A MICROMECHANICAL MODEL FOR THE NONLINEARITY OF MICROCRACKS IN RANDOM DISTRIBUTIONS AND THEIR EFFECT ON HIGHER HARMONIC RAYLEIGH WAVE GENERATION

A Thesis
Presented to
The Academic Faculty

by

Tobias Oberhardt

In Partial Fulfillment
of the Requirements for the Degree
Master of Science in Engineering Science and Mechanics in the
School of Civil and Environmental Engineering

Georgia Institute of Technology
December 2015

A MICROMECHANICAL MODEL FOR THE NONLINEARITY OF MICROCRACKS IN RANDOM DISTRIBUTIONS AND THEIR EFFECT ON HIGHER HARMONIC RAYLEIGH WAVE GENERATION

Approved by:

Prof. Laurence J. Jacobs, Advisor
School of Civil and Environmental Engineering
Georgia Institute of Technology

Dr. Jin-Yeon Kim
School of Civil and Environmental Engineering
Georgia Institute of Technology

Prof. Jianmin Qu
Department of Civil and Environmental Engineering
Northwestern University

Date Approved: 21. August 2015

ACKNOWLEDGEMENTS

First and foremost, I want to express my deepest appreciation to Prof. Dr.-Ing. Lothar Gaul of the Institute of Applied and Experimental Mechanics at the University of Stuttgart and Prof. Laurence J. Jacobs from the Georgia Institute of Technology in Atlanta, Georgia for establishing and fostering the ISAP program between the two universities.

My graduate studies at Georgia Tech extensively broadened my mind and enriched my scientific experience in the research field of mechanics in general and in particular the fields of finite element simulation and contact mechanics. Therefore, I want to acknowledge the outstanding support of Prof. Jacobs in preparation of and throughout my year in the United States. He offered an open ear throughout my time in the States and helped me wherever possible. Furthermore, he made it possible for me to attend the Quantitative Nondestructive Evaluation (QNDE) Conference 2015 in Minneapolis, Minnesota to present the results of my research work. Moreover, I am sincerely indebted to Prof. Gaul for choosing me as a candidate for the ISAP program 2014/2015.

I would especially like to thank my advisor, Dr. Jin-Yeon Kim, for sharing his extensive knowledge and expertise, and having fruitful discussions with me. Dr. Kim always guided my research in a promising direction and gave me valuable advice. Therefore, I want to thank him for his immense contribution to this thesis and his supportive understanding and positive attitude when I needed it most.

Thank you also to Christian Ehrlich of the Institute of Applied and Experimental Mechanics at the University of Stuttgart for giving helpful guidance in the bureaucratic paperwork beginning in early January 2014 until August 2014.

Furthermore, I would like to thank Sibylle Langer of the Office of International Affairs for administratively supporting the program with regard to the German Academic Exchange Service ("Deutscher Akademischer Austauschdienst (DAAD)"), whose generous scholarship was highly appreciated.

Thanks go to Prof. Jianmin Qu from Northwestern University in Chicago, Illinois for reviewing this thesis and for serving as a committee member.

Furthermore, I would like to thank my lab partners Gun Kim, David Torello, Katie Scott, Mehdi Rashidi, Alexander Lakocy, and Matthias Uhrig for their fruitful scientific discussions and for creating a pleasant working atmosphere in the laboratory. Especially, I want to acknowledge my program colleague Aulon Bajrami for sharing both joy and sorrow during our stay at Georgia Tech and for becoming a friend in the last year, contributing a lot to this unforgettable experience of studying abroad.

Furthermore, I am grateful for all my friends in Germany for keeping in touch with me throughout my year abroad and for helping me wherever possible.

Last but not least, I would like to express my deepest gratitude to my family who exceptionally supported me in the last years both mentally and financially and for encouraging me whenever it was necessary during this challenging, but rewarding year.

Mathematics is the instrument that brings about the mediation between theory and practice, between thought and observation; it builds the connecting bridge and designs it increasingly robust. So it is that all our present culture, insofar as it is based on intellectual penetration and instrumentalization of nature, finds its foundation in mathematics.

David Hilbert (1862 - 1943)

(Translated from German)

TABLE OF CONTENTS

LIST OF TABLES

LIST OF FIGURES

LIST OF SYMBOLS AND ABBREVIATIONS

SYMBOL	DESCRIPTION
β	acoustic nonlinearity parameter
β_{crk}	nonlinearity parameter for solids with cracks
Γ	Gamma function
δ	approach, relative displacement
δ_{ij}	Kronecker delta
δ_s	equilibrium distance
ϵ_{ij}	strain tensor
η	number density of asperities
λ, μ	Lamé parameters
λ_L, λ_R	wavelength of first harmonic longitudinal and Rayleigh wave
μ_{dyn}	dynamic friction coefficient
μ_{stat}	static friction coefficient
ν	Poisson's ratio
ξ	degrees of freedom of χ^2 - probability density function
ρ	density
$\boldsymbol{\sigma^{PK}}$, σ_{ij}^{PK}	first Piola-Kirchhoff stress tensor
σ	stress
σ_0	opening stress
σ_{appl}	applied stress
σ_{asp}	reactive asperity stress
σ_{comp}	RMS roughness of composite surface
σ_i	nominal normal stress in crack opening state i

SYMBOL	DESCRIPTION
σ_{ij}	Cauchy stress tensor
σ_{int}	internal stress
σ_n	total normal stress at the interface
σ_{rms}	RMS roughness
σ_{xx}, σ_{xz}	Rayleigh wave normal stress and Rayleigh wave shear stress
ϕ	χ^2 - probability density function
Φ, $\boldsymbol{\psi}$	scalar and vector potential
ω	circular frequency
Ω_c	Rayleigh critical angle
Ω_{crit}	shear wave critical angle
Ω_{Li}, Ω_{Lr}, Ω_{Lt}	angle of incident, reflected and transmitted longitudinal wave at solid-solid interface
Ω_{Si}, Ω_{Sr}, Ω_{St}	angle of incident, reflected and transmitted shear wave at solid-solid interface
a	radius of hemispheres
A_{Ci}	area in contact state i
A_{nom}	nominal contact area
A_{real}	real contact area
b_j	body forces
c_L, c_S	longitudinal and shear wave velocity
c_{LW}	longitudinal wave velocity in the wedge
c_{RS}	Rayleigh wave velocity in the specimen
C	stiffness
C_{ijkl}	fourth-order elastic stiffness tensor
C_{ijklmn}, M_{ijklmn}	higher-order elastic tensor

SYMBOL	DESCRIPTION
C_{slip}	tangential interface stiffness during "slipping"
C_{stick}	tangential interface stiffness during "sticking"
C_t	tangential interface stiffness
$\boldsymbol{d}$	direction of motion
$\boldsymbol{E}$	Lagrangian strain tensor
E	Young's modulus
E^*	plane-stress modulus
f	force to compress elastic hemispheres
F_{ij}	deformation gradient
$\overline{F}_N$	area-weighted normal force
F_{N_i}	normal force in contact state i
$F_{R_{dyn}}$	friction force
$F_{R_{stat}}$	static friction force threshold
F_{shear}	force due to Rayleigh wave shear stress
h_s	characteristic asperity height
i	imaginary unit
$\boldsymbol{I}$	identity matrix
k_L, k_S, k_R	wavenumber of longitudinal, shear and Rayleigh wave
k_{Si}, k_{Lr}, k_{Sr}	wavenumber of incident shear, reflected longitudinal and shear wave
$\boldsymbol{n}$	unit normal vector
N_{crk}	crack density
$\boldsymbol{p}$	direction of propagation
P	load
P_i	incident longitudinal wave

SYMBOL	DESCRIPTION
P_r	reflected longitudinal wave
P_t	transmitted longitudinal wave
r	radial crack coordinate
R	crack radius
S	surface
SV_r	reflected shear vertical wave
SV_t	transmitted shear vertical wave
t	time
t_j	traction
u_i	displacement
V	volume
V_{crack}	crack volume
w_i	weighting factor
W	specific strain energy per unit mass
$\boldsymbol{x^*}$, x_i^*	Eulerian coordinate
$\boldsymbol{x}$, x_i	Lagrangian coordinate
y_i	distance from a mean height level

ABBREVIATION	DENOTATION
NDE	Nondestructive evaluation
NLU	Nonlinear ultrasonic
FEM	Finite Element method
FE	Finite Element
SCC	Stress-Corrosion Cracking
SV-wave	Shear vertical wave
SH-wave	Shear horizontal wave
P-wave	Longitudinal wave
CAN	Contact Acoustic Nonlinearity
IGSCC	Intergranular Stress-Corrosion Cracking
IGC	Intergranular Corrosion
PDF	Probability density function
RMS	Root mean square

SUMMARY

This research addresses the modeling of randomly distributed surface-breaking microcracks and their effects on higher harmonic generation in Rayleigh surface waves. The modeling is based on micromechanical considerations of rough surface contact. A microcrack does not necessarily have the same opening state along the entire crack path. More precisely, it can have different opening states, ranging from fully-opened to fully-closed. In the remaining crack parts the rough crack faces are in asperity contact. The normal contact stress at the interface is in an equilibrium state due to internal stress in the solid. This contact stress is alternated by the normal stress of an incident Rayleigh wave. On the basis that every crack part can be described by a local stress-strain relationship, the whole crack is described by its effective stress-strain relationship, which is the result of a weighted average of all the local stress-strain relationships. While this type of Contact Acoustic Nonlinearity (CAN) – the nonlinear interface loading and unloading due to normal wave incidence – generates the full spectrum of higher harmonics, only odd harmonics are generated in the case of the "stick-slip" mechanism, which is the second type of CAN this research investigates. Stick-slip occurs when the static friction force threshold is overcome temporarily due to the Rayleigh wave shear stress. The different crack opening states are accounted for by an area-weighted normal force since no normal force evolves in fully-opened crack parts , whereas in fully-closed and asperity contact parts different normal forces develop.

The derived effective stress-strain relationship is implemented into a finite element model by means of a Mooney-Rivlin hyperelasticity model whose input parameters

are optimized using a least-squares optimization. Moreover, the frictional interfaces are implemented into a finite element model by using a master-slave contact surface approach and constraining the opening of the contact to prevent wave rectification. The evolution of acoustic nonlinearity in Rayleigh waves is studied for varying crack densities, opening state percentages and RMS roughnesses of crack faces. The nonlinearity parameter β is predicted and the odd harmonic generation is studied numerically.

CHAPTER I

INTRODUCTION

This chapter introduces the importance and effectiveness of nonlinear ultrasonic (NLU) methods in nondestructive evaluation (NDE) and provides some background knowledge about the concepts of Contact Acoustic Nonlinearity (CAN) and the mechanisms which can cause microcracking in structures.

1.1 Motivation

The popularity of metals in engineering applications can be explained by their advantageous material properties. Strength, stiffness, hardness, and tolerance of high temperatures prompt engineers to make use of them in a great variety of applications [13]. Nevertheless, metals when exposed to a combination of tensile stress and a corrosive environment can become susceptible to corrosion. Stress-Corrosion Cracking (SCC) causes microstructural changes in a material which can lead to microcracking. For instance, these SCC cracks pose a serious threat to the structural integrity of nuclear power plants. Unfortunately, traditional ultrasonic NDE methods are not capable of accurately detecting these cracks, especially when they are partially closed due to a temporary shut-down of the plant and the removal of tensile stress fields [33]. However, these cracks can cause tremendously high acoustic nonlinearity due to CAN mechanisms ([9], [40]). As a result, new methods are developed to detect SCC cracks by monitoring the acoustic nonlinearity. Nonlinear ultrasonic (NLU) techniques have been shown to be able to detect material degradation early ([20], [21]), [44], [45]) and they can help prevent macroscopic failure of components during service.

Note that SCC is only one type of material degradation mechanism; for instance, fatigue also causes a change in a material's microstructure and decreases material

strength. Independent of the specific mechanism, macroscopic failures often attract attention to themselves because they have significant precursors. In fact, in the previously mentioned cases, the initiation and growth of microcracks precede the complete loss of structural integrity. NLU techniques are able to quantitatively evaluate damage by analysing the generated acoustic nonlinearity by defects in an input probing ultrasonic signal. Since microcracks typically initiate on the material surface, Rayleigh surface waves whose energy is confined to the near-surface region are highly advantageous to evaluate this type of damage and find defects in the near-surface region. The knowledge of the dependency of acoustic nonlinearity on crack density and other parameters is of high interest to gain a better understanding of nonlinear wave propagation in microcracked components and wave-defect interaction.

1.2 Problem Statement

This research investigates how the acoustic nonlinearity in Rayleigh surface waves depends on parameters such as crack density and crack face roughness. In order to answer this question, a micromechanical model to describe the contact problem of rough by internal stresses compressed crack faces under a Rayleigh surface wave drive needs to be developed, implemented into a finite element model which allows for effective Rayleigh wave generation, and then studied for varying microcrack densities of randomly distributed surface-breaking microcracks. The ultimate objective of this research approach is to predict the absolute acoustic nonlinearity for microcracked components.

1.3 Literature Review

The theoretical background related to this research reaches back several decades. Probably the first study on acoustic harmonic generation from an interface and a crack was performed in 1978 by Buck et al. [9] who investigated the harmonic generation at unbonded interfaces and fatigue cracks.

In 1979, Richardson [36] studied the nonlinear dynamics of a system which is composed of an unbonded planar interface separating two semi-infinite linear elastic media. The nonlinearity originates from the opening and closing of the interface. Since the interface is unbonded, it is not able to support tension. Thus, it opens up in the tension phase of an incident wave.

Solodov et al. ([40], [34]) investigated different mechanisms of CAN, amongst others the "clapping" of crack faces, a frictional interface under a shear wave drive and subharmonic generation. Anomalously high nonlinearity is reported which is promising for NDE applications.

Back in 1966, Greenwood and Williamson [18] proposed an elastic contact model for the contact of nominally flat surfaces. The asperities are assumed to be elastic hemispherical bumps whose top heights are distributed according to a probability density function.

In 1997, Nazarov and Sutin [30] derived the nonlinearity parameter for elastic solids including randomly distributed penny-shaped cracks. The contact between rough crack faces is assumed to be elastic. The interfaces are compressed by an internal stress in the solid.

Cantrell [10] used the rough surface model of Nazarov and Sutin [30] to derive the acoustic nonlinearity from randomly distributed cracks in a solid and introduces an acoustic nonlinearity parameter for cracks β_{crk}, which relates contact properties at the interface to the generated acoustic nonlinearity.

In 2001, Kawashima et al. [23] numerically investigated second harmonic generation (SHG) due to minute surface cracks using self-defined finite elements. The crack faces are assumed to be perfectly flat and parallel. The stress-strain relationship describing the crack is assumed to be a superposition of different bimodular stress-strain relationships accounting for different states of opening.

1.4 Outline

Chapter 1 introduces the field of non-destructive evaluation (NDE) and underlines the advantages of nonlinear ultrasonic (NLU) methods. Furthermore, it provides the research questions we want to answer with this research and a literature review showing previous work in related topics.

Chapter 2 discusses aspects of linear wave propagation in a linear elastic, isotropic, and macroscopical homogeneous solid. After that, particular wave phenomena of interest are discussed in more detail. At the end of Chapter 2 a brief introduction into the theory of nonlinear wave propagation in general and nonlinear Rayleigh surface waves in particular is given.

Chapter 3 discusses two exemplary mechanisms for microcracking in structures: stress-corrosion cracking (SCC) and fatigue.

Chapter 4 presents a micromechanical model for the contact problem of rough surfaces under Rayleigh wave incidence.

Chapter 5 gives remarks on the finite element model that is developed to generate Rayleigh waves and to investigate the effect randomly distributed surface microcracks have on initially monochromatic Rayleigh waves.

Chapter 6 summarizes the numerical results concerning SHG for varying crack densities, opening state percentages and crack face roughness values. Moreover, odd harmonic generation due to frictional interfaces under Rayleigh wave incidence is shown.

Finally, Chapter 7 draws a conclusion and mentions possible future work.

CHAPTER II

FUNDAMENTALS OF WAVE PROPAGATION IN SOLIDS

This chapter presents the fundamentals of wave propagation in linear elastic, isotropic, and macroscopical homogeneous solids and is based on the mathematical derivations of Achenbach [1], Graff [17], and Viktorov [43]. After deriving the linear wave equation, we introduce common wave phenomena which play a major role in this research and discuss both nonlinear wave propagation in general and nonlinear Rayleigh surface waves in particular.

2.1 Cauchy's Equation of Motion

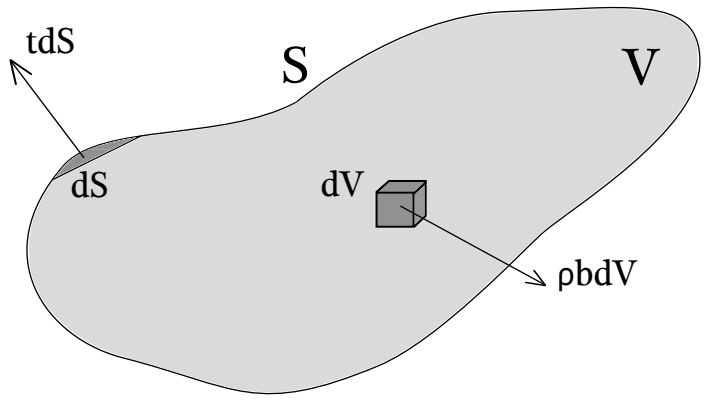

Figure 2.1: Balance of linear momentum for Cauchy's first law of motion.

The integral form of the balance of linear momentum for a domain with an arbitrary volume V, surface S, and density ρ can be written as

$$\int_V \rho \ddot{u}_i dV = \int_S t_j dS + \int_V \rho b_i dV \tag{1}$$

in which t_j is the traction vector, b_i represents the body forces and u_i the displacements [1].

We now want to write the balance of linear momentum in terms of the Cauchy stress σ_{ij}. Using Cauchy's stress formula, the traction t_j across an arbitrary plane of orientation can be obtained by multiplying the Cauchy stress with the outward pointing unit normal vector n_i of this arbitrary plane of orientation

$$t_j = \sigma_{ij} n_i \tag{2}$$

in which n_i is the unit normal vector on the surface S. In order to perform a vector integral transformation to write Equation 1 in terms of volume integrals, we make use of the divergence theorem.

2.1.1 Divergence Theorem

The divergence theorem states that the integral of the outer normal component of a vector over the closed surface S is equal to the integral of the divergence of the vector over the volume bounded by the closed surface, i.e. the outward flux of the displacement field $\boldsymbol{u}$ through the closed surface S equals its sources and sinks in the volume [1].

Theorem 1 (Divergence Theorem)*: Consider a region B of volume V, bounded by a surface S. Furthermore, consider the vector field* $\boldsymbol{v}$ *with continuously differentiable components in B. Then the divergence theorem states*

$$\int_S v_i n_i dS = \int_V \frac{\partial v_i}{\partial x_i} dV \tag{3}$$

in which n_i *are the components of the unit vector along the outer normal to the surface S.*

Making use of the divergence theorem, we can express Equation 1 in terms of the volume integral form as

$$\int_V \rho \ddot{u}_i dV = \int_V \sigma_{ij,j} dV + \int_V \rho b_i dV, \tag{4}$$

which can be written by rearranging as

$$\int_V (\sigma_{ij,j} + \rho b_i - \rho \ddot{u}_i) dV = 0. \tag{5}$$

Since Equation 5 must hold for any arbitrary closed small volume V in the body, Cauchy's first law of motion follows as

$$\sigma_{ij,j} + \rho b_i = \rho \ddot{u}_i. \tag{6}$$

2.2 Linear Stress and Strain

Stress σ_{ij} and strain ϵ_{kl} are linked to each other by a stress-strain relationship. This relationship can be written by means of the fourth-order elastic stiffness tensor C_{ijkl} leading to the generalized Hooke's law

$$\sigma_{ij} = C_{ijkl} \epsilon_{kl} \tag{7}$$

with C_{ijkl} having 81 components. However, making use of the symmetry of both stress and strain tensors

$$C_{ijkl} = C_{jikl} \quad \text{or} \quad C_{ijkl} = C_{ijlk} \tag{8}$$

and thermodynamic considerations

$$C_{ijkl} = C_{klij}, \tag{9}$$

the number of independent components reduces to 21. If, additionally, isotropy is assumed, the number of independent components reduces to two, the so-called Lamé parameters λ and μ

$$\lambda = \frac{E\nu}{(1+\nu)(1-2\nu)}, \qquad \mu = \frac{E}{2(1+\nu)} \tag{10}$$

with E being the Young's modulus and ν the Poisson's ratio.

Therefore, in the case of a linear elastic, macroscopical homogeneous, isotropic solid the stress-strain relationship from Equation 7 becomes

$$\sigma_{ij} = \lambda \epsilon_{kk} \delta_{ij} + 2\mu \epsilon_{ij} \tag{11}$$

with δ_{ij} being the Kronecker delta ($\delta_{ij} = 1$ for $i = j$, $\delta_{ij} = 0$ for $i \neq j$).

2.3 The Wave Equation for a Linear Elastic Solid

Furthermore, under the assumption of infinitesimal strains we can write the linear strain tensor ϵ_{ij} in terms of the displacement u

$$\epsilon_{ij} = \frac{1}{2}(u_{i,j} + u_{j,i}). \tag{12}$$

By neglecting the body forces and making use of the previous made derivations, we get the elastic wave equation

$$\mu u_{i,jj} + (\lambda + \mu) u_{j,ji} = \rho \ddot{u}_i \tag{13}$$

which can be rewritten using vector instead of index notation

$$\mu \boldsymbol{\nabla}^2 \boldsymbol{u} + (\lambda + \mu) \boldsymbol{\nabla} \boldsymbol{\nabla} \cdot \boldsymbol{u} = \rho \ddot{\boldsymbol{u}}. \tag{14}$$

2.3.1 Helmholtz Decomposition

One way to solve the system of coupled partial differential equations in Equation 14 is to use the Helmholtz Decomposition, i.e. we define both a scalar potential and a vector potential in order to express the displacement field $\boldsymbol{u}$ in Equation 14 by the two potentials.

Theorem 2 (Helmholtz Decomposition): *The displacement field* $\boldsymbol{u}$ *can be decomposed by defining a scalar potential* Φ *and a vector potential* $\boldsymbol{\psi}$

$$\boldsymbol{u} = \boldsymbol{\nabla} \Phi + \boldsymbol{\nabla} \times \boldsymbol{\psi} \quad \text{with} \quad \boldsymbol{\nabla} \cdot \boldsymbol{\psi} = 0. \tag{15}$$

Notice that the zero-divergence condition is needed in order to uniquely relate the three components of the displacement field $\boldsymbol{u}$ to the four components of the scalar and vector potentials Φ and $\boldsymbol{\psi}$.

Substituting Equation 15 into the system of three coupled partial differential equations in Equation 14 uncouples the system of equations into

$$\boldsymbol{\nabla}^2\Phi = \frac{1}{c_L^2}\ddot{\Phi} \quad \text{and} \quad \boldsymbol{\nabla}^2\boldsymbol{\psi} = \frac{1}{c_S^2}\ddot{\boldsymbol{\psi}}, \tag{16}$$

which depend only on the scalar potential and vector potential respectively, with c_L and c_S being the longitudinal and shear wave velocity. Based on Equation 10, the longitudinal and shear wave velocity can also be written in terms of the Lamé parameters λ and μ

$$c_L = \sqrt{\frac{\lambda + 2\mu}{\rho}} \quad \text{and} \quad c_S = \sqrt{\frac{\mu}{\rho}}. \tag{17}$$

2.4 Wave Phenomena

2.4.1 Plane Waves in Unbound Media

In the following derivations, the plane wave assumption, i.e. the assumption of a wave with constant stress, strain and displacement in a plane perpendicular to its direction of propagation $\boldsymbol{p}$, is made. Considering such a plane wave propagating in an unbound medium with the wave velocity c and the direction of particle motion, expressed by the unit vector $\boldsymbol{d}$, we can write the displacement in terms of the unit propagation vector $\boldsymbol{p}$ and the position vector $\boldsymbol{x}$ in the plane wave equation

$$\boldsymbol{u} = f(\boldsymbol{x} \cdot \boldsymbol{p} - ct)\boldsymbol{d}. \tag{18}$$

It is clear that this expression describes a plane of constant phase normal to the propagation vector p ($x \cdot p - ct = const.$ required).

Substituting our new expression for the displacement into Equation 14 leads to

$$(\mu - \rho \cdot c^2)\boldsymbol{d} + (\lambda + \mu)(\boldsymbol{p} \cdot \boldsymbol{d})\boldsymbol{p} = 0. \tag{19}$$

Equation 19 is satisfied by requiring the propagation vector $\boldsymbol{p}$ to be parallel to the direction of motion $\boldsymbol{d}$,

$$\boldsymbol{d} = \pm\boldsymbol{p} \quad \text{and accordingly} \quad \boldsymbol{p} \cdot \boldsymbol{d} = \pm 1. \tag{20}$$

This corresponds to a particle motion parallel to the propagation direction and is the main characteristic of a longitudinal wave traveling at a speed of c_L

$$c_L = \sqrt{\frac{\lambda + 2\mu}{\rho}}. \tag{21}$$

Figure 2.2 shows a schematic of a propagating longitudinal wave.

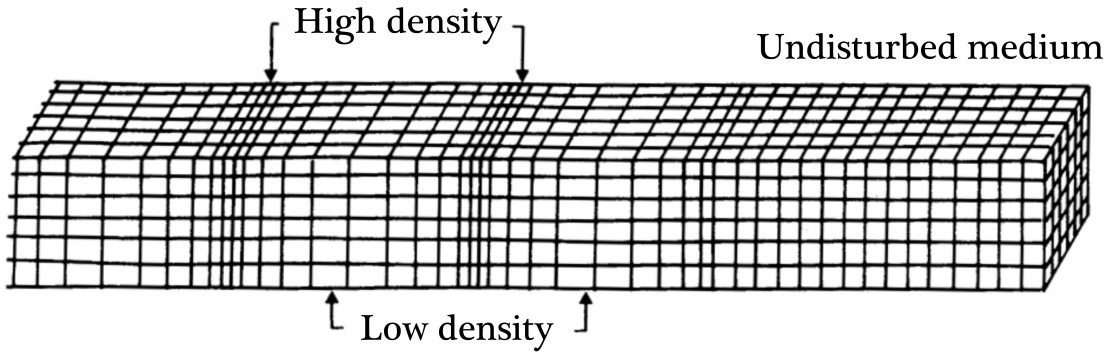

Figure 2.2: Schematic of longitudinal wave propagation [4].

However, Equation 19 is also satisfied by requiring the propagation vector $\boldsymbol{p}$ to be perpendicular to the direction of motion

$$\boldsymbol{p} \cdot \boldsymbol{d} = 0. \tag{22}$$

This describes the propagation of a shear wave traveling at a phase velocity of

$$c_S = \sqrt{\frac{\mu}{\rho}}. \tag{23}$$

Figure 2.3 shows a schematic of a propagating shear wave.

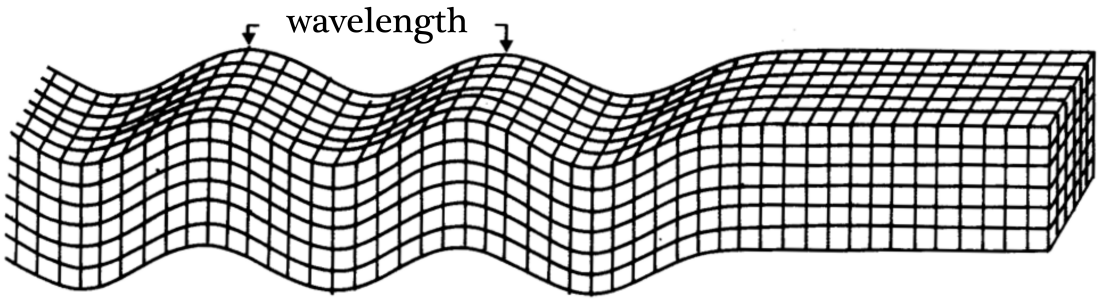

Figure 2.3: Schematic of shear wave propagation [4].

2.4.2 Mode Conversion, Reflection and Transmission at a Solid-Solid Interface

The previous relationships are derived under the assumption of an infinite medium. However, in reality waves often encounter boundaries while propagating. As shown in Figure 2.4, a longitudinal wave P_i under oblique incidence hits a solid-solid interface which causes both a reflected longitudinal P_r, a transmitted longitudinal P_t, and due to the phenomenon of mode conversion, a reflected and transmitted shear vertical wave (SV-wave) SV_r and SV_t. Analogously this occurs under SV-wave incidence. However, under the incidence of horizontally polarized shear waves (SH-waves) no mode conversion occurs, regardless of the angle of incidence. Note that also under normal incidence no mode conversion occurs, no matter if longitudinal, vertically or horizontally polarized shear waves are incident.

According to Snell's Law, Equation 24 describes the transmission and reflection of waves at a solid-solid interface for longitudinal and shear wave incidence respectively. While the first index of the wave velocities stands for the type of wave, i.e. either longitudinal (L) or shear (S) wave, the second index refers to either "incident" (i), "reflected" (r), "transmitted" (t), solid '1' or solid '2'.

$$\frac{\sin\Omega_{Li}}{c_{L1}} = \frac{\sin\Omega_{Lr}}{c_{L1}} = \frac{\sin\Omega_{Lt}}{c_{L2}} = \frac{\sin\Omega_{Sr}}{c_{S1}} = \frac{\sin\Omega_{St}}{c_{S2}} \tag{24}$$

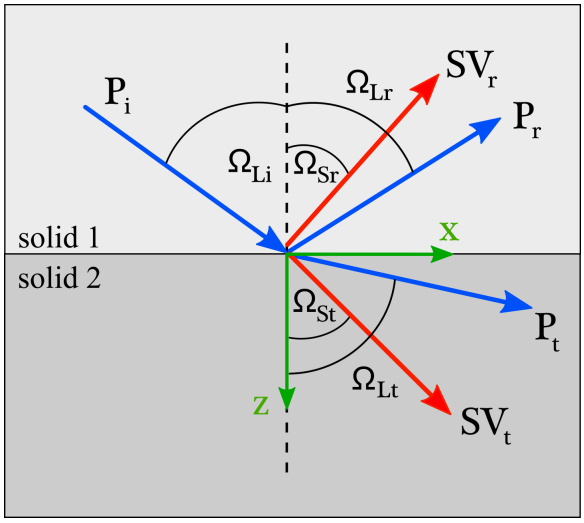

Figure 2.4: Reflected and transmitted waves at a solid-solid interface.

2.4.3 Reflection of Plane Waves at a Stress-Free Boundary

We observe another wave phenomenon when waves are incident on a stress-free boundary. Figure 2.5 shows a schematic of an incident SV-wave at a stress-free boundary, which can be idealized as a solid-vacuum interface.

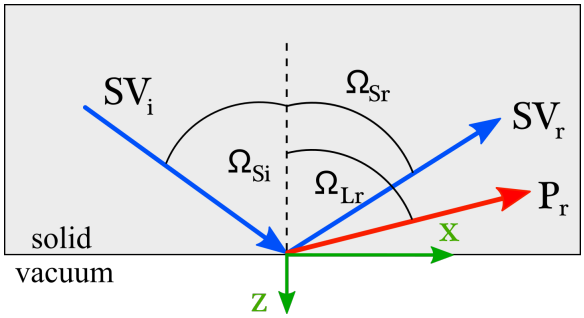

Figure 2.5: SV-wave incident on a stress-free boundary.

Note that no transmitted but only reflected waves exist in the case of a solid-vacuum interface. The reflected SV-wave propagates under an angle $\Omega_{Sr} = \Omega_{Si}$, the reflected P-wave under an angle

$$\sin(\Omega_{Lr}) = \frac{c_L}{c_S}\sin(\Omega_{Si}). \tag{25}$$

According to Snell's law, the following relationships between the angles of incident and reflected waves have to be satisfied

$$k_{Si}\sin(\Omega_{Si}) = k_{Lr}\sin(\Omega_{Lr}) = k_{Sr}\sin(\Omega_{Sr}). \tag{26}$$

in which k_L and k_S are the wavenumbers of longitudinal and shear wave respectively. In two cases no mode conversion occurs: $\Omega_{Si} = 0$, which means normal incidence at the interface, and $\Omega_{Si} > \Omega_{crit}$ with $\Omega_{crit} = \arcsin\left(\frac{c_S}{c_L}\right)$ being the shear wave critical angle. In the latter case, only the SV-wave is reflected whereas the reflected P-wave becomes evanescent and generates a longitudinal surface wave. Comparable effects can be seen for transmitted waves across a solid-solid interface for an appropriate combination of materials. This phenomenon of waves traveling closely confined to a stress-free surface leads directly to the subject of Rayleigh waves which are discussed in more detail in the following section.

2.5 Rayleigh Surface Waves

This section presents some important properties of Rayleigh surface waves. The derivations in this section leading to the displacement fields of Rayleigh waves are based on Herrmann et al. [21], Viktorov [43], and Rose [38] and play an important role in understanding the micromechanical model for the nonlinearity of microcracks in Chapter 4.

Let us consider a two-dimensional Rayleigh wave propagating in the positive x direction while the z axis points into the depth of the half-space. Then we can express the displacement field of this Rayleigh wave by

$$\begin{aligned} u_x &= Be^{-bz}e^{ik_R(x-c_Rt)} \\ u_z &= De^{-bz}e^{ik_R(x-c_Rt)}, \end{aligned} \tag{27}$$

with c_R being the phase velocity of the Rayleigh wave with wavenumber k_R. Since this displacement field has to satisfy the equation of motion, we get the solution of

the system of equations for the non-trivial parameters B and D

$$\left(c_L^2 b^2 - (c_L^2 - c_R^2)k_R^2\right)\left(c_S^2 b^2 - (c_S^2 - c_R^2)k_R^2\right) = 0. \tag{28}$$

By setting each term in Equation 28 to zero we get four solutions for b. However, only the following two are physically acceptable since b has to be positive for decaying displacement amplitudes with increasing depth,

$$\begin{aligned} b_1 &= k_R\left(1 - \frac{c_R^2}{c_L^2}\right)^{\frac{1}{2}}, \\ b_2 &= k_R\left(1 - \frac{c_R^2}{c_S^2}\right)^{\frac{1}{2}}. \end{aligned} \tag{29}$$

Using Equation 29 we can obtain the following two ratios for the parameters B and D

$$\begin{aligned} \left(\frac{D}{B}\right)_1 &= -\frac{b_1}{ik_R}, \\ \left(\frac{D}{B}\right)_2 &= \frac{ik_R}{b_2}. \end{aligned} \tag{30}$$

In a next step, we substitute Equation 29 and 30 into Equation 27 and get

$$\begin{aligned} u_x &= \left(B_1 e^{-b_1 z} + B_2 e^{-b_2 z}\right) e^{ik_R(x - c_R t)}, \\ u_z &= \left(-\frac{b_1}{ik_R} B_1 e^{-b_1 z} + \frac{ik_R}{b_2} B_2 e^{-b_2 z}\right) e^{ik_R(x - c_R t)}. \end{aligned} \tag{31}$$

In order to determine the relationship between the parameters B and D, we use the stress boundary conditions at the stress-free surface. Therefore, we require $\sigma_{zz} = 0$ and $\sigma_{xz} = 0$ at $z = 0$.

Then, the relationship between the parameters B_1 and B_2 is found to be

$$B_2 = -\frac{2b_1 b_2}{k_R^2 + b_2^2} B_1. \tag{32}$$

This leads us to the following displacement formulation

$$\begin{aligned} u_x &= B_1\left(e^{-b_1 z} - B_2 \frac{2b_1 b_2}{k_R^2 + b_2^2} e^{-b_2 z}\right) e^{ik_R(x - c_R t)}, \\ u_z &= iB_1 \frac{b_1}{k_R}\left(e^{-b_1 z} - \frac{2k_R^2}{k_R^2 + b_2^2} e^{-b_2 z}\right) e^{ik_R(x - c_R t)}. \end{aligned} \tag{33}$$

The phase shift between the displacements u_x and u_z is 90°. The equation for the Rayleigh wave phase velocity follows to

$$\left(2 - \frac{c_R^2}{c_S^2}\right)^2 - 4\left(1 - \frac{c_R^2}{c_L^2}\right)^{\frac{1}{2}}\left(1 - \frac{c_R^2}{c_S^2}\right)^{\frac{1}{2}} = 0. \tag{34}$$

An approximate solution to Equation 34 is

$$c_R = \frac{0.862 + 1.14\nu}{1 + \nu} c_S. \tag{35}$$

Note that the Rayleigh wave phase velocity is independent of the Rayleigh wavelength λ_R. Here the weakly-dispersive character of Rayleigh surface waves becomes clear. The particles at the surface perform an ellipsoidal motion which is counterclockwise until a specific depth in the material (according to [38] approx. 0.2 λ_R). In greater depth, the sign of the horizontal displacement component changes and the particle rotation becomes clockwise.

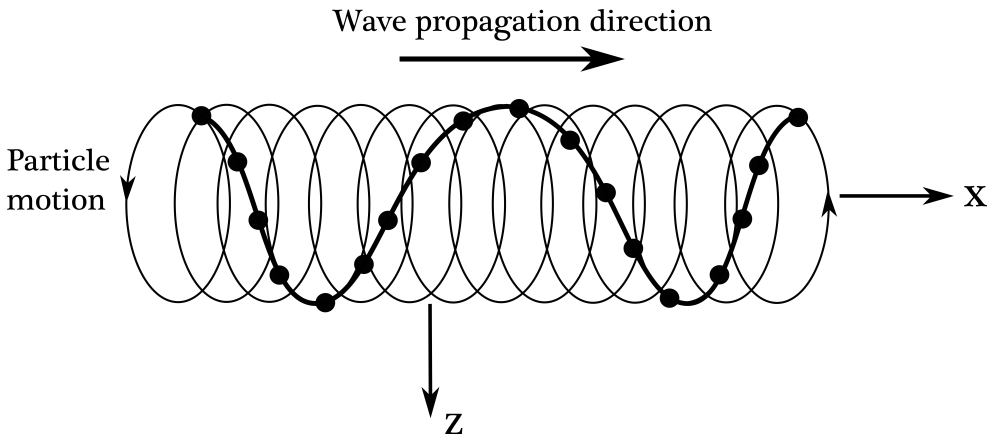

Figure 2.6: Schematic of Rayleigh wave propagation with ellipsoidal particle motion.

2.5.1 Generation of Rayleigh Surface Waves

In the literature, different techniques of experimental Rayleigh wave generation can be found, e.g. the comb and the wedge technique [43]. Despite being originally an experimental technique, this research utilizes the wedge technique to numerically excite Rayleigh waves in the finite-element model proposed in Chapter 5.

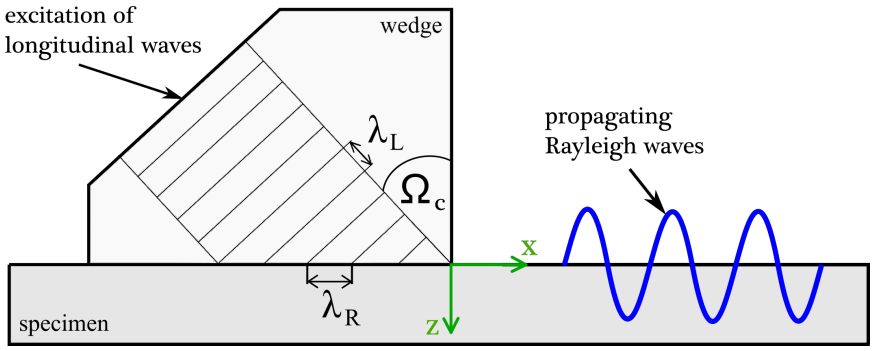

Figure 2.7: Wedge-specimen assembly for Rayleigh surface wave generation.

A requirement to excite Rayleigh surface waves is the appropriate choice of material combination and the angle of incidence. According to Snell's law, the Rayleigh critical angle can be determined by

$$\frac{\sin\Omega_c}{c_{LW}} = \frac{\sin\Omega_{RS}}{c_{RS}} \tag{36}$$

for a longitudinal wave velocity in the wedge c_{LW} being smaller than the Rayleigh wave speed c_{RS} in the specimen. In order to excite Rayleigh waves, Ω_{RS} must be $90\,^\circ$ and the longitudinal waves must hit the specimen under the Rayleigh critical angle Ω_c

$$\Omega_c = \arcsin\frac{c_{LW}}{c_{RS}}. \tag{37}$$

2.6 Nonlinear Wave Propagation

As already mentioned in the introduction to this thesis, nonlinear ultrasonic methods are more sensitive to microstructural changes in the material than linear methods. Thus, using only linear wave theory cannot be valuable to describe nonlinear wave phenomena such as higher harmonic generation. This section gives a brief introduction into nonlinear wave propagation.

To clarify the effect nonlinear media have on ultrasonic waves, we compare the two schematics in Figure 2.8. The left schematic describes the input-output relationship in a linear medium. The right schematic shows this relationship for a nonlinear medium. When using a monochromatic sinusoidal input to a linear medium, the

output signal might have another amplitude but it will still be monochromatic at the same frequency as in the input. In contrast, a monochromatic sinusoidal input to a nonlinear medium gets distorted due to the nonlinear stress-strain relationship of the medium by which higher harmonics are generated in the output signal.

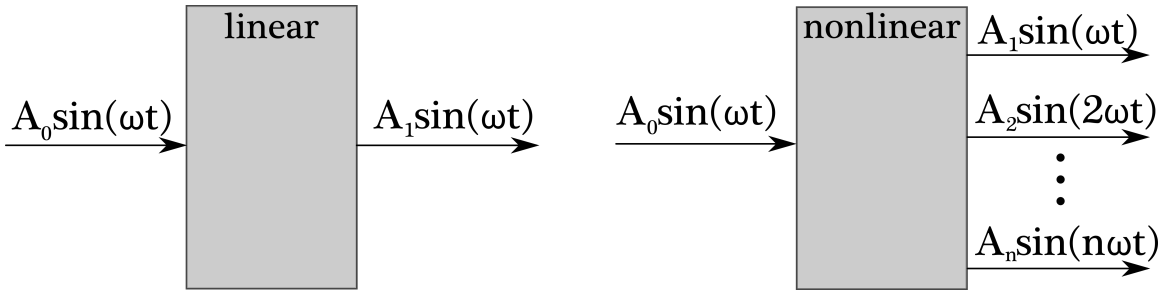

Figure 2.8: Comparison of linear and nonlinear media concerning input-output relations.

The following derivation of the nonlinear wave equation is based on the work of Hamilton and Blackstock [19].

The specific strain energy W per unit mass can be written as an expansion for small strains as follows

$$\rho_0 W = \frac{1}{2} C_{ijkl} E_{ij} E_{kl} + \frac{1}{6} C_{ijklmn} E_{ij} E_{kl} E_{mn} + ... \tag{38}$$

with C_{ijkl} and C_{ijklmn} being the second and third order elastic constants respectively, and

$$\begin{aligned} \boldsymbol{E} &= \frac{1}{2} \left(\boldsymbol{F}^T \cdot \boldsymbol{F} - \boldsymbol{I} \right), \\ E_{ij} &= \frac{1}{2} \left(\frac{\partial u_i}{\partial x_j} + \frac{\partial u_j}{\partial x_i} + \frac{\partial u_k}{\partial x_i} \frac{\partial u_k}{\partial x_j} \right) \end{aligned} \tag{39}$$

being the Lagrangian strain tensor in vectorial and indicial notation respectively. In the equation above we used the definition of the deformation gradient tensor

$$F_{ij} = \frac{\partial x_i^*}{\partial x_j} \tag{40}$$

which transforms the coordinates of a point in the reference configuration C_{ref} into the deformed configuration C_{def}.

Having defined the deformation gradient in Equation 40, we introduce the first Piola-Kirchhoff stress tensor as

$$\boldsymbol{\sigma}^{PK} = \frac{\rho_0}{\rho}\boldsymbol{\sigma} \cdot \boldsymbol{F}^{-T} \tag{41}$$

which becomes

$$\sigma_{ij}^{PK} = C_{ijkl}\frac{\partial u_k}{\partial x_l} + \frac{1}{2}M_{ijklmn}\frac{\partial u_k}{\partial x_l}\frac{\partial u_m}{\partial x_n} + ... \tag{42}$$

with M_{ijklmn} being a higher-order tensor which can be rewritten as

$$M_{ijklmn} = C_{ijklmn} + C_{ijln}\delta_{km} + C_{jnkl}\delta_{im} + C_{jlmn}\delta_{ik}. \tag{43}$$

We express the equation of motion

$$\rho\frac{\partial^2 u_i}{\partial t^2} = \sigma_{ij,j} \tag{44}$$

in Lagrangian coordinates

$$\rho_0\frac{\partial^2 u_i}{\partial t^2} = \frac{\partial \sigma_{ij}^{PK}}{\partial x_j}. \tag{45}$$

With Equation 42 this leads to the nonlinear wave equation

$$\rho_0\frac{\partial^2 u_i}{\partial t^2} = \frac{\partial^2 u_k}{\partial x_j \partial x_l}\left(C_{ijkl} + \frac{1}{2}M_{ijklmn}\frac{\partial u_m}{\partial x_n} + ...\right). \tag{46}$$

For the case of a one-dimensional longitudinal wave, Equation 46 simplifies to

$$\frac{\partial^2 u_1}{\partial t^2} = c_L^2\frac{\partial^2 u_1}{\partial x_1^2}\left(1 - \beta\frac{\partial u_1}{\partial x}\right) \tag{47}$$

in which β is the acoustic nonlinearity parameter

$$\beta = -\left(\frac{3}{2} + \frac{C_{111}}{2\rho_0 c_L^2}\right). \tag{48}$$

C_{111} is the third-order elastic constant in Voigt notation.

A detailed derivation of the nonlinearity parameter β due to weak material nonlinearity, e.g. inherent lattice anharmonicity, precipitates or vacancies, can be found in Hamilton and Blackstock [19].

Furthermore, the desription of β in terms of displacement amplitudes A_1 and A_2 of the first and second harmonic wave are derived for the case of a harmonic wave of amplitude A and frequency ω for the following excitation signal

$$u(x,t) = Asin(k_L x - \omega t). \tag{49}$$

For this excitation the nonlinear wave equation can be solved to

$$\begin{aligned} u(x,t) &= A_1 sin(k_L x - \omega t) + A_2 sin(2k_L x - 2\omega t) + \mathscr{O} \\ &= A_1 sin(k_L x - \omega t) + \frac{1}{8}\beta k_L^2 A_1^2 x sin(2k_L x - 2\omega t), \end{aligned} \tag{50}$$

in which $\mathscr{O}$ denotes the sum of higher order contributions to the displacement.

The acoustic nonlinearity parameter β becomes

$$\beta = \frac{8c_L^2 A_2}{\omega^2 A_1^2 x}. \tag{51}$$

As it can be clearly seen in Equation 51, the acoustic nonlinearity parameter is proportional to the normalized second harmonic amplitude over the propagation distance, x.

$$\beta \sim \frac{A_2}{A_1^2 x} \tag{52}$$

2.7 Nonlinear Rayleigh Surface Waves

Herrmann et al. [21] showed that the displacement field of the second harmonic Rayleigh wave becomes in the case of a material with weak quadratic nonlinearity

$$\begin{aligned} u_x(2\omega) &= A_2 \left(e^{-2b_1 z} - \frac{2b_1 b_2}{k_R^2 + b_2^2} e^{-b_2 z} \right) e^{i2k_R(x - c_R t)} \\ u_z(2\omega) &= iA_2 \frac{b_1}{k_R} \left(e^{-2b_1 z} - \frac{2k_R^2}{k_R^2 + b_2^2} e^{-b_2 z} \right) e^{i2k_R(x - c_R t)}. \end{aligned} \tag{53}$$

Due to vanishing of the third order elastic constants for shear deformation in an isotropic material, the generation of second harmonic components is solely due to longitudinal deformation. We now combine Equation 51, Equation 53 (2), the vertical

displacement at the surface $u_z(z=0) = \overline{u}_z$, and the derived displacement field in the previous section

$$\begin{aligned} u_x(\omega) &= A_1 \left(e^{-b_1 z} - B_2 \frac{2b_1 b_2}{k_R^2 + b_2^2} e^{-b_2 z} \right) e^{ik_R(x - c_R t)} \\ u_z(\omega) &= iA_1 \frac{b_1}{k_R} \left(e^{-b_1 z} - \frac{2k_R^2}{k_R^2 + b_2^2} e^{-b_2 z} \right) e^{ik_R(x - c_R t)}. \end{aligned} \tag{54}$$

The acoustic nonlinearity parameter β can be expressed by the out-of-plane displacement components of the propagating Rayleigh wave as shown in Equation 55

$$\beta = \frac{\overline{u}_z(2\omega)}{\overline{u}_z^2(\omega)} \frac{i8b_1}{k_L^2 x k_R} \left(1 - \frac{2k_R^2}{k_R^2 + b_2^2} \right). \tag{55}$$

CHAPTER III

CAUSES OF MICROCRACKING

3.1 Stress-Corrosion Cracking (SCC)

The nuclear power industry expresses interest in extending licenses for nuclear power plants to last for approximately 80 years. This calls for structures and components to act reliably under the environmental conditions, i.e. stress, temperature, corrosive environment, present in the nuclear reactor applications during this extended lifetime. Despite improvements in the control of environmental conditions which have reduced the SCC failures, SCC still remains a major safety concern in primary loop piping components. Therefore, reliable quantitative characterization of SCC damage is needed. Nonlinear methods show great potential to monitor a material's damage state. The following sections will briefly introduce one of the major driving forces of SCC in austenitic stainless steels ("Sensitization") and intergranular microcracking in these materials.

3.1.1 Driving force of SCC: Sensitization

The material property "stainless" in the context of corrosion seems to be misleading. In austenitic stainless steel, chromium is added in order to increase corrosion resistance. Nevertheless, corrosion-resistent alloys show susceptability to SCC, after their grain boundaries become depleted of corrosion inhibiting elements such as chromium. This depletion near grain boundaries is called "sensitization." Sensitization occurs when austenitic steels are held at temperatures between 400 °C and 800 °C. In this temperature range, carbon diffuses to the grain boundaries [27]. As can be seen in Figure 3.1 (left), the carbon (denoted by black circles) reacts with chromium (denoted by blue circles) to form chromium carbides (denoted by yellow ellipses) which

precipitate at the grain boundaries. This sensitization is responsible for a decrease in the elementary chromium content, which makes the steel susceptible to corrosion in chromium depleted zones near the grain boundaries (denoted by the black shaded area).

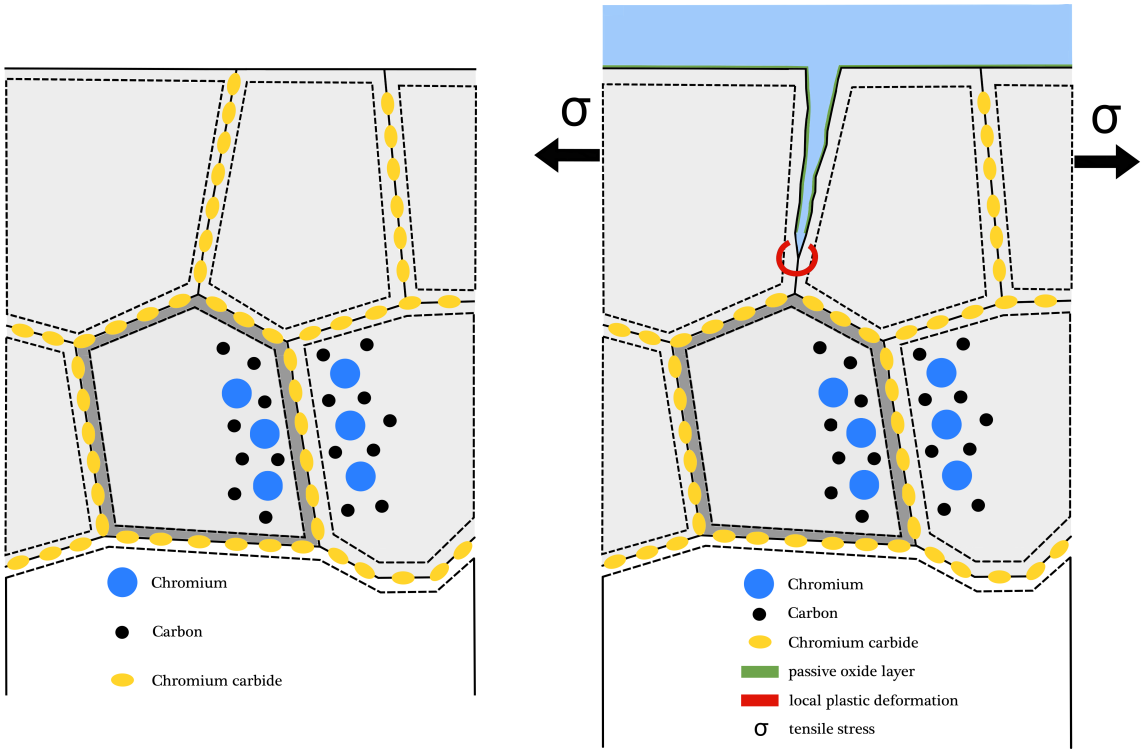

Figure 3.1: Chromium carbide precipitation at grain boundaries because of sensitization (left) and film rupture under tensile stress because of local plastic deformation (right).

Of course heating temperature is not the only factor influencing the chromium depletion in the near grain boundary regions. Heating time and exposure to environment also influence the sensitization process [27]. After falling below a minimum threshold value of chromium content, the austenitic steel becomes susceptible to intergranular stress-corrosion cracking (IGSCC). As will be described in the following section, intergranular corrosion (IGC) takes place at these boundaries of crystallites of austenitic stainless steel because of their higher susceptibility to corrosion than the grain insides.

Figure 3.2 and 3.3 show micrographs of unsensitized and heavily sensitized 304 stainless steel. As can be clearly seen, chromium carbide precipitates at the grain boundaries in the sensitized microstructure.

3.1.2 Anodic Stress-Corrosion Cracking

Anodic SCC is dominated by the process of anodic metal dissolution in which atoms serve as a electron donator. These atoms then become positively charged ions which can react with the surrounding medium, forming a passive oxide layer on the surface of the material. In forming this oxide film, the material is prevented from further oxidation.

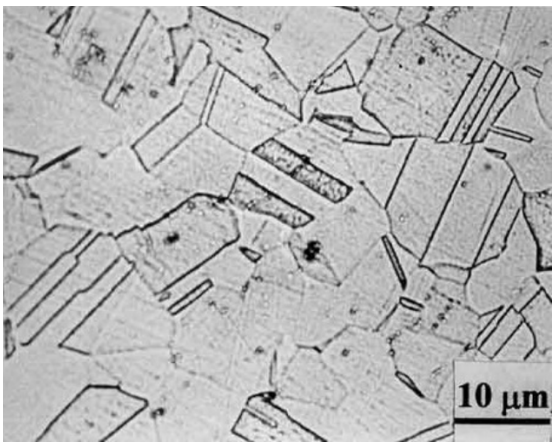

Figure 3.2: Unsensitized microstructure of 304 stainless steel [46].

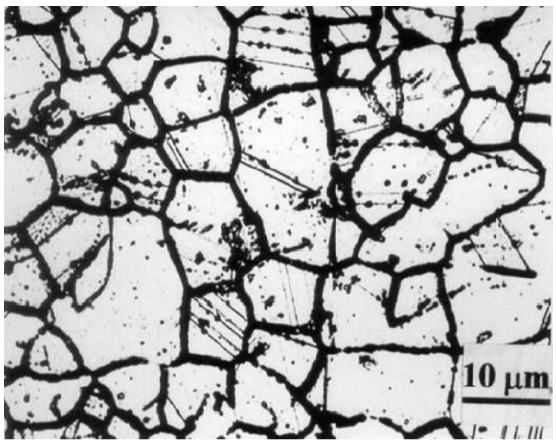

Figure 3.3: Heavily sensitized microstructure of 304 stainless steel [46].

Figure 3.1 (right) shows a schematic of the process of anodic SCC. Under application of a tensile stress, the oxide film ruptures at points of localized plastic strain (denoted by the red semi-circle), especially at the crack tip. As a result, the anodic partial reaction takes place in the freshly cracked areas. The cathodic partial reaction occurs in the areas of passivation.

Anodic SCC can artificially be accelerated by using a SCC cell in which the sample is exposed to a corrosive medium and tensile stress for a longer time [48], [27].

3.1.3 Intergranular Microcracking

As the corrosion process proceeds, the microcrack propagates along grain boundaries, especially the chromium-depleted zones (denoted by the red dotted line in Figure 3.4). The microcracks start to evolve from scratches or imperfections in the material surface. As observed by Zeitvogel et al. [48] the microcracks close due to internal stresses in the solid after removing the tensile stress.

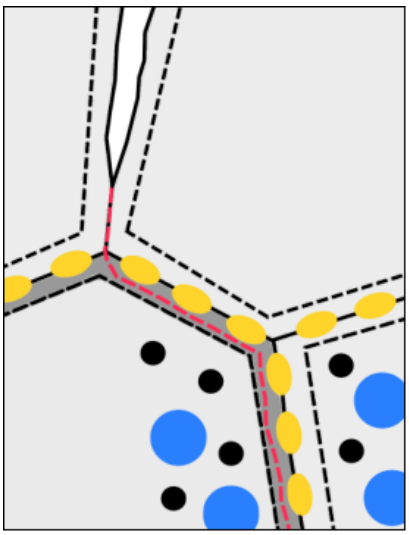

Figure 3.4: Schematic of a microcrack propagating along chromium-depleted near-grain boundary zones.

It is the fundamental research aim of this thesis to model the dynamic behavior of these microcracks and to study the effect random microcrack distributions have on Rayleigh waves. In later stages of SCC damage, these microcracks coalesce and form macroscopic cracks which cause low dispersion but high attenuation in ultrasonic waves. Thus, macrocracks can be measured via linear ultrasonic methods and are therefore beyond the scope of this research.

Figure 3.5 shows a cut through a specimen to evaluate the microcrack depth. Figure 3.6 shows a scanning electron microscope image of intergranular cracks [35]. Figure 3.7 shows a micrograph of the polished material surface of 1018 cold rolled steel [48]. Before taking the micrograph, the passive oxide layer is removed by polishing.

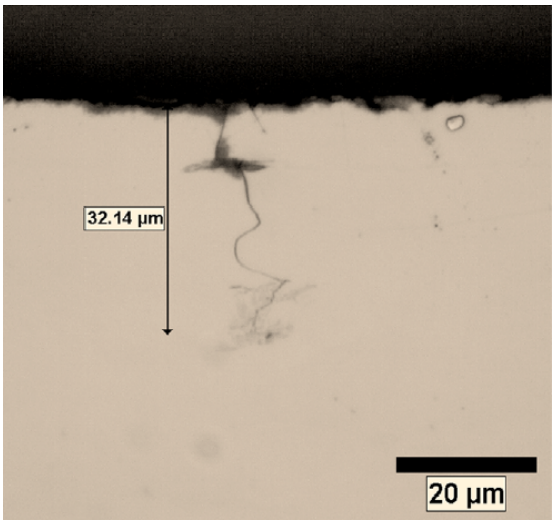

Figure 3.5: Cut through a specimen to evaluate the microcrack depth [48].

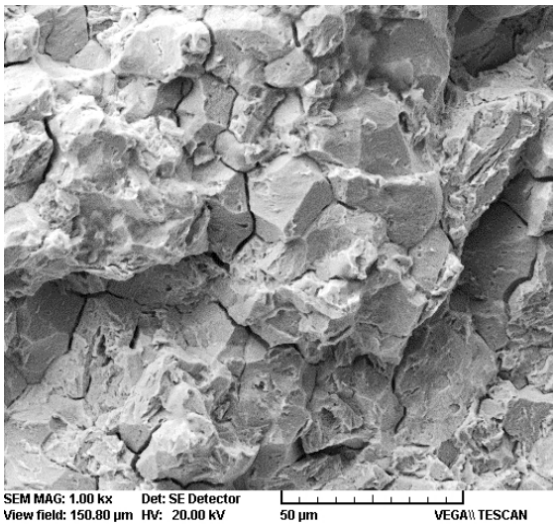

Figure 3.6: Scanning electron microscope image of an intergranular fracture characteristic of SCC [35].

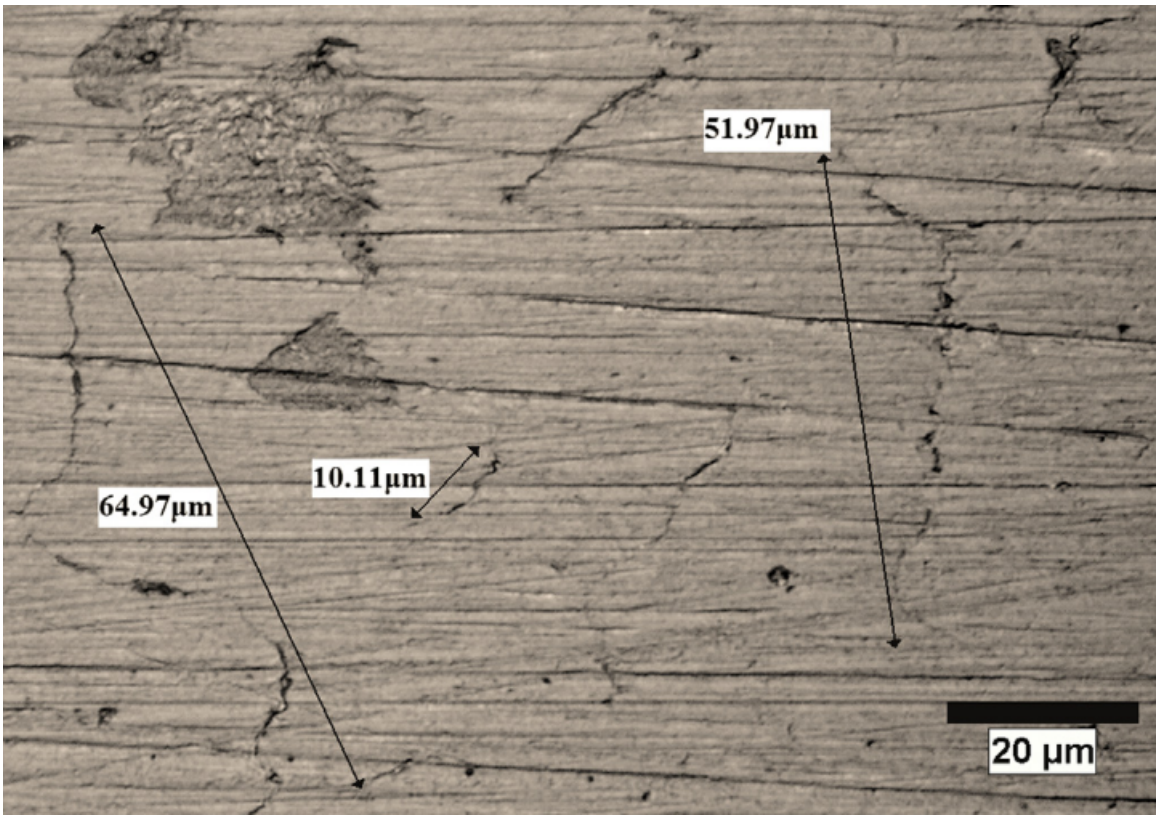

Figure 3.7: Micrograph of polished 1018 cold rolled steel specimen surface showing distributed surface-breaking SCC microcracks [49].

3.2 Fatigue Damage

Besides SCC, another primary reason for failure of structural components is fatigue. ASTM, the American Society for Testing and Materials, defines fatigue as:

"...the process of progressive localized permanent structural change occurring in a material subjected to conditions that produce fluctuating stresses and strains at some point or points and that may culminate in cracks or complete fracture after a sufficient number of fluctuations [2]."

The life of a fatigue crack consists of two parts, the initiation and the crack propagation [31]. During the initiation of a fatigue crack, dislocations play a major role. They pile up and form persistent slip bands. Due to cyclic loading, the material slides along these slip bands resulting in parts of the material which rise above the material surface ("extrusions") or fall below the surface ("intrusions"). The stresses at the surface (for example, due to bending and torsional loading) are higher than in the bulk of the material and the environmental conditions at the surface promote fatigue damage. Therefore, fatigue cracks usually initiate at the material surface.

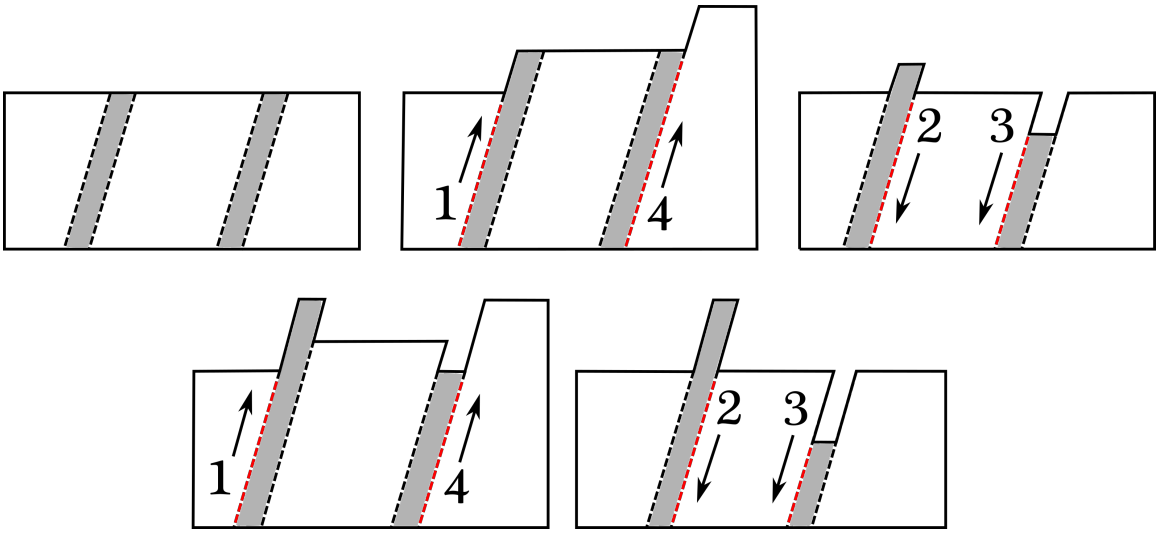

Figure 3.8: Mechanism causing extrusions and intrusions at the material surface [37].

3.2.1 Extrusions and Intrusions

As can be seen in Figure 3.8, in the first tensile phase slip bands 1 and 4 are active. After that, during compressional phase, slip bands 2 and 3 are active. This results in both an extrusion and an intrusion. Figure 3.9 (left) shows an extrusion on a metal surface. On the right side of Figure 3.9, a schematic illustrates the slip bands causing extrusions and intrusions. Intrusions most likely serve as initiation points of microcracking.

Crack initiation takes place in the presence of plastic flow which may be caused by local stress concentrations at surface scratches. Usually cracks form where persistent slip bands reach the surface of the specimen. The plastic flow in a material is to a great extent confined to localized slip bands. Therefore, crack initiation often happens where these bands of slip build extrusions and intrusions at the surface which serve as nucleation sites for cracks.

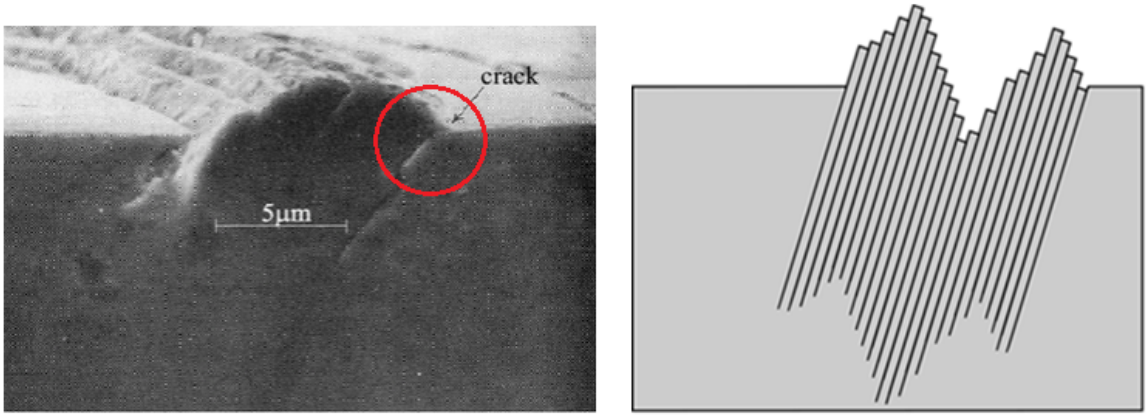

Figure 3.9: Real extrusion and intrusion (left) and schematic of slip-bands (right) [31].

Figure 3.10 shows four different stages of fatigue damage. The upper left picture shows a polished metal surface at zero stress cycles. The picture on the upper right side shows the same metal surface after n = 2000 stress cycles. Obviously, extrusions and intrusions form and can be clearly seen on the micrograph.

The lower left picture illustrates the fatigue damage due to n = 4000 stress cycles. The extrusions and intrusions become more and more clear and the fatigue damage more severe. The lower right picture shows the result of n = 6000 stress cycles, where a fatigue microcrack has formed at the material surface.

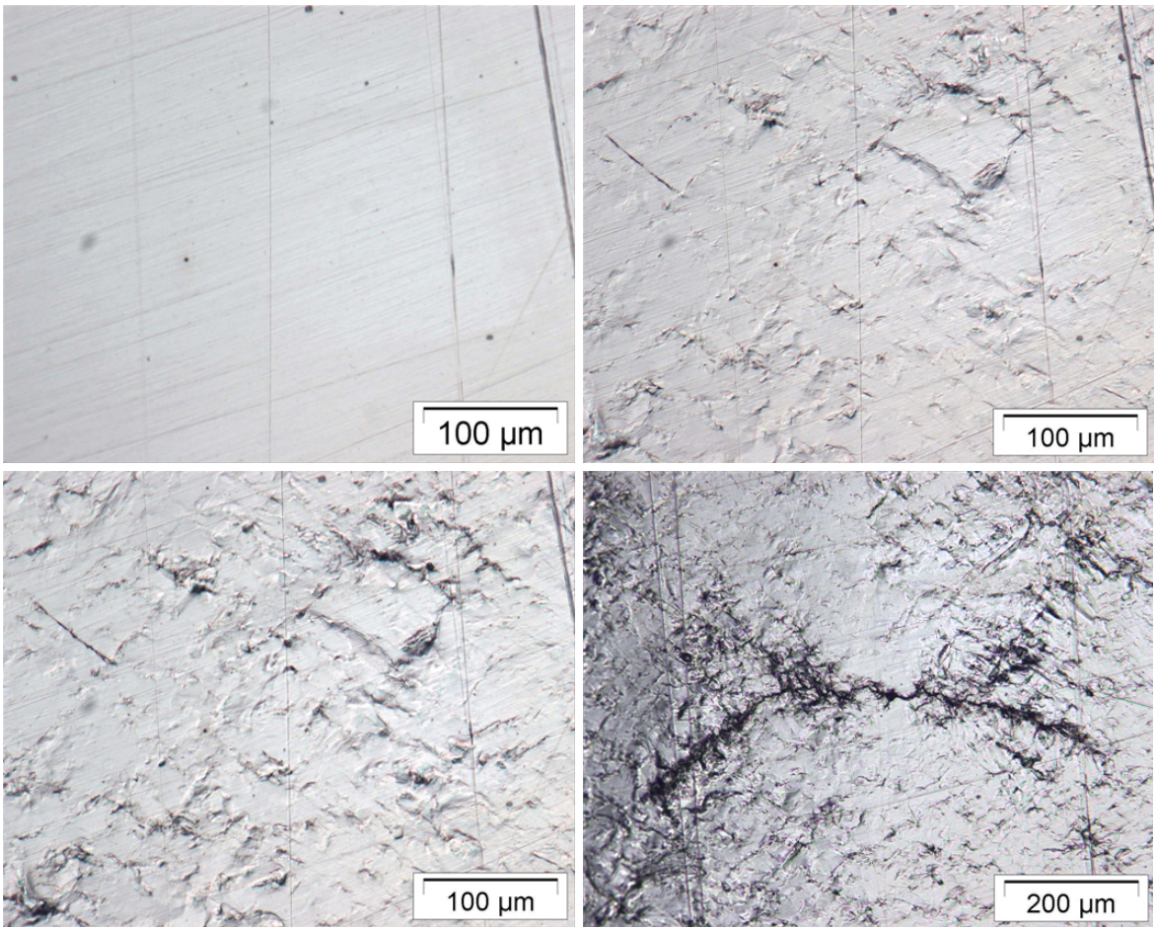

Figure 3.10: Schematic showing stages of fatigue damage on a steel specimen surface for 0, 2000, 4000, and 6000 cyclic loadings [37].

The following chapter presents a micromechanical model for microcracks which is not limited to one mechanism causing microcracking but flexible for different mechanisms.

CHAPTER IV

MICROMECHANICAL MODEL FOR THE NONLINEARITY OF MICROCRACKS

This chapter introduces a new modeling concept for microcracks and their effect on ultrasonic Rayleigh waves. Figure 4.1 shows a schematic of a microcrack which is initially closed, and a Rayleigh wave propagating through the microcrack. During the phase of compressional stress ($\sigma_{xx} < 0$) of the incident ultrasonic wave (–) (Figure 4.1 (a)) the microcrack is compressed further and this compressional as well as shear stress are transmitted across the crack faces. At a transition point from compressional (–) to tensile (+) stress, the stress at the interface can be reduced to zero and the interface is about to open (Figure 4.1 (b)). During the following phase of tensile stress (+) ($\sigma_{xx} > 0$), the microcrack is opened which results in zero stress transmission across the crack faces (Figure 4.1 (c)). Thus, a rectification of the original sinusoidal waveform occurs, i.e. the crack faces only transmit the compressional and not the tensile stress of the ultrasonic wave. Despite having drawn a simplified picture of a microcrack, this schematic makes clear that an ultrasonic wave gets distorted due to the nonlinear effect of the microcrack itself. This distortion expresses itself in acoustic nonlinearity, i.e. the generation of higher harmonics in an initially monochromatic ultrasonic wave. As can be seen in the micrograph of a real intergranular SCC microcrack in Figure 4.1 (right), both the dynamic behavior of the crack under wave incidence and its associated modeling problem become more complex. Some parts of the real microcrack can be partially closed, while others are either fully-closed or fully-opened. Furthermore, the crack faces are not perfectly flat but rough and carry tiny asperities which are compressed due to internal stress σ_{int} in the solid which is acting on this

rough interface (Figure 4.2 (a)). The normal stress of an ultrasonic wave $\sigma_{xx}(t)$ alternates this equilibrium stress state (Figure 4.2 (b)). At the tops of the asperities, small contact spots develop which represent the real area of contact. This real area of contact is much smaller than the nominal contact area of the whole interface.

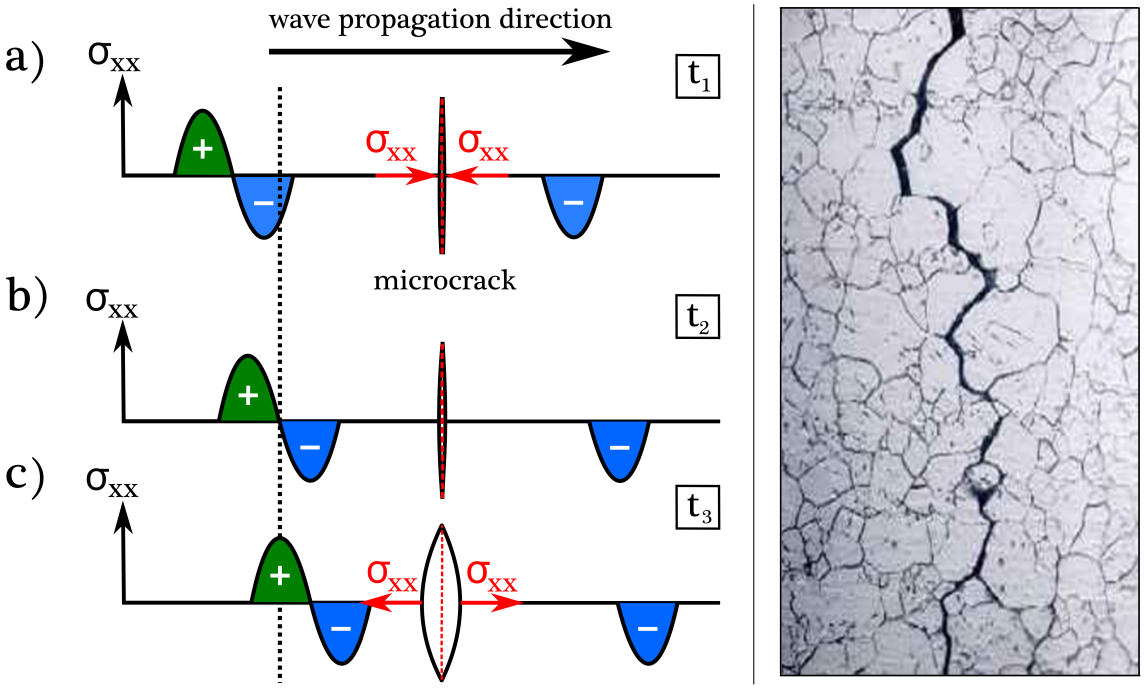

Figure 4.1: Schematic of a closed microcrack compressed under compressional stress (−) and opened under tensile stress (+) ($t_1 < t_2 < t_3$) (left) and micrograph of a real intergranular SCC microcrack at 500x magnification (right) [12].

As a result of the perturbative Rayleigh wave normal stress, the real area of contact becomes greater and smaller, i.e. the asperities on the crack faces become more and less deformed. This implies that only in an extreme case of very high amplitude incident waves, the internal stress is overcome, the crack faces totally separate and the so-called "clapping" of crack faces may occur.

Against the background of investigating the dependency of acoustic nonlinearity from microcracks on parameters such as crack density, we choose the finite element method (FEM) to perform numerical studies. FEM modeling has been shown in previous works to be a valuable method to numerically describe wave propagation and the

interaction with defects ([15], [32]). After studying the suitability of built-in features in ABAQUS to model microcracks, e.g. finite elements which do not support any tensile stiffness ("bimodular stiffness elements"), this research takes another approach for numerically modeling microcracks. Since built-in features seem to be too rigid to describe the actual nature of the problem, their use is fundamentally limited.

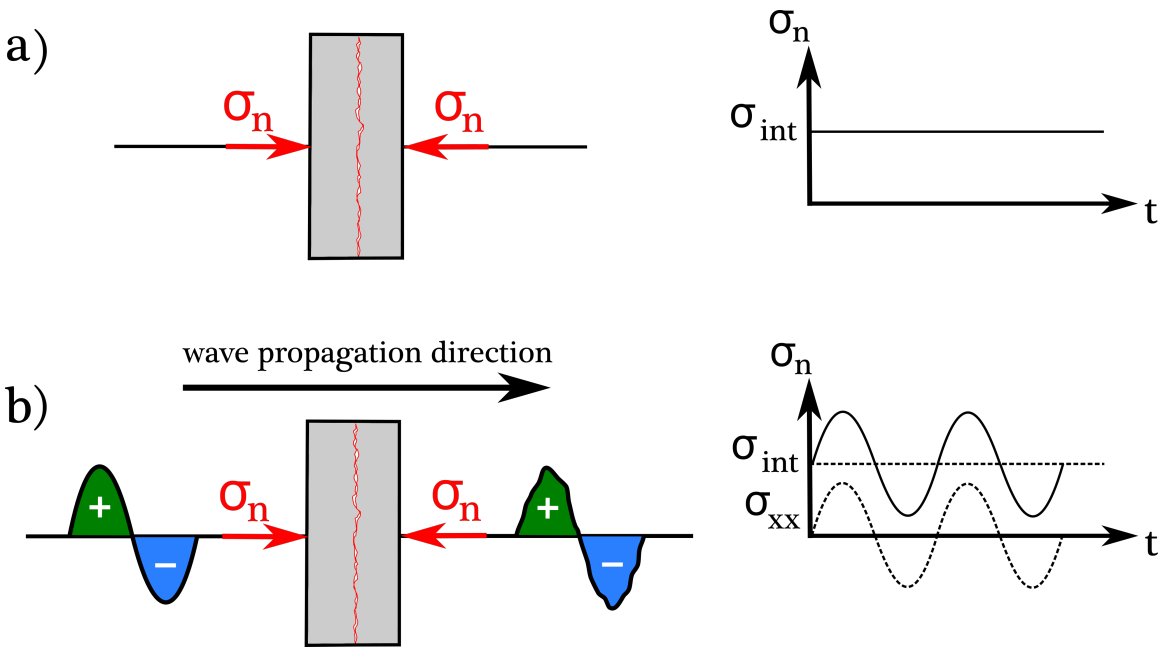

Figure 4.2: Schematic of a single microcrack under (a) an internal stress σ_{int} and (b) an internal and an additional perturbative stress $\sigma_{xx}(t)$ of an ultrasonic wave which gets distorted due to the nonlinear dynamics of the microcrack.

Therefore, we describe a microcrack by an "effective stress-strain relationship" which mimics the gross effect this microcrack has on incident Rayleigh surface waves. The effective stress-strain relationship results from a weighted average of local stress-strain relationships describing different states of contact along the crack path. This is valid when the wavelength is much greater than the size of microcracks and the microcracks are uniformly distributed in the material. Since the properties of the microcrack are averaged, our model can also be understood as describing distributed microcracks with each microcrack as a whole being in a different state of contact.

4.1 Effective Stress-Strain Relationship

A microcrack is assumed to have different states of contact along its crack path. Each contact state is described by a particular local stress-strain relationship accounting for the specific contact properties in these parts of the crack. One stress-strain relationship accounts for – due to internal stress – the fully-closed parts of the crack, whereas another local stress-strain relationship accounts for the fully-opened parts of the crack. A third local stress-strain relationship accounts for crack parts in which asperity contact takes place.

In this third case, the perturbative normal stress $\sigma_{xx}(t)$ of a Rayleigh wave alternates the contact normal stress σ_n between the two extrema of 1) the internal stress plus the ultrasonic normal stress and 2) the internal stress minus the ultrasonic normal stress (Figure 4.2 b)).

The following sections summarize the assumptions of the chosen rough surface contact model which is used to derive the nonlinear stress-strain relationship accounting for asperity contact crack parts. Moreover, the local stress-strain relationships describing the different contact states along the crack path are discussed in more detail.

4.1.1 Model Assumptions and Justifications

A1 Microcracks are small compared to the wavelength of the Rayleigh surface waves (ratio $\frac{\lambda_R}{crackdepth} \approx 50$).

⇒ Assumption 1 is plausible since typical lengths of microcracks are on the order of micrometers, whereas the Rayleigh wavelength is in the millimeter range for the frequency (f = 2MHz) typically used in the experiments by Marino et al. [26] and Thiele et al. [41].

A2 No bulk deformation occurs due to deformation of asperities. The deformation of one asperity does not effect the deformation of a neighboring asperity.

⇒ Assumption 2 is valid if contact spots are small compared to the distance

between neighboring asperities. This is a good approximation since most often, as can be seen also in this research, the real contact area is a small fraction of the nominal contact area [16].

A3 Only the linear contribution of the lattice structure is considered. Therefore, the single source of acoustic nonlinearity is the nonlinear dynamics of the microcrack.

⇒ Assumption 3 is reasonable since the acoustic nonlinearity caused by microcracks has been reported by many authors ([9], [11], [40]) to be much higher than the classical material nonlinearity.

A4 Asperity tops have the shape of hemispheres of equal radii and act as elastic bumps.

⇒ Assumption 4 is chosen in accordance to the classical rough surface contact model of Greenwood and Williamson [18] which builds upon the Hertzian contact theory [42].

A5 The asperity top heights are randomly distributed following a χ^2-probability density function.

⇒ Assumption 5 is chosen in order to mathematically describe the stochastic nature of rough surfaces. A χ^2-probability density function has been found to be a more realistic distribution function than exponential and Gaussian distribution functions (Kim et al. [24]).

4.1.2 Contact State 1: "Fully-Closed"

Contact state 1 accounts for all crack parts in which the asperities perfectly fit into each other (Figure 4.3 (left)), e.g. in freshly cracked parts. This contact state in which the two crack faces are assumed to be perfectly matched due to internal stress in the solid is described by a linear stress-strain relationship

$$\sigma_1(\epsilon) = E\epsilon. \tag{56}$$

These parts remain fully-closed even under an incident Rayleigh wave.

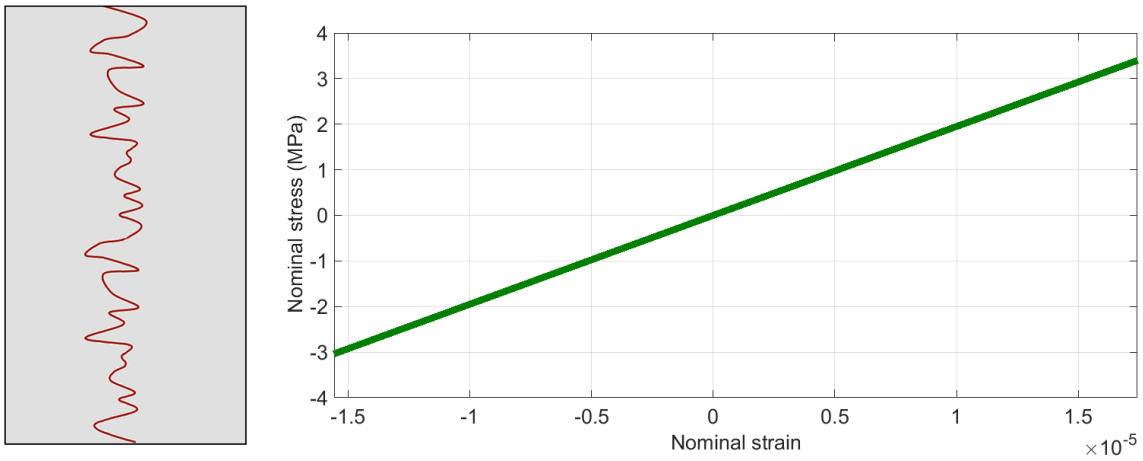

Figure 4.3: Schematic of fully-closed crack parts (left), linear stress-strain relationship describing these crack parts (right).

4.1.3 Contact State 2: "Fully-Opened"

Contact state 2 accounts for all parts of the microcrack which remain permanently open (Figure 4.4 (left)). As a result, neither normal nor shear stresses are transmitted across the crack faces (Equation 57) and the local stress-strain relationship describing these crack parts becomes

$$\sigma_2(\epsilon) = 0. \tag{57}$$

These parts remain fully-opened even under an incident Rayleigh wave.

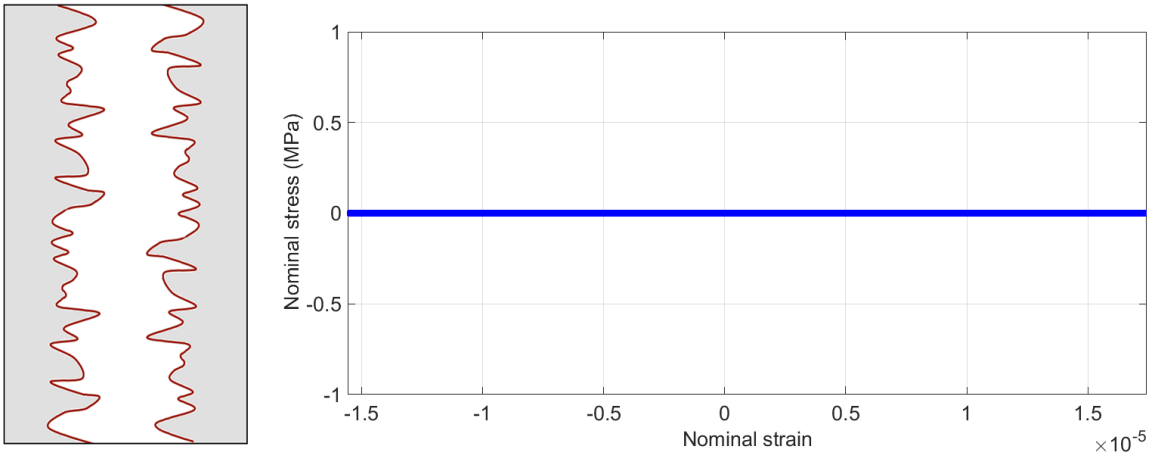

Figure 4.4: Schematic of fully-opened crack parts (left), zero stress transmission in these crack parts (right).

4.1.4 Contact State 3: "Asperity Contact"

Contact state 1 and 2 define the two extrema of fully-closed and fully-opened crack parts. Thus, in the remaining parts of a microcrack the crack faces are separated by a distance which allows for asperity contact. Due to for example, the corrosion process on stress-corroded crack faces, the asperities do not match. Internal stress in the solid brings the asperities into contact and small plastic deformation occurs at the asperity tops which form small contact spots. The incident ultrasonic wave perturbs this equilibrium state and periodically increases and decreases the real contact area.

4.1.4.1 Rough Surface Contact Model

Based on the work of Greenwood and Williamson [18] on the elastic contact of hemispherical asperities, this section discusses the derivation of the nonlinear stress-strain relationship

$$\sigma_3(\epsilon) = C(\epsilon)\epsilon \tag{58}$$

accounting for asperity contact crack parts. Following the schematic in Figure 4.5 (top) we assume asperity contact crack parts to be composed of two rough surfaces having RMS ("root mean square") roughness values of σ_{rms_1} and σ_{rms_2} respectively.

The RMS roughness σ_{rms} is defined in [14] as the root over the average of all squared distances y_i of the rough surface profile measured from a mean height level (Figure 4.6)

$$\sigma_{rms} = \sqrt{\frac{1}{n}\sum_{i=1}^{n} y_i^2}. \tag{59}$$

The problem of two rough surfaces in contact can be transformed into the problem of a "composite" surface, which has the relative profile of the two rough surfaces prior to contact, in contact with a smooth, rigid surface (Figure 4.5 (upper middle)). The RMS roughness of the composite surface σ_{comp} is defined as

$$\sigma_{comp} = \sqrt{\sigma_{rms_1}^2 + \sigma_{rms_2}^2}. \tag{60}$$

The tops of the contacting asperities form small contact spots and get deformed by the internal stress σ_{int} in the solid (Figure 4.5 (bottom)). The required force to deform a single asperity is based on the Hertzian equations [42]

$$f = \frac{4}{3} E^* \sqrt{a} \sqrt{\delta^3}, \tag{61}$$

with E^* being the "plane-stress modulus" [18] defined as

$$\frac{1}{E^*} = \frac{1-\nu_1^2}{E_1} + \frac{1-\nu_2^2}{E_2} \tag{62}$$

which becomes in our case of an elastic surface in contact with a rigid surface ($E_2 \to \infty$)

$$E^* = \frac{E_1}{1-\nu_1^2}. \tag{63}$$

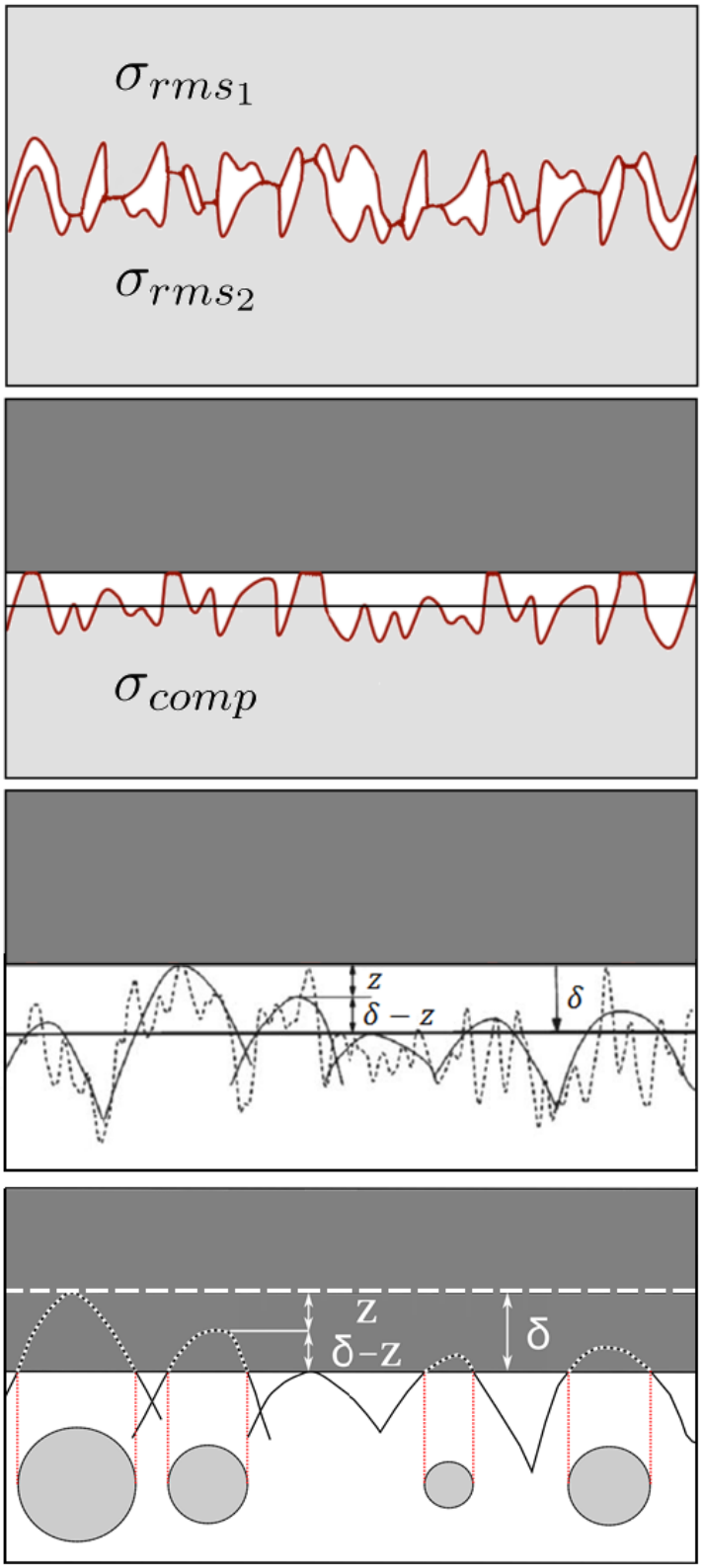

Figure 4.5: Two rough surfaces in contact (top); "Composite surface" of one rough surface, with the effective profile of two rough surfaces, in contact with a smooth rigid surface (upper middle); Definition of hemispherical asperities (lower middle) [25]; Hemispheres building contact spots when deformed (bottom).

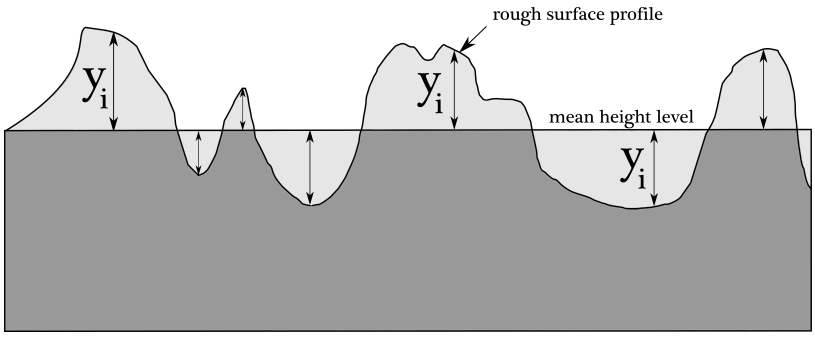

Figure 4.6: Schematic of a rough surface profile to define the RMS roughness value.

Variable a in Equation 61 is the radius of the hemispherical top of the asperity. Kim et al. [24] reconstructed this radius from RMS roughness values for the case of a composite surface from the experimentally obtained ultrasonic interfacial stiffness using a nonlinear least-squares optimization. Note, that δ in Equation 61 is the approach of the smooth, rigid surface towards the rough surface (Figure 4.5 (lower middle)). The coordinate axis z is attached to the top of the highest asperity and points inwards the rough surface.

The stochastic distribution of asperity top heights on the composite surface is described by the χ^2-probability density function (PDF) $\phi(\xi, z)$, in which ξ are the degrees of freedom (Figure 4.7).

The χ^2-probability density function is chosen because of its advantages over exponential and Gaussian distributions. Asperities distributed according to a χ^2-PDF have a finite maximum height, as a real surface has. In contrast, exponential and Gaussian distributions have a finite probability of finding an asperity at an infinite height [8]. Equation 64 describes the χ^2-PDF as it is introduced by Kim et al. [24]. One of the fundamental difficulties in the modeling of rough surfaces is the choice of appropriate parameters to characterize their roughness. In contrast to the rough surface description Nazarov and Sutin [30] used, which requires the problematic choice of a characteristic asperity height, our model using a χ^2-PDF requires RMS roughness values which can be measured by means of a profilometer.

The probability density function is described by

$$\phi(\xi; z) = \sqrt{\frac{\xi}{2}} \frac{1}{\sigma_{comp}} \frac{\left(\sqrt{\frac{\xi}{2}} \frac{z}{\sigma_{comp}}\right)^{\frac{\xi-2}{2}}}{\Gamma\left(\frac{\xi}{2}\right)} e^{-\sqrt{\frac{\xi}{2}} \frac{z}{\sigma_{comp}}} \tag{64}$$

in which Γ stands for the Gamma function, an extension for non-integers of the well-known factorial function. As a next step it is essential to set the approach δ by which the plane, rigid surface moves towards the composite surface, in relation to the generated asperity stress due to this approach. In order to relate these two quantities, we calculate the required load P to deform the distributed asperities by an approach δ according to

$$P = \eta A_{nom} \int_0^{\delta} f(\delta - z)\phi(\xi; z)\mathrm{d}z \tag{65}$$

in which η is the number density of asperities and A_{nom} is the nominal contact area. We perform the integration in Equation 65 numerically using MATLAB. Note that for an approach δ the force contribution of a specific asperity in a depth z is $f(\delta - z)$ (Figure 4.7).

Having defined the required load P to cause a specific approach δ, the generated asperity stress σ_{asp} follows by dividing the load P by the nominal contact area A_{nom} and inserting a minus to account for the fact that this nominal pressure P/A_{nom} causes a compressive asperity stress ("reactive asperity stress")

$$\sigma_{asp} = -\frac{P}{A_{nom}} = -\eta \int_0^{\delta} f(\delta - z)\phi(\xi; z)\mathrm{d}z. \tag{66}$$

Figure 4.8 shows both the nominal pressure P/A_{nom} and the reactive asperity stress σ_{asp} in dependency of the approach δ. In the equilibrium state, the following equation holds

$$\frac{P}{A_{nom}} + \sigma_{asp} = 0. \tag{67}$$

Let us now develop an estimate for the internal stress σ_{int}. A theory for plane cracks can be found in Sneddon [39].

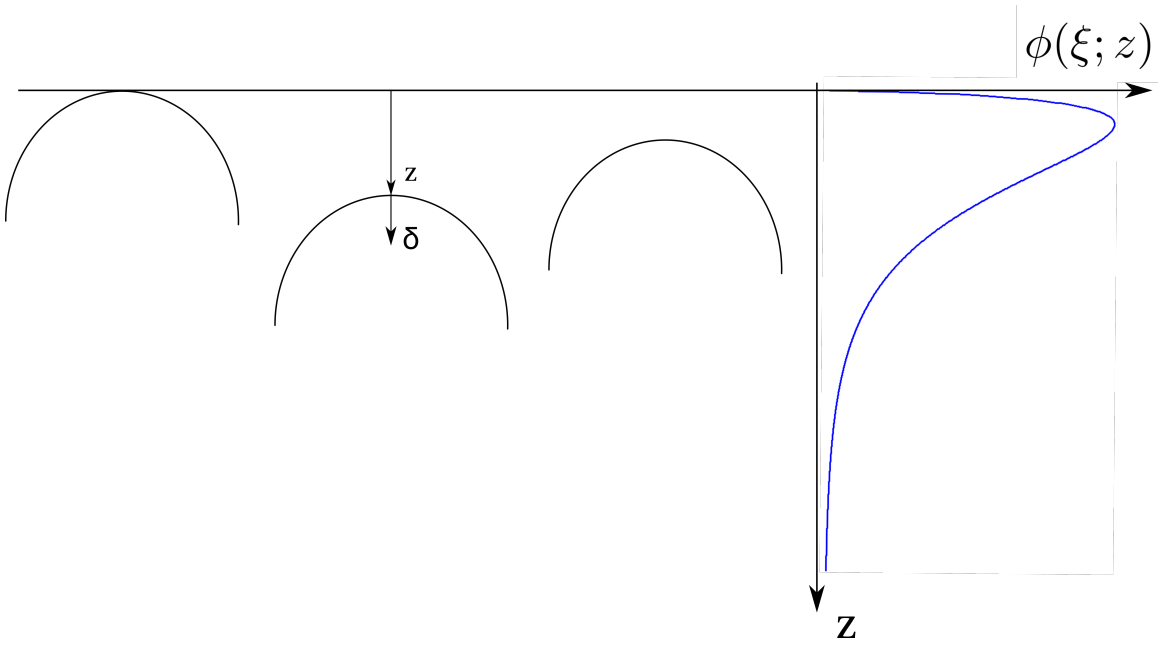

Figure 4.7: Exemplary hemispherical asperity tops distributed following a χ^2- probability density function.

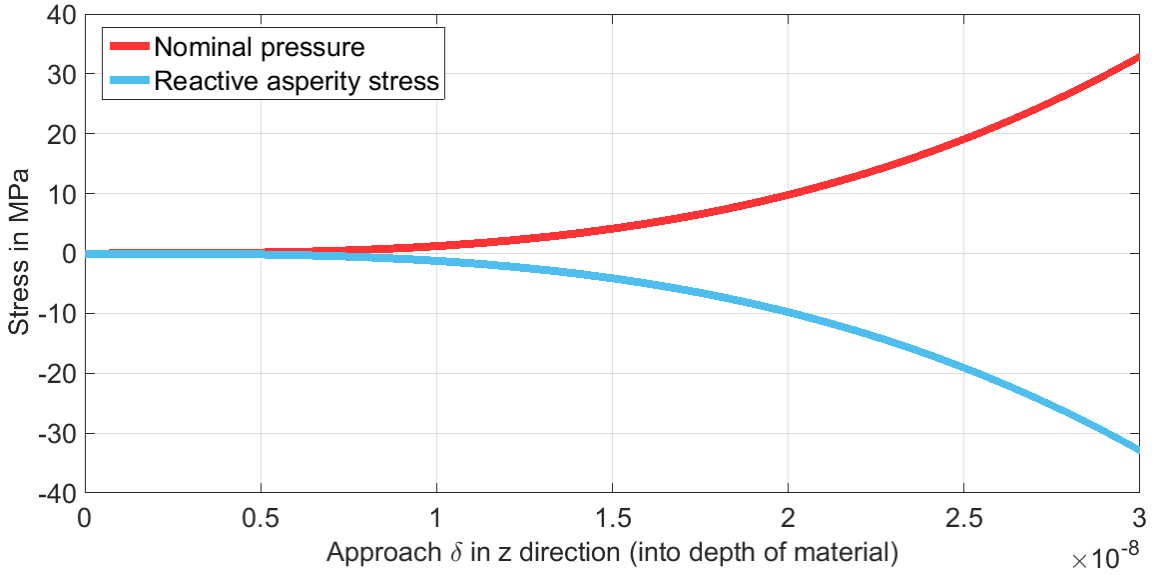

Figure 4.8: Nominal pressure P/A_{nom} and reactive asperity stress σ_{asp} for the following choice of rough surface model parameters: 260 asperities per nominal contact area, $E = 195$ GPa, $\nu = 0.305$, $\sigma_{rms} = 0.8$ μm (chosen in the range of RMS roughness values for rough interfaces [24], needs further experimental characterization), a $= \sigma_{rms}/(1.2\text{E-}3)$, $\xi = 3$.

According to this theory, the normal displacement $u_n(r)$ of crack surfaces in dependency of the radial crack coordinate r as reaction to a stress σ_o which tries to open the crack is

$$u_n(r) = \frac{4(1-\nu^2)}{\pi E}\sqrt{R^2 - r^2}\sigma_o. \tag{68}$$

Furthermore, the volume V_{crack} of a single crack is

$$V_{crack} = \frac{16(1-\nu^2)}{3E}R^3\sigma_o. \tag{69}$$

Let us now assume that this theory is also valid for rough crack surfaces [10]. The internal stress in the solid σ_{int} is $\sigma_{int} = -\sigma_o$ and tries to close the crack. With the crack volume $V_{crack} = \pi R^2\delta_s$ and the equilibrium crack separation distance δ_s we get an estimate for the internal stress σ_{int} in the solid

$$\sigma_{int} = -\frac{3\pi E\delta_s}{16R(1-\nu^2)}. \tag{70}$$

(Example: $\delta_s = 3$ nm, E = 195 GPa, R = 40 μm, $\nu = 0.305$, $\sigma_{int} = -9.9984$MPa). Note that for the next step, the equilibrium crack separation distance δ_s defines the working point for the perturbative stress of the incident ultrasonic Rayleigh wave. Any additional perturbative stress acting along with the internal stress in the solid slightly increases and decreases the real contact area. As mentioned earlier, during the compressional phase, the real contact area is increased, while during the tensile phase the real contact area is decreased. In case of extremely large ultrasonic wave amplitudes the real area of contact becomes zero, meaning that the crack faces separate from each other. This "clapping" effect of crack faces is known to cause tremendously high acoustic nonlinearity ([9], [40]).

The equilibrium state defines the working point for the derivation of the local stress-strain relationship accounting for asperity contact crack parts. Later on, this working point is set to be zero stress and zero strain to fit into the framework of a Mooney-Rivlin hyperelasticity model.

We now assume an additional loading by an incident ultrasonic Rayleigh wave (Figure 4.9). Thereby, the applied stress $\sigma_{appl}(t)$ on the interface is the sum of the internal stress σ_{int} and the perturbative normal stress $\sigma_{xx}(t)$ of the incident ultrasonic Rayleigh wave

$$\sigma_{appl}(t) = \sigma_{int} + \sigma_{xx}(t) = \sigma_{asp}(t). \tag{71}$$

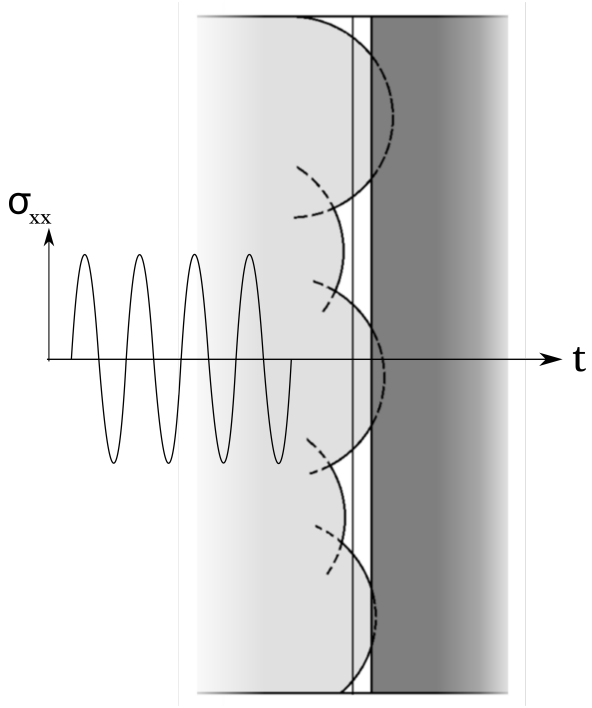

Figure 4.9: Compressed interface under perturbative stress $\sigma_{xx}(t)$ of an ultrasonic Rayleigh wave.

Then the nonlinear stress-strain relationship due to asperity contact is derived as it can be seen in Figure 4.10. Note that the origin of the z axis now is in a depth of 30 nm and the axis points outward of the rough composite surface.

This coordinate transform is required because of a sign convention for compressional stresses in ABAQUS.

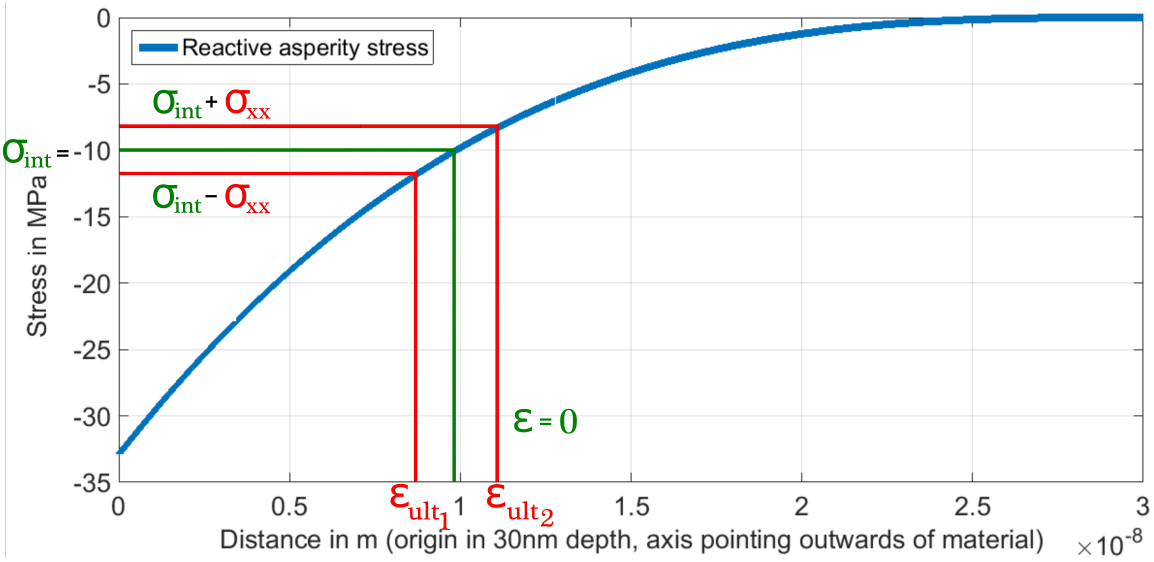

Figure 4.10: Generated asperity stress in dependency of approach δ.

Let us assume an internal stress $\sigma_{int} = -10$ MPa acting on the interface. Thus, the composite surface becomes compressed by an approach $\delta \approx 20.1$ nm. The additional ultrasonic stress $\sigma_{xx}(t)$ perturbs this equilibrium state. We now define the working point to be zero stress and zero strain. Furthermore, we portion the nominal strain caused by the Rayleigh wave in a linear medium proportionately to the asymmetric stress-displacement characteristic of the asperity contact and get the two intervals $(\epsilon - \epsilon_{ult_1})$ and $(\epsilon_{ult_2} - \epsilon)$. Due to this transition from the stress-displacement relationship to a stress-strain relationship, we get the nonlinear stress-strain relationship describing asperity contact crack parts as can be seen in Figure 4.11.

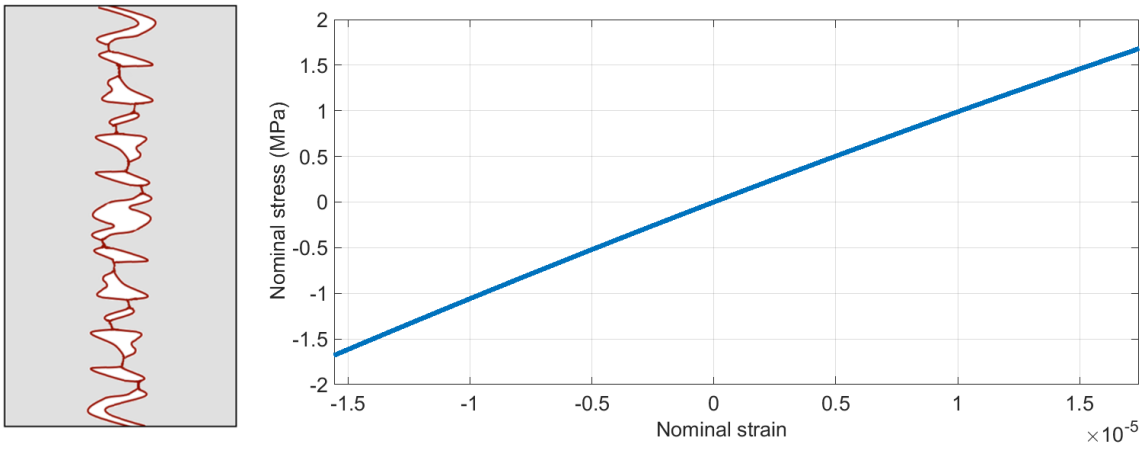

Figure 4.11: Nonlinear stress-strain relationship describing asperity contact crack parts.

The derivation of the effective stress-strain relationship which describes the whole crack is now straightforward. We get it by taking a weighted average of the three local stress-strain relationships in Figure 4.12 (Contact state 1, 2, and 3).

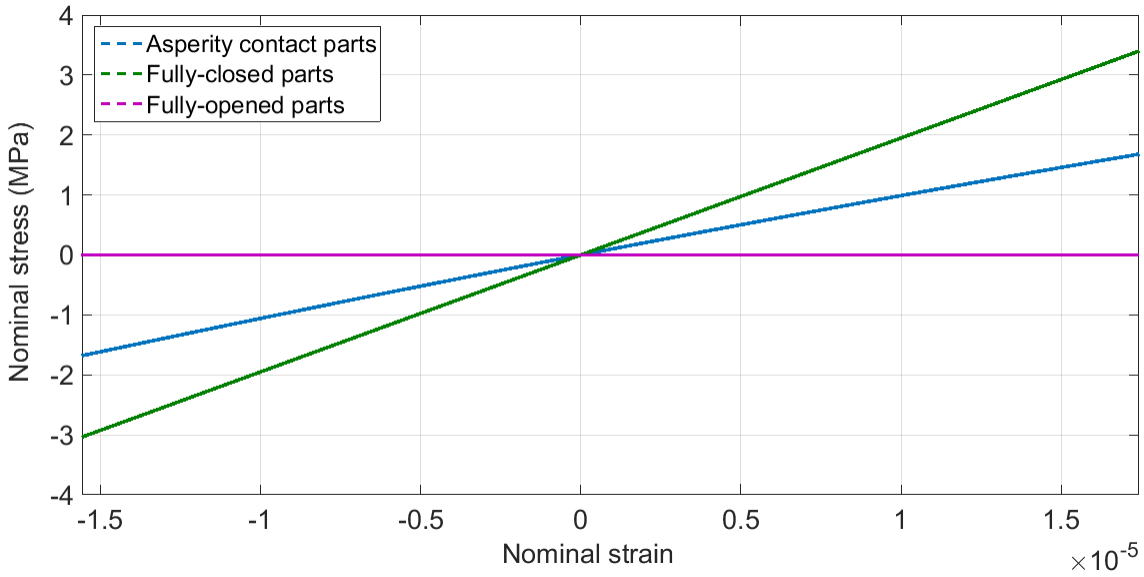

Figure 4.12: Three local stress-strain relationships describing the three different states of contact.

4.1.5 Weighted Average of Local Stress-Strain Relationships

We obtain the effective stress-strain relationship as a weighted average (Equation 72) of the three local stress-strain relationships derived in previous sections

$$\begin{aligned}\sigma(\epsilon) &= \sum_{i=1}^{3} w_i f_i(\epsilon) \\ &= w_1 f_1(\epsilon) + w_2 f_2(\epsilon) + w_3 f_3(\epsilon) \qquad \text{with} \qquad \sum_i w_i = 1.\end{aligned} \tag{72}$$

State 1: "Fully-closed"

State 2: "Fully-opened"

State 3: "Asperity contact"

Figure 4.13 shows an exemplary effective stress-strain relationship for 50% fully-closed crack parts, 50% asperity contact crack parts, and 0% fully-opened crack parts.

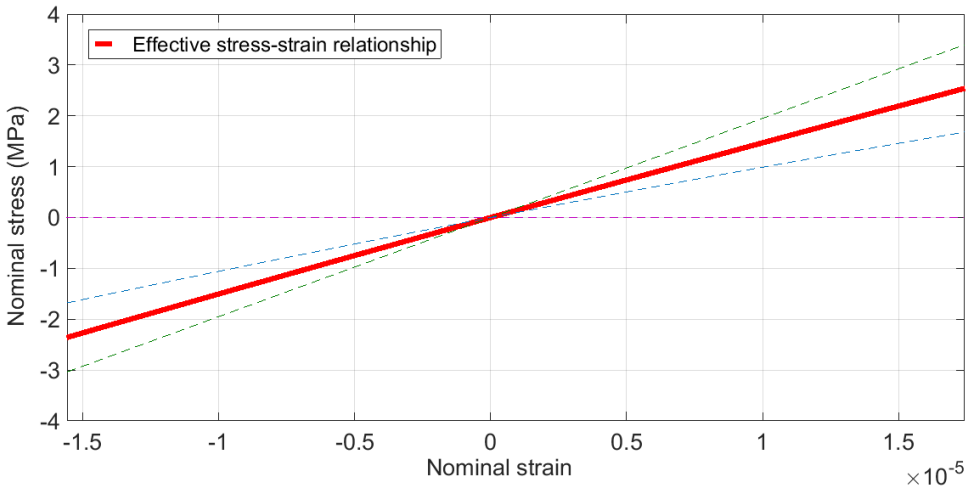

Figure 4.13: Effective stress-strain relationship for 50% fully-closed crack parts, 50% asperity contact crack parts and 0% fully-opened crack parts.

Having obtained the effective stress-strain relationship of a single microcrack, the next step is to implement this stress-strain relationship in a FE-model to perform studies on the generated acoustic nonlinearity by distributed microcracks. For stability reasons and since it fits the effective stress-strain relationship the best, a polynomial hyperelasticity material model of order 1, i.e. the Mooney-Rivlin hyperelasticity

model, is chosen. A least-squares optimization in ABAQUS is used to obtain the input parameters for the Mooney-Rivlin model to fit the desired material behavior. Figure 4.14 (top) shows both the effective and the optimized hyperelastic stress-strain relationship. In Figure 4.14 (bottom), the error between the two stress-strain relationships is shown. As can be clearly seen, the error is negligible small. Therefore, it can be said that the effective stress-strain relationship follows the Mooney-Rivlin nonlinear hyperelastic behavior.

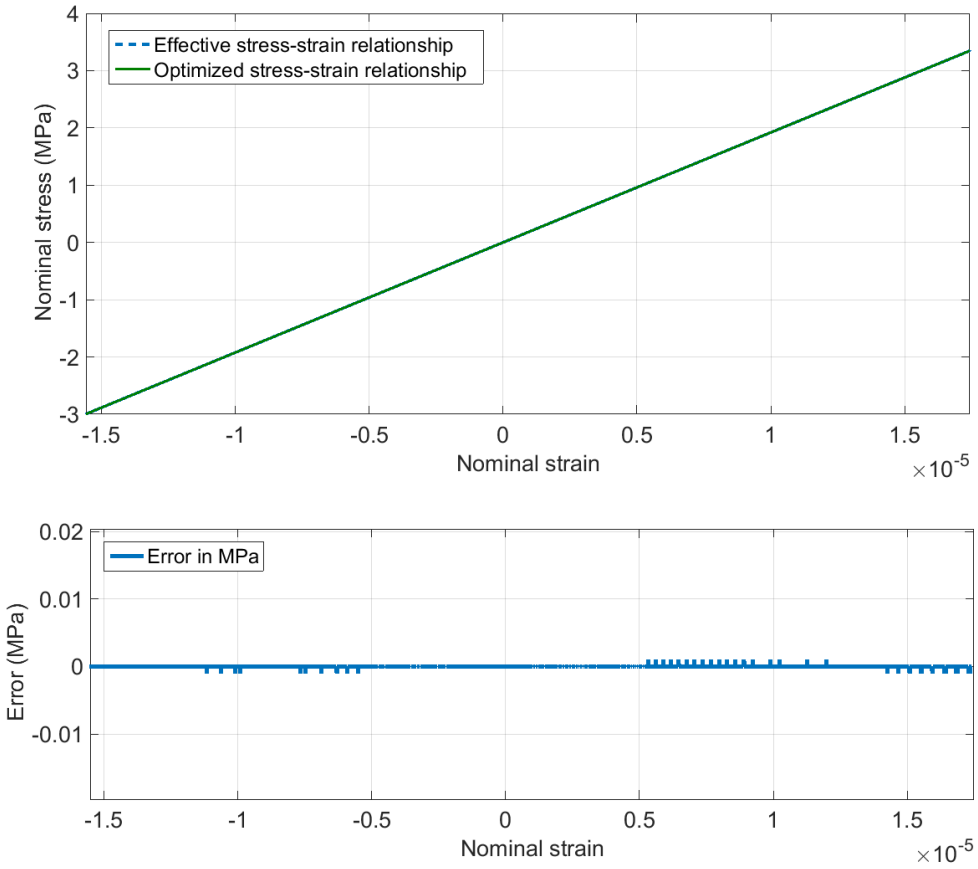

Figure 4.14: Comparison of effective stress-strain relationship and optimized hyperelastic stress-strain relationship (top) and error in MPa (bottom).

In order to qualitatively compare our results for the dependency of acoustic nonlinearity on crack density, we introduce the nonlinearity parameter β_{crk} as proposed by Cantrell [10].

Cantrell uses the rough surface contact model proposed by Nazarov and Sutin [30] to derive the acoustic nonlinearity from randomly distributed penny-shaped cracks in a solid. In summary, β_{crk} becomes

$$\beta_{crk} = \frac{\beta' N_{crk}}{7}\left(1 + \left(\frac{\alpha' N_{crk}}{5}\right)\right)^{-2} \tag{73}$$

in which the elastic crack coefficients α' and β' are dependent on contact model parameters

$$\begin{aligned} \alpha' &= \frac{16 h_s R^3 (1-\nu^2)}{3 d_s}\left(1 + \frac{h_s}{d_s}\right)^{-1} \\ \beta' &= \frac{256 h_s R^4 (1-\nu^2)^2}{9\pi {d_s}^2}\left(1 + \frac{h_s}{d_s}\right)^{-3}. \end{aligned} \tag{74}$$

N_{crk} is the crack density, h_s the characteristic asperity height and R the radius of the penny-shaped cracks Cantrell proposed. Figure 4.15 shows β_{crk} (Equation 73) for relatively small crack densities.

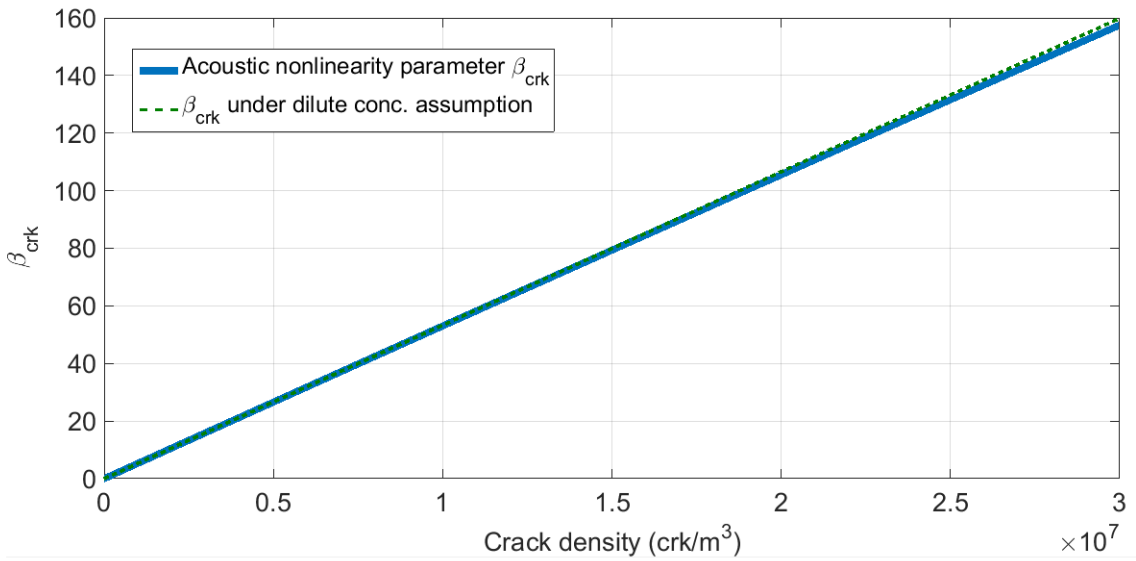

Figure 4.15: Acoustic nonlinearity parameter β_{crk} [10] for small crack densities (chosen contact model parameters: crack equilibrium separation $d_s = 30$nm, Poisson's ratio $\nu = 0.25$, crack radius $R = 1$mm, characteristic asperity height $h_s = 10$nm).

Note that the dotted line (β_{crk} for dilute concentration of cracks) is calculated by only considering the term in front of the brackets in Equation 73. This is valid for small crack densities [10]. Having a dilute concentration of cracks, we observe an almost linear relationship between crack density and acoustic nonlinearity.

Figure 4.16 reveals that Cantrell's measure β_{crk} for acoustic nonlinearity is only additive for relatively small crack densities. Despite having been derived for longitudinal wave incidence, the same trends are observed for Rayleigh waves in Chapter 6.

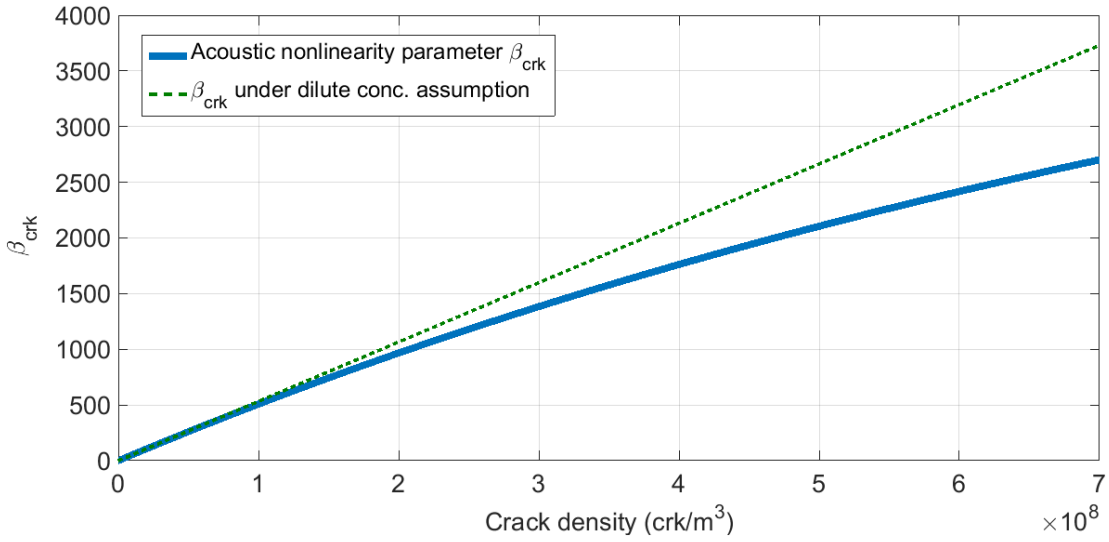

Figure 4.16: Acoustic nonlinearity parameter β_{crk} [10] for higher crack densities (chosen contact model parameters: crack equilibrium separation $d_s = 30$nm, Poisson's ratio $\nu = 0.25$, crack radius $R = 1$mm, characteristic asperity height $h_s = 10$nm).

Besides the normal stress $\sigma_{xx}(t)$ of the Rayleigh wave also its shear stress $\sigma_{xz}(t)$ acts on the interface and introduces a nonlinear friction mechanism, another type of CAN.

4.2 Frictional Interface under Rayleigh Wave Drive

Besides the previously investigated CAN generated by an imperfect interface under normal wave incidence, the interaction between an ultrasonic wave and a frictional interface is of special interest in NDE. A reason for that is the odd harmonic generation in an initially monochromatic ultrasonic wave by e.g. partially closed cracks which can be thus detected. Previous studies by Blanloeuil et al. [6] and Solodov et al. [40] focused on a frictional interface under a shear wave drive. In this research, the interaction of a Rayleigh wave with a frictional interface is investigated and studied numerically for distributed interfaces later on.

4.2.1 Normal Force in Different Contact States

In the framework of the last section about different opening states of a crack, in fully-closed crack parts the normal stress at the interface causes a normal force

$$F_{N1}(t) = \sigma_n(t) A_{C2} \tag{75}$$

with

$$\sigma_n(t) = \sigma_{int} + \sigma_{xx}(t) \tag{76}$$

and

$$A_{C1} = w_1 A_{nom}. \tag{77}$$

A_{C1} as a portion w_1 of the nominal contact area A_{nom} is the area of all crack parts in contact state 1. Moreover, fully-opened crack parts are not in contact (area of crack parts in contact state 2, $A_{C2} = 0$). Hence, no normal force can develop in these crack parts

$$F_{N2} = 0. \tag{78}$$

In asperity contact crack parts, a normal force

$$F_{N3}(t) = \sigma_n(t) A_{C3} \tag{79}$$

develops. Note that the real contact area is assumed to be constant. This assumption is valid when a high portion of the crack is fully-closed and the change in real contact area is small compared to A_{C1}.

Figure 4.17 (top) shows the real area of contact for the asperity contact crack parts. Moreover, Figure 4.17 (bottom) reveals an almost linear increase in real contact area over the nominal pressure acting on the interface.

4.2.2 Static Friction Force Threshold

We get the averaged normal force $\overline{F}_N(t)$ acting on the entire interface by taking the area-weighted average of all normal forces N_i in the contact states i (i=3)

$$\overline{F}_N(t) = \sum_{i=1}^{3} \frac{F_{N_i} A_{Ci}}{A_{nom}}. \tag{80}$$

Thus, the static friction force which has to be overcome to cause the interface to change from "sticking" (no transverse motion) to "slipping" (transverse motion) is

$$F_{R_{stat}}(t) = \mu_{stat} \overline{F}_N(t) \tag{81}$$

with the static friction coefficient $\mu_{stat} = 0.15$ for crack faces as approximately proposed by Bower [7]. Figure 4.18 shows the time-dependence of the averaged normal force $\overline{F}_N(t)$ and the static friction force threshold $F_{R_{stat}}(t)$.

This static friction force is a threshold friction force, which means that it is the maximum force the frictional interface can bear before it passes from "sticking" to "slipping".

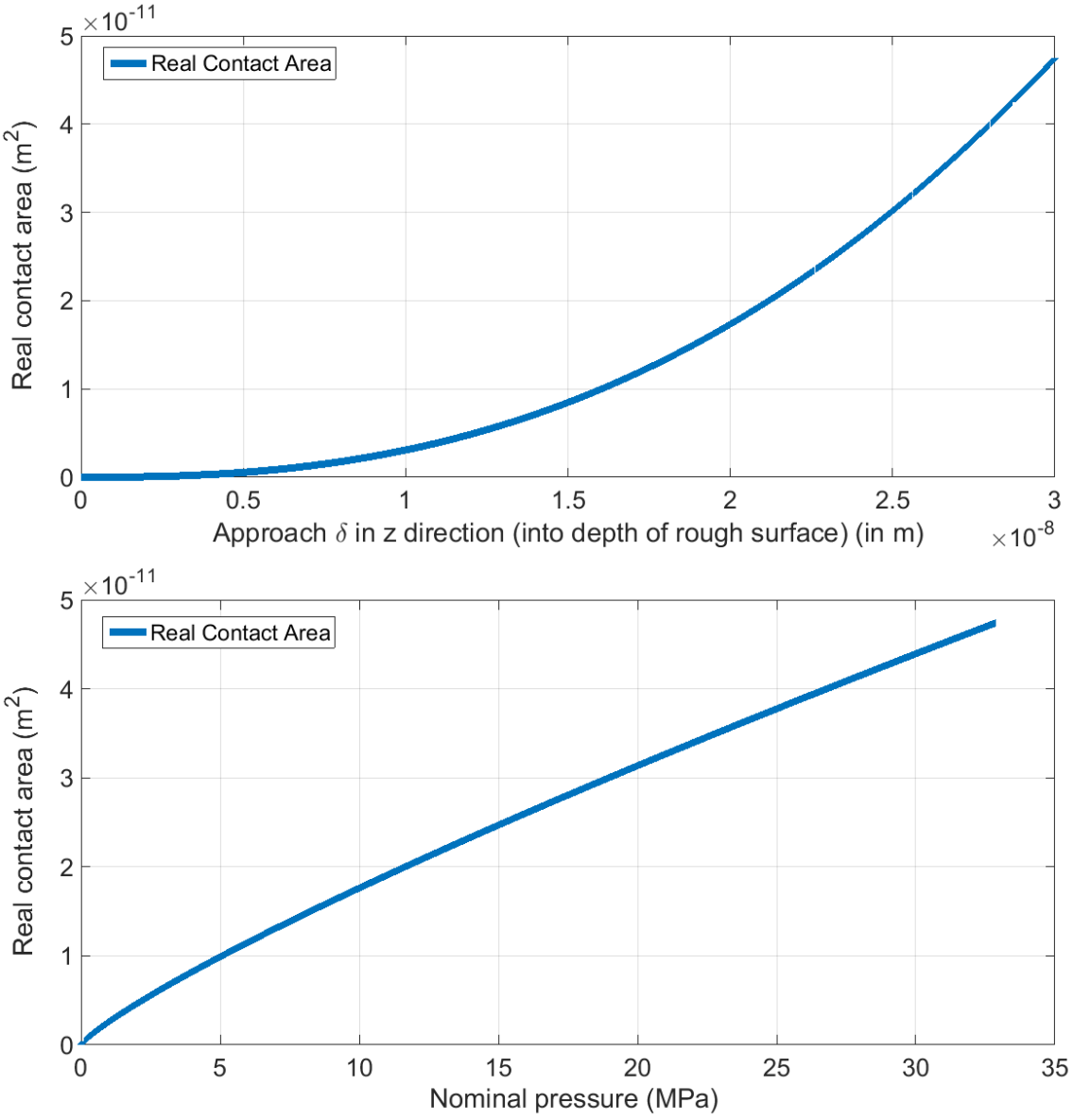

Figure 4.17: Real area of contact in dependency of approach δ (top) and real area of contact in dependency of nominal pressure at the interface revealing almost linear relationship.

4.2.3 Rayleigh Wave Shear Stress Component as Driving Force

The driving force of the interface is the shear stress of the Rayleigh wave which is time-dependent and at the stress-free surface delayed by 90° in phase relative to the Rayleigh wave normal stress $\sigma_{xx}(t)$.

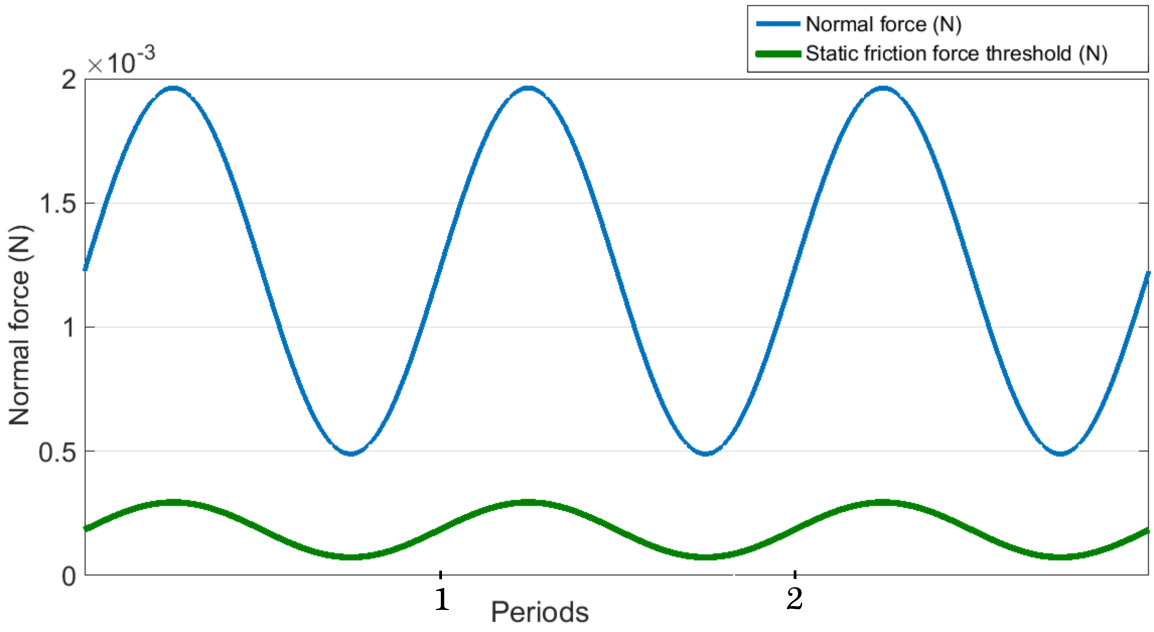

Figure 4.18: Averaged normal force $\overline{F}_N(t)$ and static friction force threshold $F_{R_{stat}}(t)$ for $w_1 = 0.97$, $w_2 = 0$, $w_3 = 0.03$, $\overline{\sigma}_{xx} = 1.2019$ MPa, $\overline{\sigma}_{xz} = 0.3172$ MPa, $\sigma_{int} = 2$ MPa, $\mu_{stat} = 0.15$, excitation amplitude 5 nm, crack depth 180 μm.

Figure 4.19 shows both the normal stress $\sigma_{xx}(t)$ of the Rayleigh wave and the Rayleigh wave shear stress $\sigma_{xz}(t)$, both for an exemplary point near the surface of the specimen in a depth of 72 μm.

Note that at this location, the normal stress is more than three times higher than the shear stress. Whenever the force due to the shear stress exceeds the threshold $F_{R_{stat}}(t)$, "slipping" of the frictional interface occurs, and vice versa.

Note that this threshold is valid for both directions along the interface. The force due to the Rayleigh wave shear stress $\sigma_{xz}(t)$ acting on the real area of contact is

$$F_{shear}(t) = \sigma_{xz}(t) A_{real} \tag{82}$$

with the real contact area A_{real} in this case being the sum of areas from all three area contributions of the different contact states

$$A_{real} = \sum_{i=1}^{3} A_{Ci}. \tag{83}$$

Directly at the surface the Rayleigh wave shear stress $\sigma_{xz}(t)$ is too small compared to the normal stress $\sigma_{xx}(t)$ to cause sliding of the interface, meaning that the sliding contribution for short surface-breaking cracks (e.g. $0 - 30$ μm) seems to be minor.

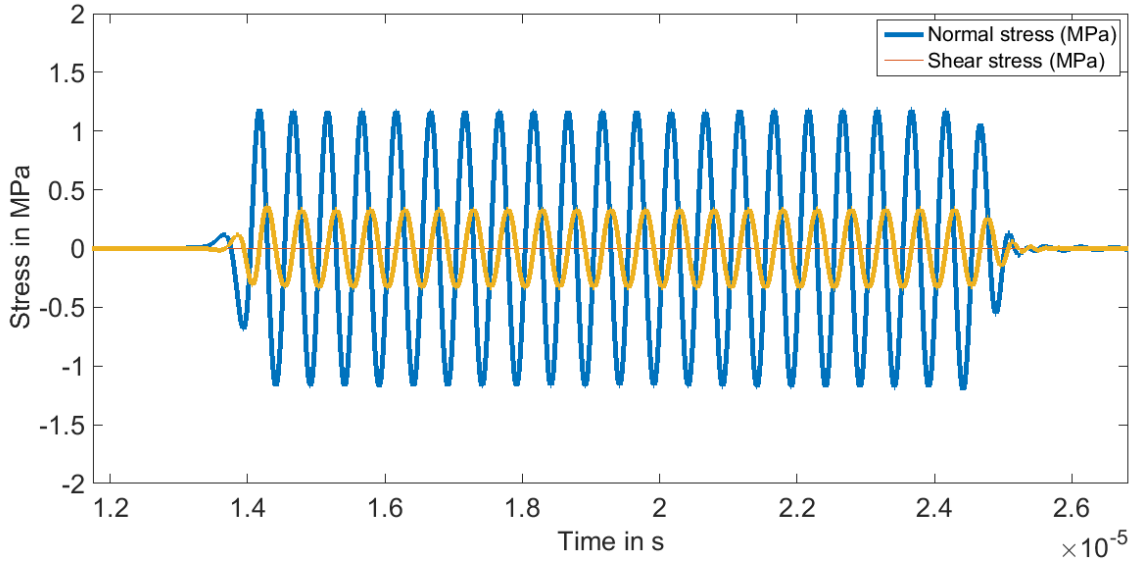

Figure 4.19: Rayleigh wave normal stress $\sigma_{xx}(t)$ and by 90° phase-delayed shear stress $\sigma_{xz}(t)$ at a point near the surface of the specimen.

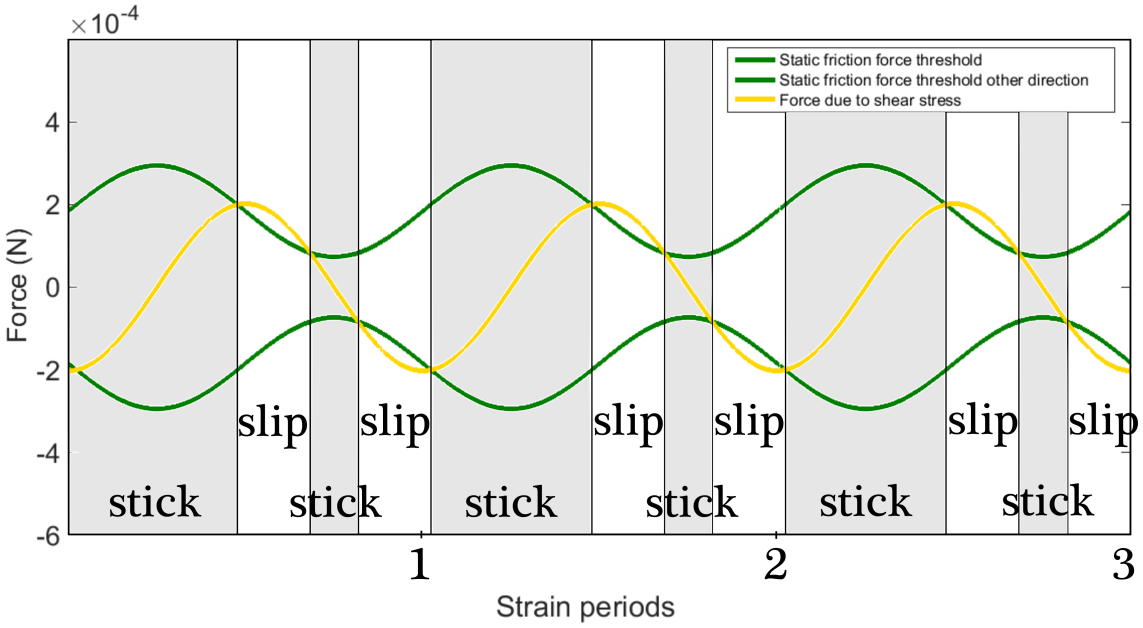

Figure 4.20: Static friction force threshold $F_{R_{stat}}(t)$ (in two directions) and force $F_{shear}(t)$ due to the Rayleigh wave shear stress. Bands indicate the states of "sticking" and "slipping".

However, for longer cracks (e.g. up to 180 μm) sliding could occur since by averaging the normal and shear stresses along the depth of the crack the averaged shear stress becomes big enough to cause sliding. The stresses are obtained at element integration points from an ABAQUS simulation.

The transverse motion of the interface causes a symmetrical variation of the tangential interface stiffness [34] twice over one input strain period (Figure 4.21). As a result, the Fourier spectrum of the received signal behind the frictional interface only shows odd harmonics. Once the static friction force threshold is overcome, the interface starts to slide and immediately a dynamic friction force $F_{R_{dyn}}(t)$ – an applied force – is acting against the motion. The dynamic friction force $F_{R_{dyn}}(t)$ can be calculated following Coulomb's law

$$F_{R_{dyn}}(t) = \mu_{dyn} F_N(t) \tag{84}$$

in which μ_{dyn} is the dynamic friction coefficient of the crack faces chosen to be $\mu_{dyn} = 0.1$.

Figure 4.21 shows a schematic of the hysteretic stress-strain relationship describing the frictional interface under stick-slip motion. Note that the tangential interface stiffness C_{stick} during the phases of sticking (2) and (4) is higher than the tangential interface stiffness C_{slip} during the phases of slipping (1) and (3). The ratio of the tangential interface stiffnesses C_{stick} and C_{slip} is assumed to be linearly proportional to the ratio of the static and dynamic friction coefficients μ_{stat} and μ_{dyn}. The determination of the exact relationship between these ratios needs further investigations.

The following chapter presents a FE-model which is used to numerically study the effect randomly distributed surface-breaking microcracks have on higher harmonic generation in Rayleigh surface waves.

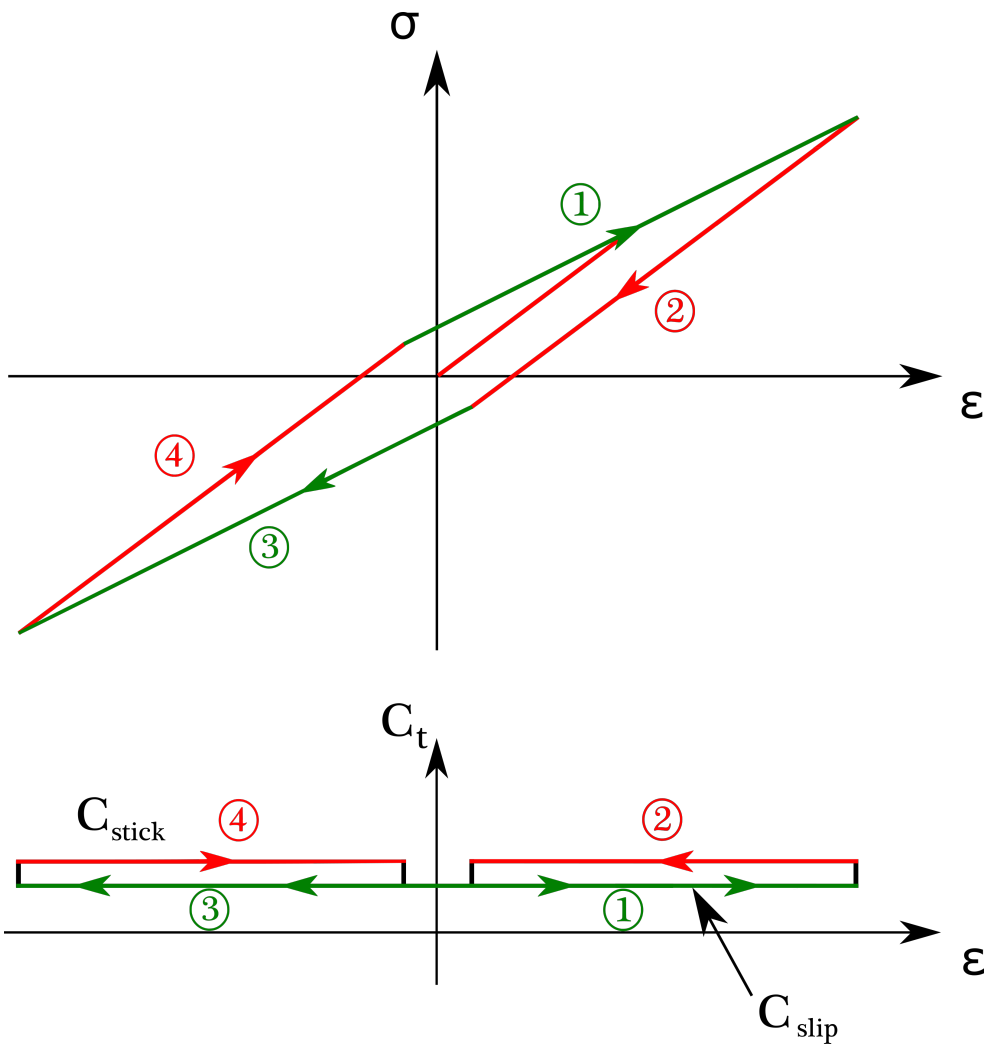

Figure 4.21: Schematic showing the hysteretic stress-strain relationship describing the interface under stick-slip motion and the symmetrical variation of the tangential interface stiffness twice over one input strain period.

CHAPTER V

FINITE ELEMENT MODEL OF RANDOMLY DISTRIBUTED MICROCRACKS

In order to study the dependency of the acoustic nonlinearity parameter β on the microcrack parameters including crack density, different percentages of crack opening states and varying crack face roughnesses, we delevoped a two-dimensional finite element model. This chapter summarizes the most important properties of this FE-model. The two types of contact acoustic nonlinearity investigated in the previous chapter are studied separately. The effect of the Rayleigh wave normal stress $\sigma_{xx}(t)$ on the compressed interfaces – under an internal stress σ_{int} – is studied by assigning the effective stress-strain relationship (Chapter 4) to "crack elements," which are distributed elements at the surface of the specimen. Additionally, we developed another FE-model to study odd harmonic generation due to a nonlinear friction mechanism which we realized using a master-slave contact surface approach, constraining the opening of the contact and assigning a friction coefficient to the contact surfaces.

5.1 Finite Element Modeling - Normal Direction

The workflow to build the FE-model and perform the simulations is: (1) the geometry is built and a finite element mesh is generated using the preprocessor HyperMesh; (2) the node coordinates and element definitions are exported to an ABAQUS input file in which the analysis steps are defined in detail; and (3) the input file is submitted to the ABAQUS Explicit solver for a time-domain analysis.

The FE-model focuses on proper Rayleigh wave generation and the practical implementation of the effective stress-strain relationship derived previously.

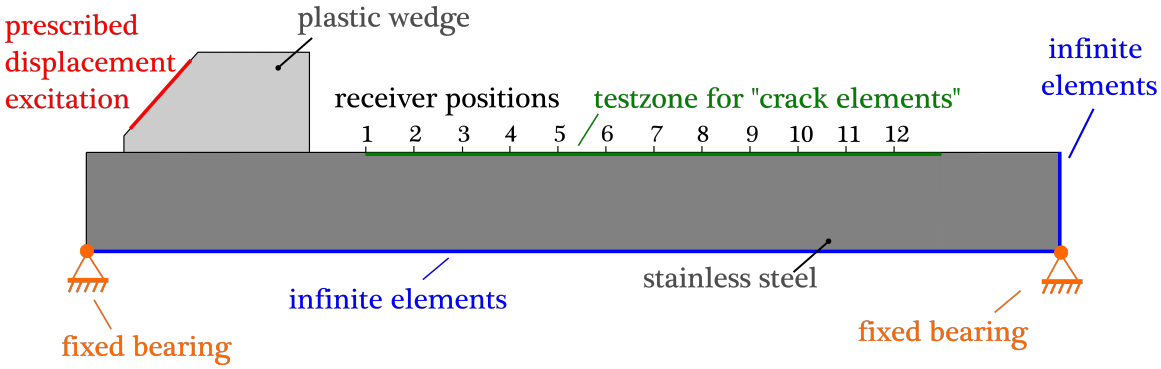

Figure 5.1: Schematic showing the wedge-specimen assembly including excitation, bearings, testzone for "crack elements" with receiver positions 1-12 and infinite elements.

As can be seen in Figure 5.1 the FE-model consists of a plastic wedge and a stainless steel specimen. In a fashion similar to the method used in experiments to excite Rayleigh surface waves, we excite longitudinal waves at the flank of the wedge and let them hit the boundary between wedge and specimen under the Rayleigh critical angle (Equation 37). Note that for Rayleigh wave generation the longitudinal wave velocity in the wedge has to be smaller than the Rayleigh wave velocity in the specimen. This leads us to the choice of materials for both wedge and specimen. The material properties of the wedge are taken from the COMSOL material library. Young's modulus and density of 304 stainless steel are taken from [3]. Poisson's ratio has been chosen in the range of values typical for steel found in various references.

5.1.1 Material

Since this analysis focuses solely on nonlinear effects from distributed microcracks, the wedge material is modeled as linear elastic. The material properties of the wedge can be found in Table 5.1.

Table 5.1: Material properties of acrylic plastic wedge

Description	Symbol	**Value**
Young's modulus	E	3.2 GPa
Poisson's ratio	ν	0.35
mass density	ρ	1190 kg/m^3
Lam*é* parameter[a]	λ	2.8 GPa
Lam*é* parameter[a]	μ	1.2 GPa
velocity P-wave[a]	c_{P1}	2077.5 m/s
velocity S-wave[a]	c_{S1}	998.0 m/s

[a]Calculated from listed properties

Furthermore, the specimen material properties of 304 stainless steel are listed in Table 5.2. Note that the coupling between the wedge and specimen is assumed as perfect, i.e. wedge and specimen share nodes at the boundary between them. Hence, the wedge and specimen are the same solid but have different material properties. This coupling condition is also desired in the experiments.

Table 5.2: Material properties of 304 stainless steel

Description	Symbol	**Value**
Young's modulus	E	195 GPa
Poisson's ratio	ν	0.305
mass density	ρ	8000 kg/m^3
Lam*é* parameter[a]	λ	116.9 GPa
Lam*é* parameter[a]	μ	74.7 GPa
velocity P-wave[a]	c_{P2}	5769.3 m/s
velocity S-wave[a]	c_{S2}	3055.9 m/s

[a]Calculated from listed properties

5.1.2 Excitation

The generation of longitudinal waves in the wedge is realized by a prescribed displacement boundary condition on the wedge flank. Figure 5.2 shows a schematic indicating waves which initiate at the nodes (yellow) and form an envelope wavefront (green) [47]. An excitation amplitude of 2 x 10^{-9} m is used to excite longitudinal waves in the wedge. This displacement value is in the range of experimentally obtained surface displacement amplitudes [5].

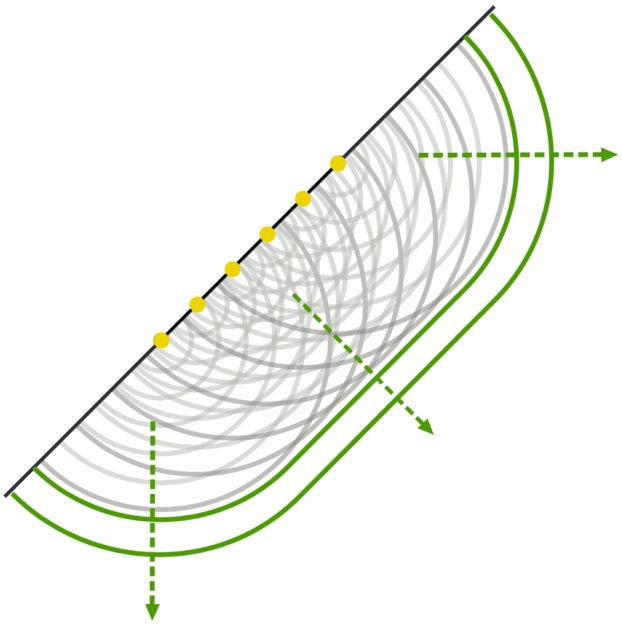

Figure 5.2: Assembly of point sources (yellow) along the excitation site and envelope wavefront (green) [47].

5.1.3 Boundary Conditions

As mentioned in the previous section, displacement boundary conditions at the excitation node set are used to initiate the elastic longitudinal stress perturbations in the wedge. Additionally, the translational degrees of freedom of the nodes in the lower left and right corners of the specimen (Figure 5.1) are constrained to be zero in order to prevent moving of the assembly as a whole (rigid body motions).

5.1.4 Implementation of Nonlinear Material Behavior

After deriving the effective stress-strain relationship, a way is needed to implement this stress-strain relationship into ABAQUS. Since the shape of the effective stress-strain relationship is similar to stress-strain relationships of hyperelastic materials, various hyperelastic materials are investigated regarding their suitability to fit the effective stress-strain relationship. For stability reasons and since it fits the desired material behavior the best, we select a Mooney-Rivlin hyperelasticity model. In order to fit the input parameters for this material model, we use ABAQUS to perform a

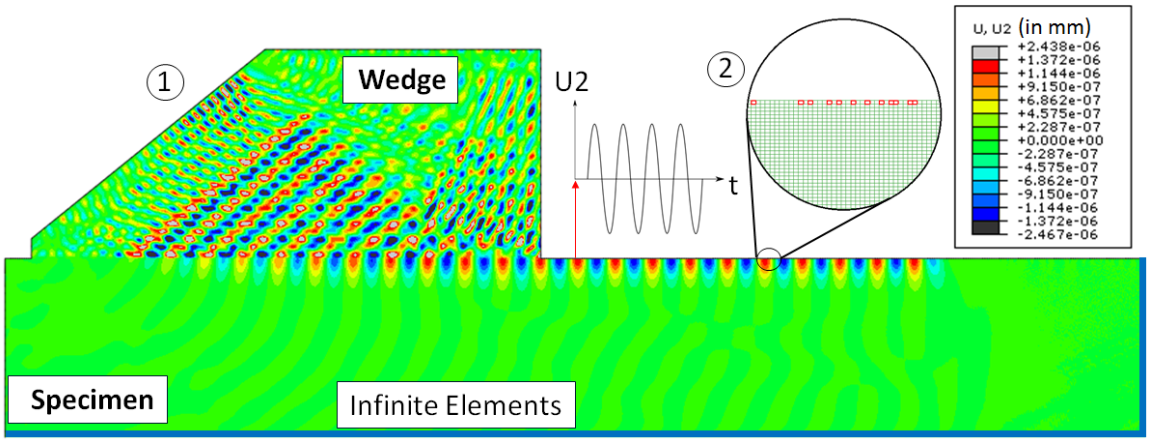

Figure 5.3: Schematic showing the wedge-specimen assembly including longitudinal waves in the wedge as well as Rayleigh waves propagating along the stress-free surface of the specimen. Infinite Elements and "crack elements" (2) are indicated.

least-squares optimization. A comparison of both stress-strain relationships shows good agreement and negligible error (Figure 4.14). To perform the optimization, we use the nominal stress and strain data of the effective stress-strain relationship as an artificial test data. The reason for this is that the optimization algorithm in ABAQUS is implemented originally to fit Mooney-Rivlin parameters to experimental data. In our case, we can utilize the power of the underlying optimization algorithm for our interests.

5.1.5 Mesh

When dealing with the FE-modeling of waves propagating in a solid, often the rule of thumb of 20 nodes per smallest wavelength of interest is mentioned [29]. Since this research investigates microcracks which are very small compared to the wavelength of the Rayleigh wave at 2 MHz frequency, the key length scale to consider is the size of the "crack elements." Beginning at the surface, we increase the element size in several steps towards the bottom of the specimen since only in the near-surface region a high resolution is necessary. Hence, we can decrease the computational effort significantly. The standard mesh size in the near-surface region is chosen to be 28.8 μm.

Wedge and specimen are modeled using CPE3 and CPE4R elements, with the latter being reduced integration plane strain elements with hourglass control. The FE-model solves for around 1.17 million degrees of freedom.

5.1.5.1 Absorbing Boundary – Infinite Elements

One problem which can effect simulation results are wave reflections at model boundaries. In order to counteract these reflection effects infinite elements (ABAQUS element type CINPE4) are generated at the bottom and the right end of the specimen. Despite mimicking an infinite space, these elements do not fully prevent wave reflections from model boundaries. Thus, we extend the specimen length so that the reflected waves do not disturb the node displacements in the test zone for microcracks. The depth of the specimen is also important for proper Rayleigh wave generation. If the depth is too small, Lamb waves instead of Rayleigh waves are generated. Since waves with higher frequencies, i.e. with smaller wavelengths, decay faster in amplitude with increasing depth, the wavelength of the fundamental wave is critical when choosing the depth of the specimen. The depth of the specimen is chosen to be 9 mm (or in multiples of the fundamental and second harmonic Rayleigh wavelength $6.4\lambda_{R_{fund}}$ and $12.8\lambda_{R_{sec}}$).

5.1.5.2 Generation of Random Distributions

The random distributions of "crack elements" are realized by renumbering elements in the test zone on the surface of the specimen (Figure 5.1) and randomly permuting these numbers in MATLAB. After that, the first 100, 200, 300, ... randomly permuted element numbers are taken, put into the ABAQUS input file and assigned the nonlinear material behavior. Note that we assign a linear elastic material behavior to the remaining elements in the test zone. The crack densities are similar to experimental observations by Zeitvogel et al. [48] who focused in one part of his research on analyzing micrographs of SCC-microcracked specimens.

5.1.6 Simulation

The simulations are performed on a Dell workstation with 8 cores, 3.6 GHz and 32 GB RAM. Using the capabilities of ABAQUS concerning parallel computing which allows for the parallel use of all 8 cores to perform the simulations, the simulation time is, depending on the crack density, around 20-30 minutes.

5.1.6.1 Time Increment and Simulation Time

Besides having a satisfying resolution in space, also an appropriate resolution in time has to be chosen. According to Moser et al. [29], the time increment should be chosen to be $\Delta t = 1/(20 f_{max})$ in which f_{max} is the highest frequency of interest. For the second harmonic frequency of 4 MHz the required timestep becomes Δt = 1s/(20 x 4E6) = 12.5 ns. In order to have appropriate resolution for the Discrete Fourier Transform (DFT) in the signal processing of node displacements, a time increment of 1 ns is chosen.

Simulations with smaller time increments show the same results. Thus, we conclude that the model converges.

In order to excite a specific amount of cycles, we divide the analysis into two steps. In the first step, the periodic displacement boundary conditions at the flank of the wedge are active. We choose a step time of t_1 = 1.1 x 10^{-5}s. Since we use a frequency f = 2MHz, this results in the excitation of (1.1 x 10^{-5}s $\cdot$ 2MHz =) 22 cycles. In the second step, these periodic displacement boundary conditions are inactive. Henceforth, no longitudinal waves are excited anymore. The step time of the second analysis step is t_2 = 3 x 10^{-5}s. The resulting total simulation time of $t_{sim} = t_1 + t_2$ = 4.1 x 10^{-5}s prevents the reflected waves from the right model boundary disturbing the node displacements in the test zone for "crack elements."

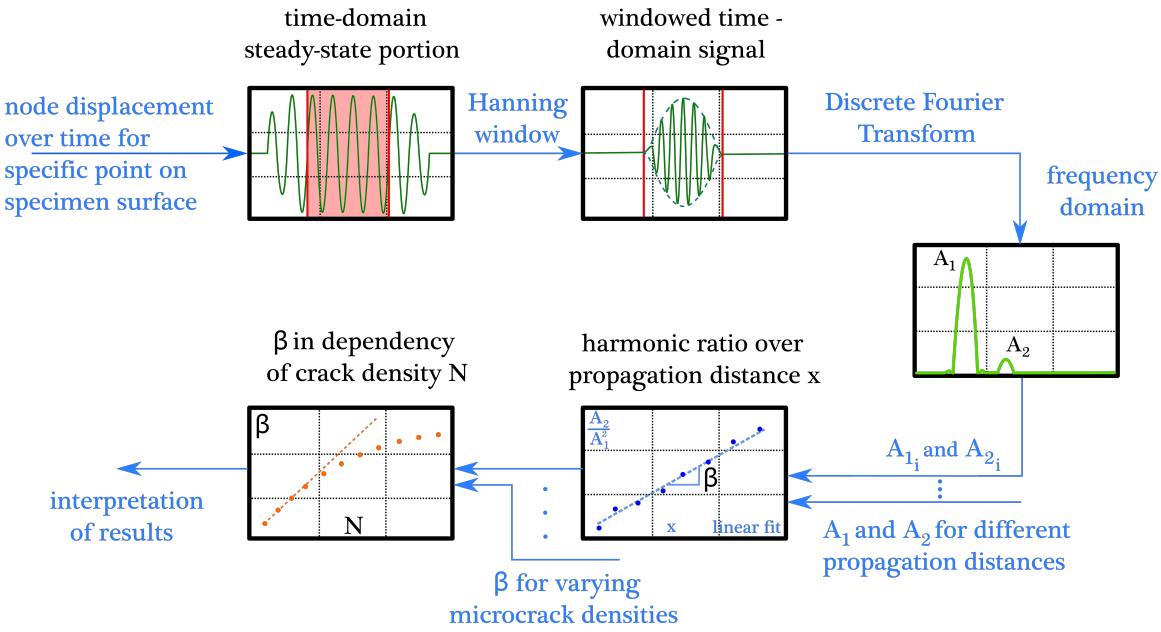

Figure 5.4: Signal processing of time-domain node displacement signals to calculate the acoustic nonlinearity parameter β and study it for varying crack densities.

5.1.7 Signal Processing

Figure 5.4 shows the signal processing procedure to analyze the time-domain node displacement signals in order to finally calculate the acoustic nonlinearity parameter, β. First, the vertical node displacements (U2) of 12 equally spaced nodes on the stress-free surface (the distance between these nodes is 5mm) of the specimen are loaded from an ABAQUS report file. Second, a steady-state portion of each node displacement signal is chosen. Third, we apply a Hanning window in order to reduce the influence of side lobes in the frequency spectrum. Note that the node displacements for these 12 nodes are stored for each time increment (each nanosecond). In contrast, displacement information for the whole model is only stored for 20 evenly spaced time intervals in each step to decrease the required disk space. Figure 5.5 shows a typical vertical node displacement at receiver position 9 for the linear model, i.e. for zero crack density.

As a next step, a DFT is performed on the extracted steady-state portion. Similar to [28], the amplitudes in the frequency domain are calculated back from the empirical formula

$$\text{time-domain amplitude} = \frac{4 \text{ x frequency domain amplitude}}{\text{number of data points used for Hanning window}}. \quad (85)$$

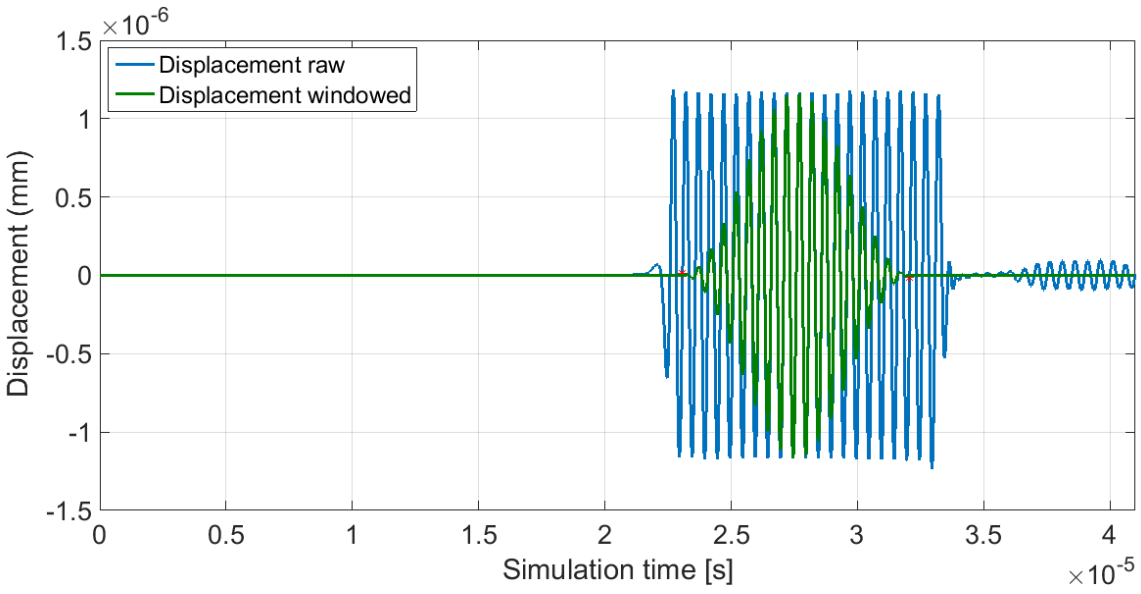

Figure 5.5: Vertical node displacement signal (U2) at receiver position 9 (blue), and Hanning windowed steady-state portion of the displacement signal (green) for zero crack density (undamaged material).

Figure 5.6 shows the frequency spectrum of the vertical displacement signal at receiver position 9. As can be clearly seen, in an undamaged medium, the Rayleigh wave stays monochromatic. A typical vertical node displacement signal at receiver position 9 for a high crack density of 27.27 cracks/millimeter is shown in Figure 5.7.

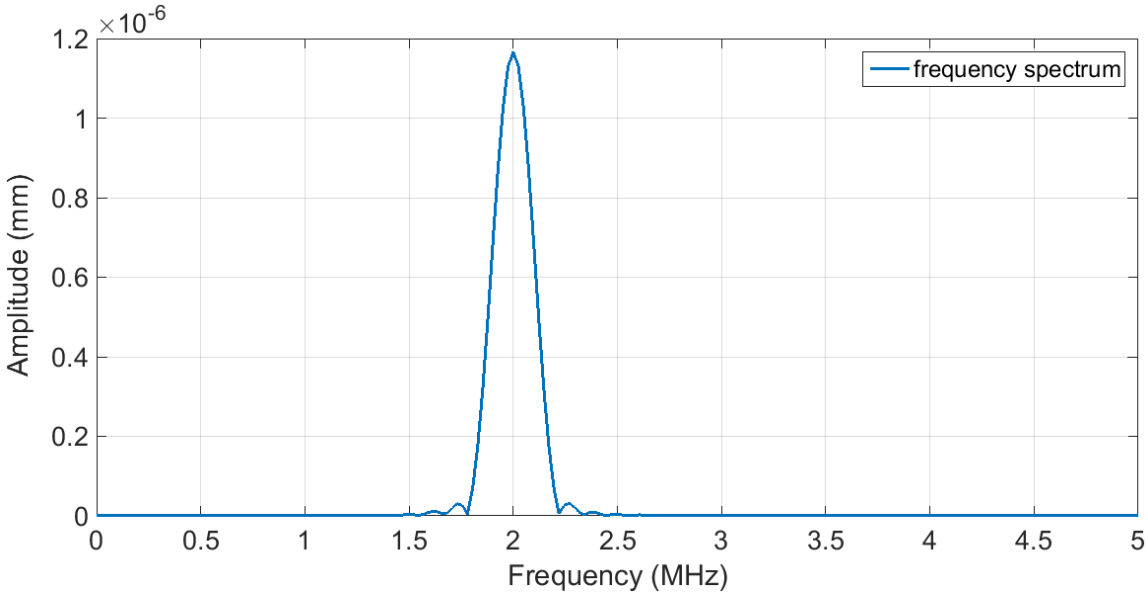

Figure 5.6: Frequency spectrum of vertical node displacement signal at receiver position 9 for zero crack density (undamaged material).

The frequency spectrum of this node displacement (receiver position 9) clearly reveals a peak at the second harmonic frequency (Figure 5.8). Note that the wave amplitude decreases very little since the scattering effect of the microcracks is very small.

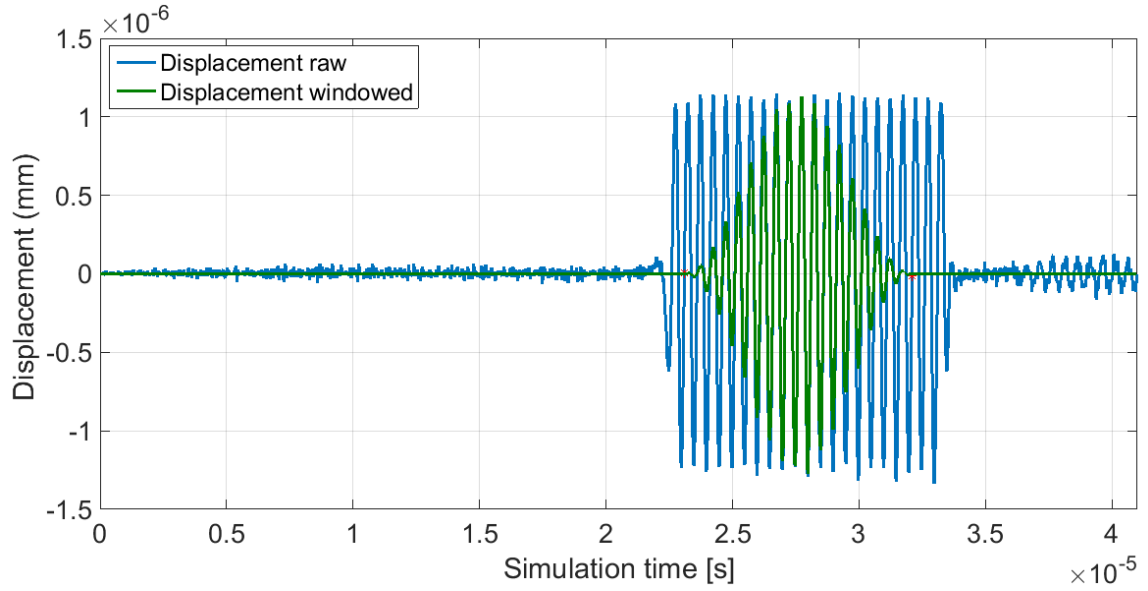

Figure 5.7: Vertical node displacement signal (U2) at receiver position 9 for specimen with high crack density (27.27 cracks/millimeter) and 95% fully-closed crack parts and 5% asperity contact crack parts.

In order to eliminate high-frequency noise, we design and apply a fourth-order Butterworth lowpass filter on the node displacement signals.

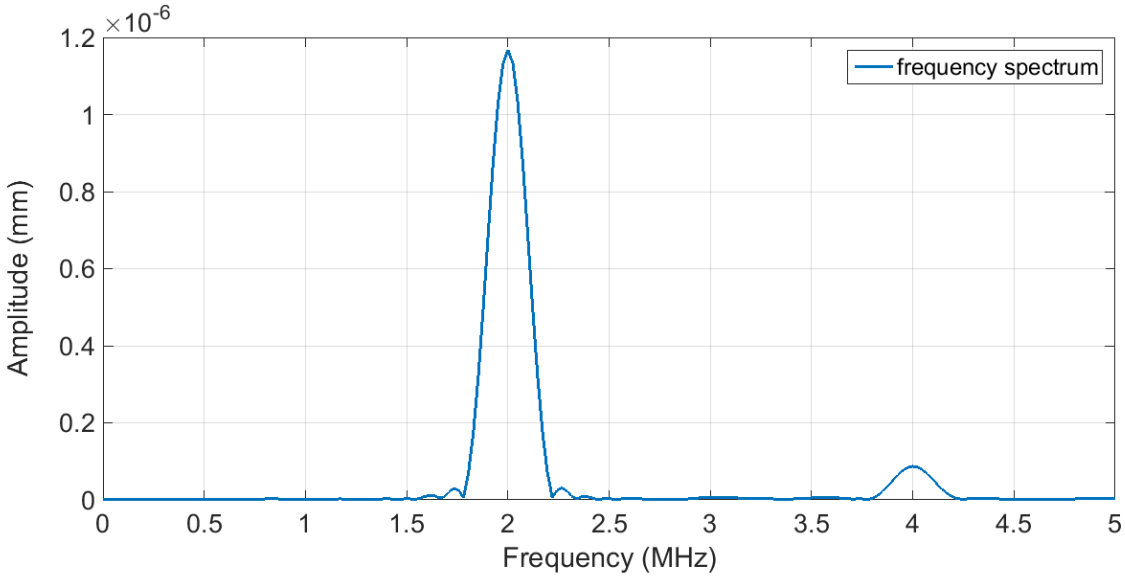

Figure 5.8: Frequency spectrum of vertical node displacement signal at receiver position 9 for a specimen with a high crack density (27.27 cracks/millimeter) and 95% fully-closed and 5% asperity contact crack parts, clearly showing the peak at the second harmonic frequency of 4 MHz.

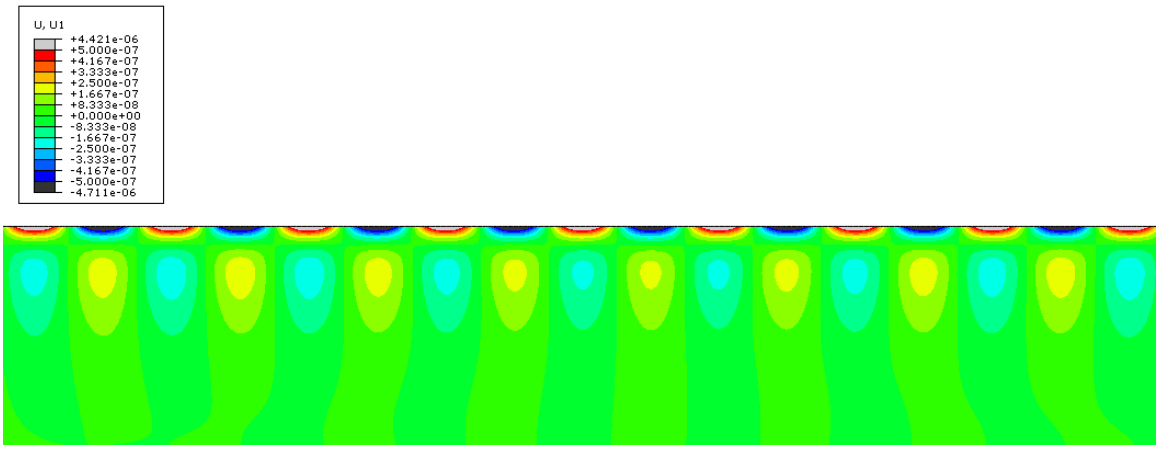

Figure 5.9: Horizontal Rayleigh wave displacement field (U1) in the specimen (displacement values in mm).

Figure 5.9 and 5.10 show the horizontal (U1) and vertical (U2) displacement fields of the Rayleigh waves obtained in the FE-simulation and qualitatively confirm proper Rayleigh wave generation in the specimen.

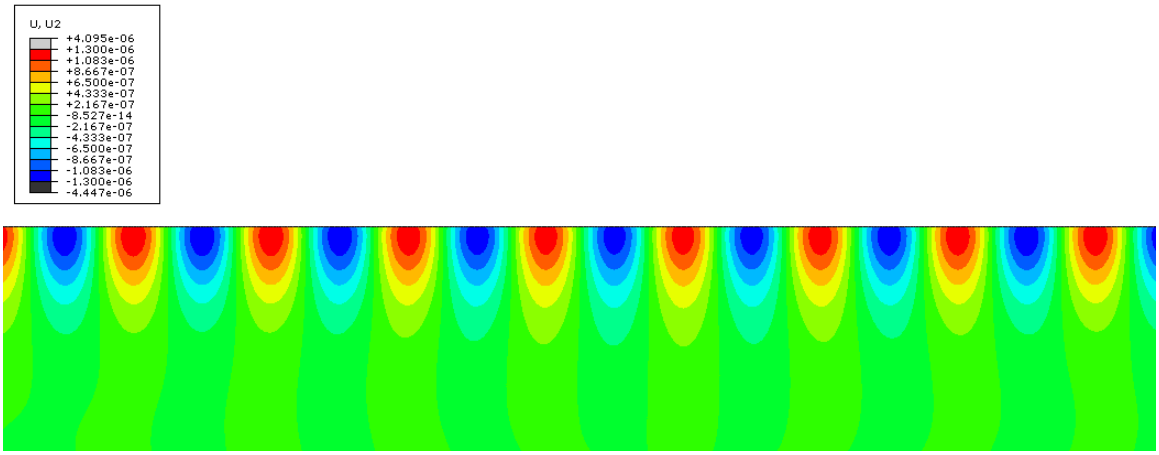

Figure 5.10: Vertical Rayleigh wave displacement field (U2) in the specimen (displacement values in mm).

Having obtained the frequency spectrum of the node displacement of a specific receiver position, the amplitudes of the first and second harmonic waves are stored, the second harmonic amplitude A_2 is normalized by the squared first harmonic amplitude A_1^2 and plotted over the propagation distance.

The same procedure is done for all of the 12 receiver positions. Furthermore, a linear fit for the harmonic ratio $\frac{A_2}{A_1^2}$ over propagation distance is performed. The slope of this linear fit is stored and multiplied by a constant term to obtain the absolute acoustic nonlinearity parameter β. We perform the same simulation for a range of microcrack densities from 0 cracks/millimeter (linear case) up to 27.27 cracks/millimeter in steps of 1.818 cracks/millimeter. The crack densities are chosen to be in the range of experimental observations by Zeitvogel et al. [48]. A MATLAB code has been developed to automatically perform the signal processing procedure for all receiver positions.

Our model for microcracks, and therefore the acoustic nonlinearity parameter β, depends on several model parameters which are summarized in Figure 5.11 and shown in which part of the modeling process they are required. First, the rough surface contact model to derive the nonlinear stress-strain relationship for asperity contact crack parts requires the RMS crack face roughness as well as an asperity number density and the choice of the degrees of freedom ξ for the χ^2-probability density function. Note that all of these parameters can be measured or estimated from experimental observations.

Moreover, macroscopic material properties such as Young's modulus, Poisson's ratio and density are required because β should of course depend on the investigated material. Since the effective stress-strain relationship is a result of a weighted average of local stress-strain relationships accounting for different crack opening states, the chosen weighting factors are another input to the model. Once the effective stress-strain relationship is obtained, the task is to optimize the parameters for a Mooney-Rivlin hyperelasticity model so that the resulting constitutive relationship fits the desired material behavior. Having said this, the parameters for the hyperelasticity model are not really additional input parameters, since they only try to fit what already has been defined by previous input parameters such as the parameters describing the stochastic nature of the rough surfaces. Finally, the crack density is an additional parameter. To summarize, our model for microcracks depends only on parameters which can be experimentally obtained or estimated by evaluation of micrographs of microcracked components.

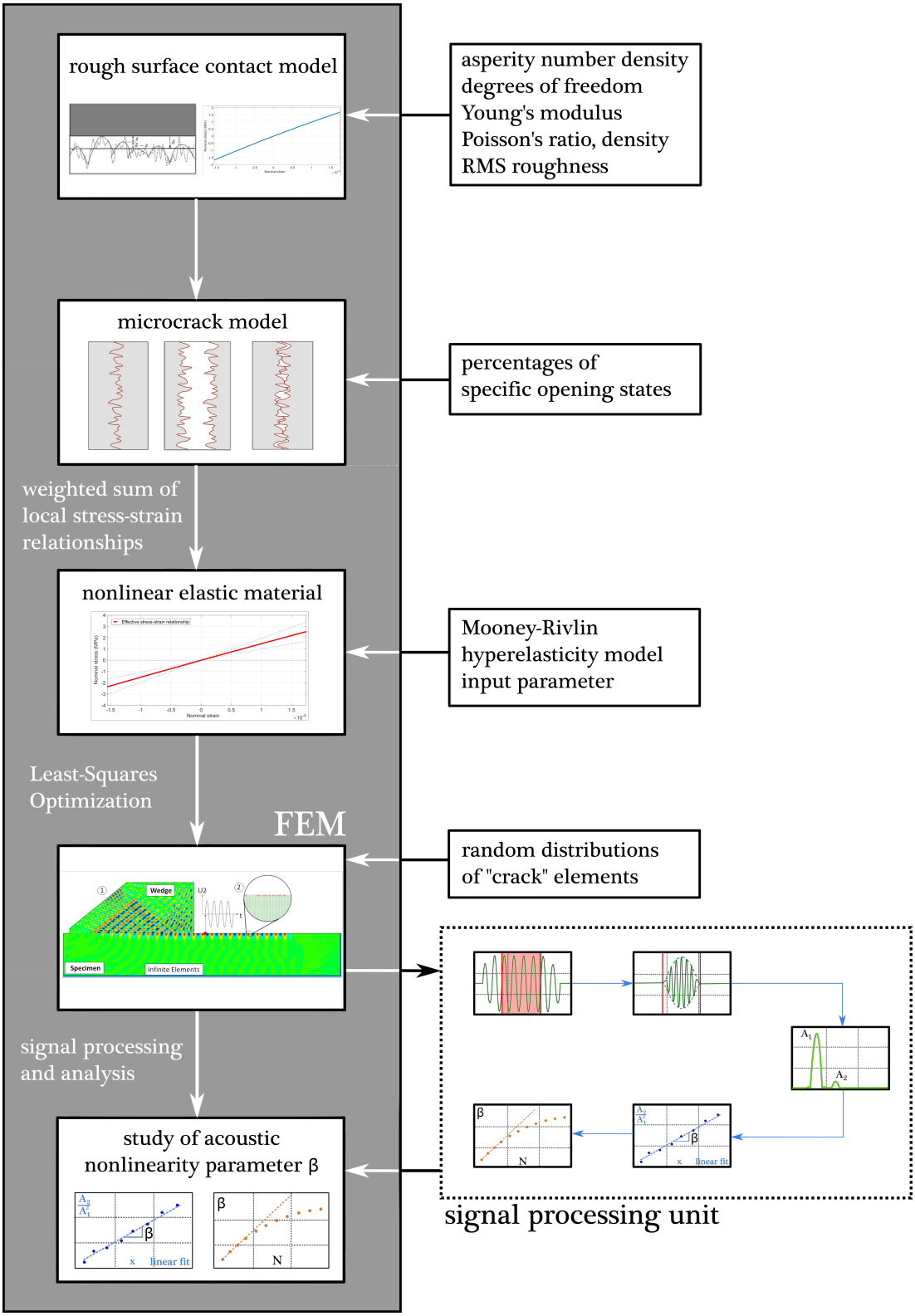

Figure 5.11: Overview of the modeling process and the required model parameters on which the acoustic nonlinearity parameter β depends.

5.2 Finite Element Modeling – Frictional Interface

Besides the normal stress Rayleigh waves impose on microcracks, Rayleigh waves also impose shear stress on the interface which can cause the crack faces to slide against each other. This section gives remarks [22] on the numerical description of this phenomenon and the FE-model which has been developed to study the dependency of odd higher harmonic generation in Rayleigh waves on shear stress driven randomly distributed frictional interfaces.

5.2.1 Numerical Background

Under Rayleigh wave incidence, the two crack faces of a microcrack impose both normal and shear stresses on each other. Note that these stresses only act on the crack faces when they are in contact. Unlike the real crack faces, finite element based surfaces do not impose any stresses on other finite element based surfaces as long as the user does not define that they can come into contact with each other. That means, if no contact surfaces are defined, finite elements penetrate each other.

Once these contact surfaces are defined, FE-codes such as ABAQUS are capable of determining if the surfaces are in contact or not. Sophisticated search algorithms keep track of the motion of the surfaces which could be able to come into contact. ABAQUS proceeds for one time increment under the assumption that contact between the two surfaces does not occur. After this time increment the FE-code checks if contact occured during the time increment. If no contact occurred, ABAQUS proceeds to the next time step. If contact occurred, ABAQUS performs acceleration corrections on the nodes involved. In the case of a pure master-slave approach (which means that one surface is treated as the master surface and one surface is treated as the slave surface), these acceleration corrections are applied on the kinematics of the slave nodes to comply with the constraint. ABAQUS calculates the resisting force that would have been required to prevent penetration. In a pure master-slave contact surface approach,

the master surface is allowed to penetrate the slave surface. Since we want to solely focus on the nonlinearity from the friction mechanism, we prefer a balanced master-slave approach which minimizes the penetration of contacting surfaces. Whereas in a pure master-slave approach one distinct master and one distinct slave surface is defined, a balanced master-slave approach calculates the accelerations corrections twice, one time with one surface as master and one surface as slave surface and vice versa. The final acceleration correction is obtained by the averaging of the two corrections [22]. After applying the acceleration corrections we obtain a corrected configuration in which contact constraints are enforced.

Once the surfaces are in contact, ABAQUS requires a definition of the interaction properties in both normal and transverse directions.

5.2.2 Normal Contact Constraint

We choose the zero penetration condition "hard contact," i.e. the contacting surfaces cannot penetrate each other. In addition, we use a balanced master-slave approach with a weighting factor of 0.5 and the surface-to-surface contact option. Furthermore, we choose the small-sliding formulation since the relative motion between two element faces describing the frictional interface of a microcrack is significantly smaller than the length of the involved element faces.

As a mechanical constraint formulation, the kinematic contact method is chosen. Finally, the "no separation after contact" option prevents wave rectification.

5.2.3 Surface Interaction Model – Coulomb Friction

After establishing the contact between two surfaces, the tangential interaction of the involved surfaces has to be defined. In this research we make use of the Coulomb friction model. Until the shear stress overcomes a critical shear stress limit, the tangential motion is zero. As the previous chapter discussed in more detail, this critical shear stress limit depends on the normal contact stress. When the shear

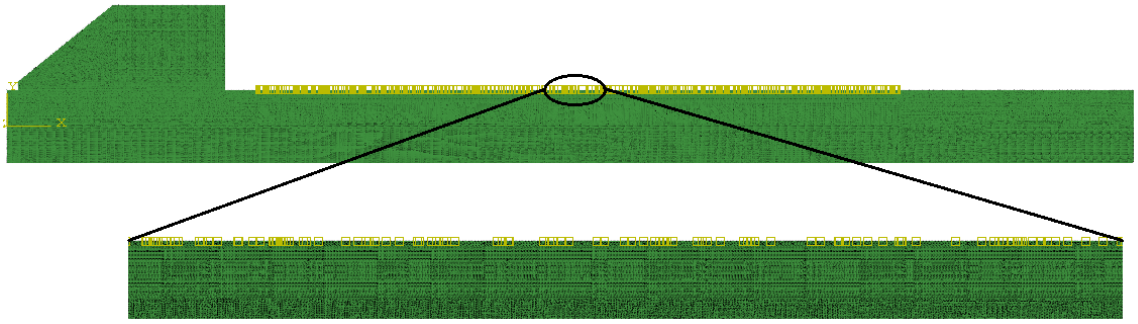

Figure 5.12: FE-model showing an exemplary random distribution of 300 frictional interfaces.

stress overcomes the shear stress limit, a Coulomb friction force acts against the relative tangential motion of the two surfaces as long as contact is established.

In order to study the effect of frictional interfaces on odd harmonic generation in Rayleigh waves, the same FE-model as proposed in the previous section is used, with the difference that both the wedge and the specimen are linear elastic and the nonlinearity is solely due to the frictional interfaces. A sample model has been built for the case of 300 randomly distributed frictional interfaces (Figure 5.12). To create the frictional interfaces, the connections between elements at the surface of the specimen have been removed manually. This was only possible by already removing the connections in the geometry description. In the next step, 600 contact surfaces have been defined.

Finally, the same interaction properties were assigned to all frictional interfaces in the input file. The same simulation time and element size as in the FE-model in the previous section is used.

The following chapter presents the simulation results of both FE-models. The dependency of the acoustic nonlinearity parameter β on crack density and surface roughness is studied. Moreover, odd harmonic generation in Rayleigh waves is shown.

CHAPTER VI

SIMULATION RESULTS AND DISCUSSION

This chapter summarizes the simulation results of the FE-models which are introduced in the previous chapter. The dependency of the acoustic nonlinearity parameter β for Rayleigh waves on crack density is shown. Moreover, the dependency of β on both varying crack opening states and RMS roughnesses of the crack faces is determined. As described in the previous chapter, the node displacement at the 12 receiver positions are stored for each time step. A Hanning window is imposed on the steady-state portion of the node displacement signal. Then a DFT is performed on the Hanning windowed signal and the amplitudes in the frequency domain are calculated. Having obtained the first and second harmonic amplitudes A_1 and A_2, the harmonic ratio $\frac{A_2}{A_1^2}$ is plotted over the propagation distance, x.

6.1 Dependency of the Harmonic Ratio on Crack Density

Figure 6.1 shows the harmonic ratio $\frac{A_2}{A_1^2}$ as a function of propagation distance for three distinct crack densities of 9.1, 18.2, and 27.3 microcracks/millimeter. The harmonic ratio increases linearly with propagation distance for all three crack densities. Moreover, the slope – the acoustic nonlinearity parameter β – of the linear fit increases with crack density. This confirms that NLU methods can be applied to monitor microcrack damage in components, and to quantitatively relate the harmonic ratio to the severeness of existing damage. When evaluating Figure 6.1, the question is raised how the slope of the linear fit lines depend on crack density. A numerical study is performed for a range of crack densities from 0 cracks/millimeter (linear case) up to 27.27 cracks/millimeter in steps of 1.818 cracks/millimeter. The dependency of β on crack density is studied for different opening state percentages of the cracks.

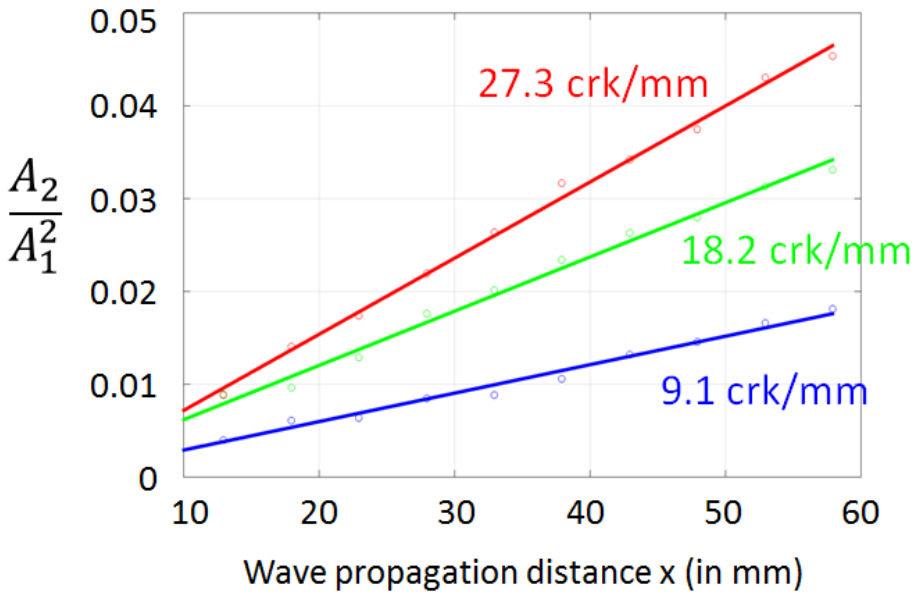

Figure 6.1: Harmonic ratio over propagation distance for the three distinct crack densities 9.1, 18.2, and 27.3 cracks/millimeter.

6.2 Dependency of β on Opening State and Crack Density

Figure 6.2 shows the dependency of the acoustic nonlinearity parameter β on both crack density and different compositions of crack opening states. It becomes clear that β increases with increasing microcrack damage. For small crack densities ("dilute concentration"), this increase is linearly related to the increase in crack density, indicating that there are no interactions between adjacent cracks. For higher crack densities, the microcracks are assumed to start to interact, and the acoustic nonlinearity is no longer additive. This is similar to the behavior seen by Cantrell [10] as described in Chapter 4 for the case of longitudinal waves. This qualitatively validates the properness of the current numerical study. Note that there is no specific threshold crack density, but instead a transition zone from small to higher crack densities in which the acoustic nonlinearity, β, starts to saturate. However, a typical crack density threshold is marked in Figure 6.2 (8 cracks/millimeter). For the case of 95% fully-closed crack parts and 5% asperity contact crack parts, the acoustic nonlinearity

is higher than the one obtained from simulations with the same crack densities but lower percentages of asperity contact crack parts. This is consistent with what is expected.

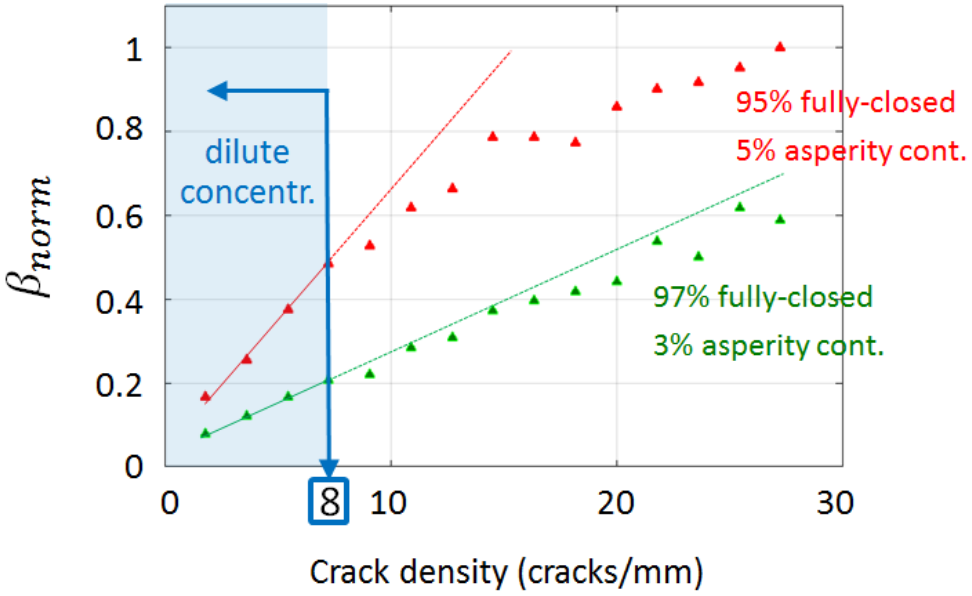

Figure 6.2: Normalized acoustic nonlinearity parameter β in dependency of crack density and percentages of crack opening states.

6.3 Effect of Crack Face Roughness

In order to study the dependency of β on crack face roughness, the nonlinear stress-strain relationship accounting for asperity contact crack parts is derived for three different RMS roughness values of the composite surface (see Chapter 4 for details). Three simulations for exactly the same choice of crack opening state percentages and crack density are performed, and the acoustic nonlinearity parameter β determined. Figure 6.3 shows that β increases with increasing roughness of the crack faces. This makes sense since the rougher the crack faces, the more flexible and more nonlinear the interfaces are.

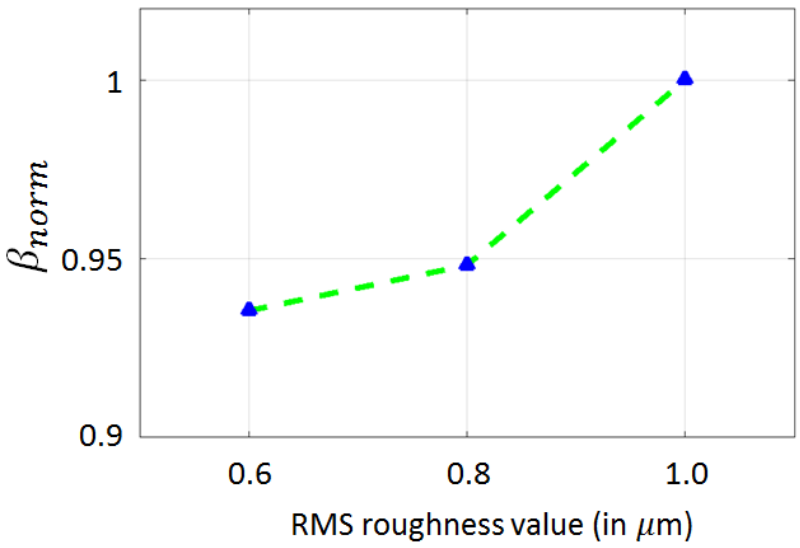

Figure 6.3: Acoustic nonlinearity parameter β for three different RMS roughnesses of the composite surface as input to the derivation of the nonlinear stress-strain relationship accounting for asperity contact crack parts.

6.4 Odd Harmonic Generation by Frictional Interfaces

After chapter 4 investigated the stick-slip motion of a single frictional interface under a Rayleigh wave drive, this section presents preliminary simulation results obtained by the second FE-model to study odd harmonic generation in Rayleigh waves due to randomly distributed frictional interfaces.

Figure 6.4 shows a sample frequency spectrum of the vertical node displacement for the case of 300 frictional interfaces, a friction coefficient of $\mu = 0.15$, an excitation amplitude of 5 nm, and with constraining of the opening of the contacts.

Since we want to solely focus on the effect of the frictional interfaces and not the effect of the opening and closing of the contact, a way has to be found to prevent opening of the contact. This is achieved by the generation of coincident nodes at each interface. We locate the nodes on both contact surfaces at the same position. Following this modification, the contact is closed initially. Using the option "no separation after contact" prevents the opening of the contact. Therefore, the contact faces cannot separate, but instead slide against each other under a Coulomb friction model.

The frequency spectrum only shows peaks at the odd higher harmonic frequencies (6 and 10 MHz), which fits with the observations of Solodov et al. [40] and Blanloeuil et al. [6] who investigated frictional interfaces under a shear wave drive.

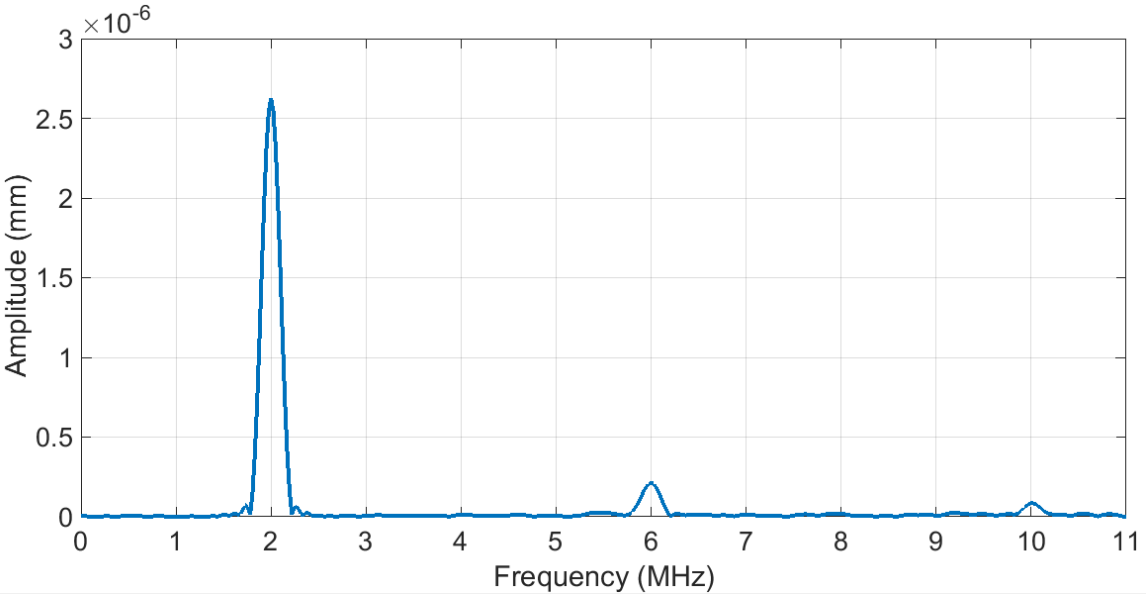

Figure 6.4: Sample frequency spectrum of vertical node displacement (U2) revealing odd harmonic generation in Rayleigh surface waves due to randomly distributed frictional interfaces.

CHAPTER VII

CONCLUSION AND FUTURE WORK

7.1 Conclusion

This work presents a micromechanical model for the nonlinearity of randomly distributed surface microcracks which are compressed under an internal stress in the solid. The behavior of a microcrack in the normal direction has been modeled by an effective stress-strain relationship which results from a weighted average of local stress-strain relationships which account for different opening states of a microcrack along its crack path. Whereas one local stress-strain relationship accounts for fully-closed crack parts which have been modeled by a linear stress-strain relationship, another local stress-strain relationship accounts for fully-opened crack parts which cause zero stress transmission across the crack faces. In the remaining crack parts asperity contact takes place. These crack parts have been modeled by a nonlinear stress-strain relationship. The derivation of this nonlinear stress-strain relationship builds upon the classical rough surface contact model of Greenwood and Williamson [18] in the framework Nazarov and Sutin [30] proposed. In order to study the effect of random distributions of microcracks on the generation of higher harmonics in Rayleigh surface waves, a FE-model has been developed. Using a least-squares optimization, the input parameters of a Mooney-Rivlin hyperelasticity model have been optimized to fit the desired material behavior. In the FE-model, "crack elements" behave in accordance to the effective stress-strain relationship. The dependency of the acoustic nonlinearity in Rayleigh surface waves has been studied for varying microcrack densities. The simulation results make qualitative sense and agree with the previous work by Cantrell for the case of longitudinal waves [10]. Moreover, the acoustic nonlinearity increased

with crack surface roughness. Second harmonic generation (SHG) has been found to be a reliable technique to monitor damage due to distributed surface-breaking microcracks. For small crack densities, the acoustic nonlinearity increases almost linearly with crack density. However, for higher crack densities the acoustic nonlinearity is not additive anymore.

In addition to the contact problem of rough crack faces under a combination of internal stress in the solid and Rayleigh wave normal stress, the transverse motion of crack faces due to the Rayleigh wave shear stress has been investigated. Whereas the normal stress alternates the compressive stress at the interface and causes a sinusoidal static friction force threshold, the Rayleigh wave shear stress drives the frictional interface. As long as the static friction force threshold is overcome, the interface slips. Due to a symmetric stiffness variation twice over one input strain period, only odd harmonics are generated due to the nonlinear friction mechanism. Odd harmonic generation has also been observed in the simulation results of a second FE-model which uses a master-slave contact surface approach with constraining of the opening to prevent wave rectification.

7.2 Future Work

In order to further develop the modeling of randomly distributed surface microcracks, the combined effect of normal and transverse motion of rough crack faces has to be investigated and implemented into a FE-model. To realize this combination, the numerical constraint "no separation after contact" has to be replaced by a more physical realization which enables us to adjust the contact normal pressure at the interface.

To adjust the model parameters for the underlying micromechanical model, experimental characterization of crack face roughness as well as static and dynamic microcrack friction coefficients is required.

REFERENCES

[1] Achenbach, J. D., *Wave Propagation in Elastic Solids.* Elsevier Science Publishers B.V., 1973.

[2] ASTM, *Standard Terminology Relating to Fatigue and Fracture Testing.* http://compass.astm.org/EDIT/html_annot.cgi?E1823+13, accessed in August 2015.

[3] ASM Aerospace Specification Metals Inc., *AISI Type 304 Stainless Steel.* http://asm.matweb.com/search/SpecificMaterial.asp?bassnum=MQ304A, accessed in August 2015.

[4] Astro, *Sound waves travel in the Earth's interior as P-waves and S-waves.* http://www.astro.uwo.ca/~jlandstr/planets/webfigs/earth/slide1.html, accessed in August 2015.

[5] Barnard, D. J., *Variation of nonlinearity parameter at low fundamental amplitudes.* Applied Physics Letters, vol. 74, no. 17, p. 2447, 1999.

[6] Blanloeuil, P., Croxford, A., Meziane, A., *Numerical and experimental study of the nonlinear interaction between a shear wave and a frictional interface.* Journal of the Acoustical Society of America 135 (4), 2014.

[7] Bower, A. F., *The Influence of Crack Face Friction and Trapped Fluid on Surface Initiated Rolling Contact Fatigue Cracks.* Journal of Tribology, vol. 110/707, 1988.

[8] Brown, S.R., Sholtz, C.H., *Closure of random elastic surfaces in contact.* Journal of Geophysical Research 90, 5531 - 5545, 1985.

[9] Buck, O., Morris, W. L., Richardson, J. M., *Acoustic harmonic generation at unbonded interfaces and fatigue cracks.* Applied Physics Letters 33, 371, 1978.

[10] Cantrell, J. H., *Fundamentals and applications of nonlinear ultrasonic nondestructive evaluation.* Ultrasonic Nondestructive Evaluation (Kundu, T., ed.), CRC Press, 2004.

[11] Cantrell, J. H., *Nondestructive Evaluation of Metal Fatigue Using Nonlinear Acoustics.* Review of Progress in Quantitative Nondestructive Evaluation, Vol. 28, edited by D. O. Thompson and D. E. Chimenti (AIP, Melville, 2009), pp. 19-32, 2009.

[12] Corrosion-Doctors.org, *Stress Corrosion Cracking.* http://corrosion-doctors.org/Forms-SCC/scc.htm, accessed in August 2015.

[13] Cottis, R. A., *Stress Corrosion Cracking, Guides to Good Practice in Corrosion Control.* Corrosion and Protection Centre, UMIST under contract from NPL for the Department of Trade and Industry, brochure.

[14] De Garmo, E. P., Black, J. T., Kohser, R. A., *DeGarmo's Materials And Processes In Manufacturing.* Eleventh Edition, John Wiley & Sons, 2011.

[15] Delrue, S., van den Abeele, K., *Nonlinear spectroscopy of closed delaminations and surface breaking cracks: Finite element simulations of clapping and nonlinear air-coupled emission.* AIP Conference Proceedings 1474, 191, 2012.

[16] Drinkwater, B., Dwyer-Joyce, R., Cawley, P., *A study of the interaction between ultrasound and a partially contacting solid-rubber solid interface.* Proceedings of the Royal Society London A 452, 2613 - 2628, 1996.

[17] Graff, K. F., *Wave Motion in Elastic Solids (Dover Books on Engineering).* Dover Publications, 1991.

[18] Greenwood, J. A., Williamson, J. B. P., *Contact of Nominally Flat Surfaces.* Proceedings of the Royal Society of London. Series A, Mathematical and Physical Sciences, 1966.

[19] Hamilton, M. F., Blackstock, D. T., *Nonlinear Acoustics.* San Diego, CA: Academic Press, 1998.

[20] Herrmann, J., *Generation and detection of higher harmonics in Rayleigh waves using laser ultrasound.* Master's thesis, Georgia Institute of Technology, 2005.

[21] Herrmann, J., Kim, J.-Y., Jacobs, L. J., Qu, J., Littles, J. W., Savage, M. F., *Assessment of material damage in a nickel-base superalloy using nonlinear Rayleigh surface waves.* Journal of Applied Physics, vol. 99, no. 12, p. 124913, 2006.

[22] Hibbitt, Karlsson, Sorensen, *Getting Started with ABAQUS/Explicit.* Hibbitt, Karlsson & Sorensen, Inc., 1998.

[23] Kawashima, K., Omote, R., Ito, T., Fujita, H., Shima, T., *Nonlinear acoustic response through minute surface cracks: FEM simulation and experimentation.* Elsevier Science B.V., Ultrasonics 40, 611615, 2002.

[24] Kim, J.-Y., Baltazar, A., Rokhlin, S. I., *Ultrasonic assessment of rough surface contact between solids from elastoplastic loading-unloading hysteresis cycle.* Journal of the Mechanics and Physics of Solids 52, 1911 1934, 2004.

[25] Kim, J.-Y., Lee, J. S., *A micromechanical model for nonlinear acoustic properties of interfaces between solids.* Journal of Applied Physics 101, 043501, 2007.

[26] Marino, Daniel, *Using nonlinear ultrasound measurements to assess the stage of thermal damage in modified 9% ferritic martensitic steel.* Master's thesis, Georgia Institute of Technology, 2014.

[27] Morlock, F., *Evaluation of stress corrosion cracking in sensitized 304 stainless steel using nonlinear Rayleigh waves.* Master's thesis, Georgia Institute of Technology, 2014.

[28] Morlock, M. B., *Nonlinear mixing of two collinear Rayleigh waves.* Master's thesis, Georgia Institute of Technology, 2013.

[29] Moser, F., Jacobs, L. J., Qu, J., *Modeling elastic wave propagation in waveguides with the finite element method.* NDT & E International 32, 225 - 234, 1999.

[30] Nazarov, V. E., Sutin, A. M., *Nonlinear elastic constants of solids with cracks.* Journal of the Acoustical Society of America 102, 3349, 1997.

[31] NDT, *Fatigue Properties.* https://www.nde-ed.org/EducationResources/ CommunityCollege/Materials/Mechanical/Fatigue.htm, accessed in August 2015.

[32] Okada, J., Ito, T., Kawashima, K., Nishimura, N., *Finite Element Simulation of Nonlinear Acoustic Behavior at Minute Cracks Using Singular Element.* Japanese Journal of Applied Physics 40, 3579, 2001.

[33] Pecorari, C., *Nonlinear interaction of plane ultrasonic waves with an interface between rough surfaces in contact.* Journal of the Acoustical Society of America 113 (6), 2003.

[34] Pecorari, C., Solodov, I., *Nonclassical Nonlinear Dynamics of Solid Surfaces in Partial Contact for NDE Applications.* Universality of Nonclassical Nonlinearity, Applications to Non-Destructive Evaluations and Ultrasonics, ed. by Pier Paolo Delsanto, Springer, 2006.

[35] Pellegrino, J., *Corrosion Fatigue in Longwall Mining.* http://www.rjlg.com/wp-content/uploads/2014/05/51-1000x-sei.jpg, accessed in August 2015.

[36] Richardson, J. M., *Harmonic generation at an unbonded interface I. Planar interface between semi-infinite elastic media.* International Journal of Engineering Science 17, 73 - 85, 1979.

[37] Roos, Eberhard, *Fatigue Damage.* Lecture Notes "Material Science I+II" Lecture, IMWF University of Stuttgart, 2009/2010.

[38] Rose, J. L., *Ultrasonic Waves in Solid Media.* Cambridge University Press, 1999.

[39] Sneddon, I., *Fourier Series.* Routledge & Kegan, New York, 1951.

[40] Solodov, I., Döring, D., Busse, G., *New Opportunities for NDT Using Non-Linear Interaction of Elastic Waves with Defects.* Journal of Mechanical Engineering 57, 3, 169 - 182, 2011.

[41] Thiele, S., *Air-coupled detection of Rayleigh surface waves to assess material nonlinearity due to precipitation in alloy steel.* Master's thesis, Georgia Institute of Technology, 2013.

[42] Timoshenko, S., Goodier J. N., *Theory of elasticity.* New York: McGraw-Hill, 1951.

[43] Viktorov, I. A., *Rayleigh and Lamb Waves: Physical Theory and Applications.* Plenum Press, 1967.

[44] Walker, S. V., *Characterization of fatigue damage in A36 steel specimens using nonlinear Rayleigh surface waves.* Master's thesis, Georgia Institute of Technology, 2011.

[45] Walker, S. V., *Fatigue damage evaluation in A36 steel using nonlinear Rayleigh surface waves.* NDT & E International, vol. 48, pp. 10 - 15, 2012.

[46] Wikipedia.com, *Intergranular Corrosion, Unsensitized and Heavily Sensitized Microstructure*. https://en.wikipedia.org/wiki/Intergranular_corrosion, accessed in August 2015.

[47] Wikipedia.com, *Huygens-Fresnel-principle*. https://en.wikipedia.org/wiki/Huygens-Fresnel_principle, accessed in August 2015.

[48] Zeitvogel, D., *Characterization of damage due to stress corrosion cracking in carbon steel using nonlinear surface acoustic waves*. Master's thesis, Georgia Institute of Technology, 2012.

[49] Zeitvogel, D., Matlack, K. H., Kim, J. Y., Jacobs, L. J., Singh, P. M., Qu, J., *Characterization of stress corrosion cracking in carbon steel using nonlinear Rayleigh surface waves*. NDT & E International 62, 144 - 152, 2014.